

Study on Preparation and Characterization of Lead-Free Piezoelectric Films

Liqiang Liu

March 2022

**Department of Intelligent Systems Design Engineering
Toyama Prefectural University**

PREFACE

Energy-converting materials have been developed and progressed with the advancement of informational society. Piezoelectric materials, which possess the capabilities of mechanical-electrical energy conversion, have been applied in various fields, such as optics, photonics, metrology, precision mechanics, mechanical engineering, and microelectronics. In practical applications, lead-containing piezoelectric materials are widely used because of their beneficial properties. The research of lead-free materials has stagnated due to the avoidance of lead contamination. However, lead-free materials cannot be completely alternative to lead-containing materials in performance. Therefore, the improvement of lead-free materials is still a crucial topic.

This thesis focuses on the preparation and the properties improvement of lead-free material films. Chapter I of this thesis introduces the background and current situation of lead-free film, thus arriving at the subject and significance of this thesis. Chapter II describes the preparation and evaluation methods of oxide films and emphasizes the reason for the selection of the Pechini process. Chapter III systematically describes the modified Pechini process, which is suitable for multicomponent systems of BaZrO_3 - $(\text{K}_{0.45}\text{Na}_{0.5}\text{Li}_{0.05})\text{NbO}_3$ - $(\text{Bi}_{0.5}\text{Na}_{0.5})\text{TiO}_3$ / $(\text{La}_{0.5}\text{Na}_{0.5})\text{TiO}_3$. A detailed fabrication process is explored and the contemporary elements of lead-free material research are described to fit the Pechini process. Chapter IV considers the effect of prepress on the lead-free $(\text{Bi}_{0.5}\text{Na}_{0.5})\text{TiO}_3$ - BaTiO_3 materials. The application temperature of $(\text{Bi}_{0.5}\text{Na}_{0.5})\text{TiO}_3$ -based materials is improved by the compressive prepress from the difference of coefficients of thermal expansion between the $(\text{Bi}_{0.5}\text{Na}_{0.5})\text{TiO}_3$ -based thick film and the

substrates. Chapter V is the conclusion of this thesis. All work will be summarized, and the contribution is emphasized.

ACKNOWLEDGMENTS

The author would like to express the deepest gratitude to his advisor, Professor Tomoaki Karaki, for his constant encouragement, instructive advice, and selfless help in the author's master's and Ph.D. studies. Thanks to his patience, enthusiasm, and erudition, the author could complete this thesis well.

The author also would like to thank Professor Tadashi Fujii for his kindness and help. On the other hand, the author is deeply indebted to all other tutors and teachers at Toyama Prefectural University for their profound knowledge and important advice to my paper. Their assistance and stimulating discussion about this research and their strong support in the last three years has impressed the author.

The author really appreciates Mr. S. Hayano and Mr. X. Pan of Lead Techno Co. in Shiga, Japan, who offered timely and kindly help with the measurement job of this experiments.

The author acknowledges Dr. Yuichi Sakai of Toyama Industrial Technology Research and Development Center, who helped measure the testing data of TG/DTA and comprehensively guided and supported the experiment in Chapter III. He gave me valuable suggestions and helped the author tirelessly when faced with difficulties during the process of writing these sections.

The author would like to thank Tao Zhang, Nan Wei, and other members of the Intelligent Robotics Laboratory.

The author would like to thank his beloved family for their loving consideration and great confidence in him through his career of Ph.D. studies.

LIST OF ABBREVIATIONS

| | | |
|------------------|---|--|
| CMOS | Complementary Metal Oxide Semiconductor | |
| CVD | Chemical vapor deposition | |
| DC | Direct current | |
| EDXA | Energy dispersive X-ray analysis | |
| FRAM | Random-access memory | |
| MEM | Microelectromechanical system | |
| MPB | Morphotropic phase boundary | |
| PDF | Powder diffraction file | |
| PFM | Piezoresponse force microscopy | |
| PVD | Physical vapor deposition | |
| RF | Radio frequency | |
| RoHS | <i>Directive on the restriction of the use of certain hazardous substances in electrical and electronic equipment</i> | |
| RT | Room temperature | |
| RTA | Rapid thermal annealing | |
| SAW | Surface acoustic wave | |
| SBC | Solution-based chemistry | |
| SEM | Scanning electron microscopy | |
| TG/DTA | Thermogravimetric & differential thermal analysis | |
| TMA | Thermomechanical analysis | |
| XRD | X-ray diffraction | |
| XRD ² | Two-dimensional X-ray diffraction | |
| d | Piezoelectric charge coefficient | |
| ϵ_r | Dielectric constant | |
| k_p | Electromechanical coupling constant | |
| S | Mechanical strain | |
| $\tan\delta$ | Dielectric loss | |
| E_c | Coercive electric field | |
| P_r | Remanent polarization | |
| P_s | Spontaneous polarization | |
| T_C | Curie temperature | |
| T_d | Depolarization temperature | |
| T_m | Temperature of the max value | |
| BT | Barium titanate | BaTiO ₃ |
| BNT | Sodium bismuth titanate | (Bi _{0.5} Na _{0.5})TiO ₃ |
| BNT-BT | (Bi _{0.5} Na _{0.5})TiO ₃ -BaTiO ₃ | |
| BNT- x BT | (1- x)(Bi _{0.5} Na _{0.5})TiO ₃ - x BaTiO ₃ | |

| | | |
|-------------|--|---|
| BZ-KNLN-BNT | $\text{BaZrO}_3\text{-(K}_{0.45}\text{Na}_{0.5}\text{Li}_{0.05}\text{)NbO}_3\text{-(Bi}_{0.5}\text{Na}_{0.5}\text{)TiO}_3$ | |
| BZ-KNLN-LNT | $\text{BaZrO}_3\text{-(K}_{0.45}\text{Na}_{0.5}\text{Li}_{0.05}\text{)NbO}_3\text{-(La}_{0.5}\text{Na}_{0.5}\text{)TiO}_3$ | |
| CA | Citric acid | $\text{C}_6\text{H}_8\text{O}_7$ |
| EG | Ethylene glycol | |
| KNN | Potassium sodium niobate | $\text{K}_{0.5}\text{Na}_{0.5}\text{NbO}_3$ |
| LNO | Lanthanum niobate | LaNiO_3 |
| PZT | Lead zirconate titanate | $\text{PbZr}_{1-x}\text{Ti}_x\text{O}_3$ |
| SBT | Strontium bismuth tantalate | $\text{SrBi}_2\text{Ta}_2\text{O}_9$ |
| STO | Strontium titanate | SrTiO_3 |

CONTENTS

PREFACEi

ACKNOWLEDGMENTS iii

LIST OF ABBREVIATIONSiv

CHAPTER I

INTRODUCTION

| | |
|--|--------|
| 1.1 Piezoelectricity..... | - 1 - |
| 1.1.1 Piezoelectric coefficient..... | - 2 - |
| 1.1.3 Curie temperature..... | - 3 - |
| 1.1.4 Dielectric loss..... | - 3 - |
| 1.1.5 Spontaneous polarization..... | - 3 - |
| 1.1.6 Ferroelectric hysteresis loop..... | - 4 - |
| 1.1.7 Piezoelectric domains..... | - 5 - |
| 1.2 Piezoelectric Materials and Film Application..... | - 5 - |
| 1.2.1 FRAM..... | - 7 - |
| 1.2.2 MEMS..... | - 7 - |
| 1.2.3 Microwave electronics..... | - 7 - |
| 1.3 Piezoelectric oxides..... | - 8 - |
| 1.4 Lead-containing and Lead-free Piezoelectric Materials..... | - 9 - |
| 1.4.1 Lead-containing piezoelectric materials..... | - 9 - |
| 1.4.2 Lead-free piezoelectric materials..... | - 11 - |
| 1.5 Films and Deposition Techniques..... | - 15 - |
| 1.6 Thesis Objectives and Organization..... | - 19 - |
| 1.6.1 Thesis objectives..... | - 19 - |
| 1.6.2 Thesis organization..... | - 21 - |
| References..... | - 22 - |

CHAPTER II

PREPARATION AND CHARACTERIZATION OF FILMS

| | |
|---|--------|
| 2.1 Introduction..... | - 26 - |
| 2.2 Preparation and Characterization of Thin Films..... | - 27 - |
| 2.2.1 Preparation of substrates..... | - 27 - |
| 2.2.2 Preparation of bottom/top electrodes..... | - 27 - |
| 2.2.3 Synthesis of the precursor solution..... | - 28 - |
| 2.2.4 Spin-coating deposition..... | - 29 - |
| 2.2.5 TG/DTA..... | - 30 - |
| 2.2.6 X-ray diffraction analysis..... | - 30 - |
| 2.2.7 Scanning electron microscopy..... | - 31 - |

| | |
|---|--------|
| 2.3 Preparation and Characterization of Thick Films | - 32 - |
| References..... | - 36 - |

**CHAPTER III
MULTICOMPONENT LEAD-FREE THIN FILMS**

| | |
|--|--------|
| 3.1 Introduction..... | - 37 - |
| 3.2 Experiment..... | - 38 - |
| 3.2.1 Selection of raw materials..... | - 38 - |
| 3.2.2 Exploration of the precursor solution synthesis..... | - 42 - |
| 3.2.3 Exploration of the bottom electrode | - 48 - |
| 3.2.4 Exploration of the spin-coating condition..... | - 50 - |
| 3.2.5 Thermal treatment process | - 51 - |
| 3.3 Results and Discussion | - 52 - |
| 3.3.1 BZ-KNLN-BNT..... | - 52 - |
| 3.3.2 BZ-KNLN-LNT | - 57 - |
| 3.4 Summary | - 64 - |
| References..... | - 66 - |

**CHAPTER IV
LEAD-FREE PIEZOELECTRIC THICK FILMS AFFECTED BY
PRESTRESS FROM SUBSTRATES**

| | |
|----------------------------------|--------|
| 4.1 Introduction..... | - 68 - |
| 4.2 Experiment..... | - 70 - |
| 4.3 Results and Discussion | - 71 - |
| 4.4 Summary | - 85 - |
| References..... | - 86 - |

CHAPTER V CONCLUSION AND PROSPECT..... - 88 -

LIST OF PUBLICATIONS..... - 91 -

LIST OF PRESENTATIONS..... - 92 -

CHAPTER I

INTRODUCTION

1.1 Piezoelectricity

Piezoelectricity is a property of certain crystalline materials with non-center-symmetries.¹⁾ Direct piezoelectricity was first discovered by Pierre and Jacques Curie in 1880 while studying the effect of pressure on the generation of electrical charges in natural crystals such as quartz, tourmaline, Rochelle salt, etc.²⁾ They found that when an external force was applied to the dielectric material in a certain direction, the material itself generated an internal polarization with the deformation which led to the orderly arrangement of dipoles. Sequentially, the electric potential difference generated due to the same amount of opposite charge appeared on the corresponding material surface. After releasing the external force, the ordered orientation was no longer maintained, and the potential difference disappeared. Subsequently, the converse piezoelectric effect was predicted by Lippmann³⁾ based on thermodynamic considerations and confirmed experimentally by Curie brothers⁴⁾ in 1881. The converse piezoelectric effect can be described as a phenomenon where dielectric materials under an electric field generate stress and strain, which disappear with the withdrawal of the electric field.^{5,6)}

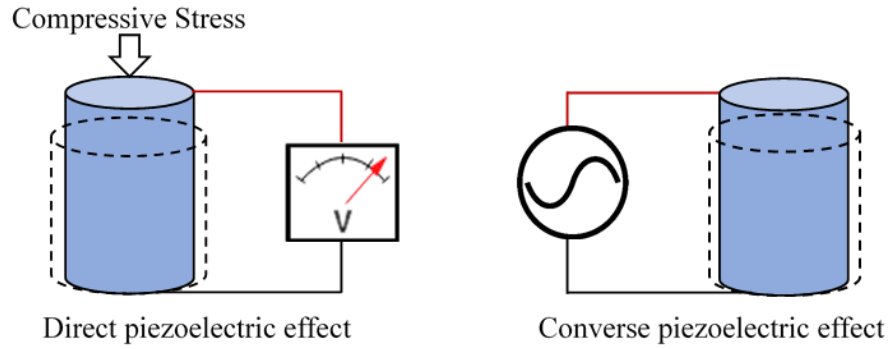


Fig. 1.1 Direct and converse piezoelectric effects.

1.1.1 Piezoelectric coefficient

Due to the anisotropy of piezoelectric materials, physical constants relate to both the direction of the applied mechanical or electric force and the directions perpendicular to the applied force. Consequently, each constant generally has two subscripts that indicate the directions of the two related quantities.

The piezoelectric charge constant (d) is the polarization per unit of mechanical stress (T) applied to the piezoelectric material, or the mechanical strain (S) per unit of the electrical field applied to the piezoelectric material. The first subscript of d represents the direction of polarization that occurs within the material when the electric field E is zero, as well as the direction of the applied electric field. The second subscript represents the direction of applied stress and induced strain, respectively. d_{33} induces polarization in direction 3 (parallel to the direction in which ceramic element is polarized) per unit stress applied in direction 3 or induced strain in direction 3 per unit electric field applied in direction 3. d_{33} can be obtained as following:⁷⁾

$$d_{33} = k_{33} \sqrt{s_{33}^E \epsilon_{33}^T} \quad (1-1)$$

where k_{33} is the electromechanical coupling coefficient for longitudinal vibration in direction 3, s_{33}^E is accompanying strain in direction 3, and ϵ_{33}^T is the dielectric constant in direction 3.

1.1.3 Curie temperature

Curie temperature (T_C) is the temperature at which a ferroelectric material transition to paraelectric. Hence, T_C is the temperature where ferroelectric materials lose their spontaneous polarization as a first or second order phase change occurs.⁸⁾ However, due to the complicated phase transition occurring in the relaxor system materials, definite Curie temperature is difficult to determine. Consequently, T_m , the temperature of the max value of relative permittivity, is generally applied.

1.1.4 Dielectric loss

Under the alternating electric field, dielectric loss is generated due to the delayed dipole transformation, and the forced dipole moment rotation turns into heat energy consumption. The dielectric loss factor is defined as the tangent of the loss angle ($\tan\delta$).⁹⁾ Usually, the consumption of electrical energy in a dielectric is expressed as the resistance (R):

$$\tan\delta = \frac{1}{\omega CR} \quad (1-2)$$

where C is the dielectric electrostatic capacity and ω is the angular frequency of the alternating electric field. Usually, a low dielectric loss represents good performance.

1.1.5 Spontaneous polarization

In a crystal cell, the centers of positive and negative charges do not coincide, resulting in an inherent electric dipole moment. The periodic repetition of the structure causes the electric dipole moments to be arranged to form a high polarization. This

polarization originates with an internal structure instead of external electric fields and thus is called spontaneous polarization.¹⁰⁾

1.1.6 Ferroelectric hysteresis loop

The ferroelectric hysteresis loop is a characterization of piezoelectric materials measured by their polarization (P) as a function of the applied AC electric field (E).^{11,12)} The dielectric behavior of piezoelectrics is distinctly nonlinear. Due to the motion of domain walls, the variation of polarization under the electric field is hysteretic.^{13,14)}

As shown in Fig. 1.2, at a low electric field, there is a linear relationship between P and E because the electric field is insufficient to switch any domain and the piezoelectrics behave as normal dielectrics. As the external field increases, the domain changes to the direction more inclined to the electric field and the polarization increases rapidly until all the domains change and the polarization becomes saturated, which is related to the spontaneous polarization P_s . As the strength of the electric field is reduced to zero, some regions will remain in the positive direction and the crystal will show remanent polarization (P_r). Remanent polarization can only be eliminated when the applied field along the negative direction reaches a certain value, which is called the coercive electric field (E_c). An ideal hysteresis loop is symmetric and the positive and negative values of E_c and P_r are equal.¹⁵⁾

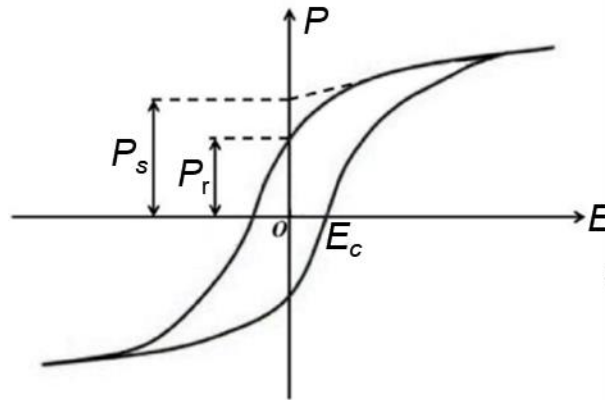


Fig. 1.2 A typical polarization hysteresis loop in ferroelectrics.

1.1.7 Piezoelectric domains

A spontaneous polarization of piezoelectrics occurs below the Curie temperature. Piezoelectric domains are uniformly polarized regions with sizes ranging from a few nanometers to tens of micrometers.¹⁶⁾ The boundary between two domains with a thickness of a few lattice cells is called the domain wall.¹⁷⁾ The domain wall is thin enough to reduce the elastic energy generated by the strain near the walls.¹⁸⁾ The formations of the ferroelectric domain and domain walls depend on the number of conceivable orientations of the dipole moment by the spontaneous polarization.¹⁹⁾

1.2 Piezoelectric Materials and Film Application

Piezoelectric materials have been studied for over a century. Piezoelectric materials are widely used in devices that require the conversion of electrical and mechanical energy. Barium titanate (BaTiO_3 , BT) ceramics were first commercial products for phonograph pickups in 1947.²⁰⁾ Subsequently, lead zirconate titanate

($\text{PbZr}_{1-x}\text{Ti}_x\text{O}_3$, PZT) started to be applied because of their superior dielectric and piezoelectric properties. Table 1.1 shows a list of piezoelectric material application fields in photonics, mechanical engineering, microelectronics and life science.

Table 1.1 Application fields of piezoelectric materials.²¹⁾

| Classification | Applications |
|--|---|
| Optics, Photonics and Measuring Technology | Image stabilization; Scanning microscopy; Autofocus systems; Interferometry; Fiber optic alignment & switching; Fast mirror scanners; Adaptive and active optics; Laser tuning; Mirror positioning; Holography; Stimulation of vibrations |
| Precision Mechanics and Mechanical Engineering | Vibration cancellation; Structural deformation; Out-of-roundness grinding, drilling, turning; Tool adjustment; Wear correction; Needle valve actuation; Micropumps; Linear drives; Piezo hammers; Knife-edge control in extrusion tools; Micro engraving systems; Shock wave generation |
| Microelectronics | Nano-metrology; Wafer and mask positioning; Critical dimensions measurement; Microlithography; Inspection systems |
| Life Science, Medicine, Biology | Patch-clamp drives; Gene technology; Micromanipulation; Cell penetration; Micro dispensing devices; Audio physiological stimulation; Shock wave generation |

For piezoelectric films, inchoate research can be traced back to late 1960s and early 1970s.²²⁻²⁴⁾ The development of Si devices and thin-film technologies attracted interest in the use of piezoelectric films to make non-volatile memories. Then Complementary Metal Oxide Semiconductor (CMOS) and microelectromechanical systems (MEMSs) were invented in succession. Until now, ferroelectric random-access memories (FRAMs), MEMSs, and microwave electronics are still three main applications of piezoelectric films. Among them, due to the high performance and low cost, toxic lead contained piezoelectric films are still mainstream in the practical application.

1.2.1 FRAM

FRAM is a semiconductor device which utilizes the polarization inversion of ferroelectrics under external electric field. The positive and negative remanent polarization states stand for “0” and “1” in binary. FRAM is a type of non-volatile memory and is widely used in frequent data logging requirement situation, such as networking, infrastructure, manufacturing, medical records, etc. Although PZT based FRAMs is almost widely used in practical applications, lead-free materials have been studied successively due to the toxicity of lead. Among them, SrBi₂Ta₂O₉ (SBT) is representative lead-free FRAM with a low storage capacity.

1.2.2 MEMS

MEMS is a miniature machine with both electrical and mechanical components. MEMSs are composed of micrometer-level parts such as microsensors, microprocessors, microactuators, data-processing units, and parts that interact with exterior pieces. Since the 1990s, piezoelectric MEMSs such as ultrasonic micromotor, micropump, miniature electronic tubes, accelerometers, gyroscopes, acoustic sensors, cantilever sensing and driving elements of the atomic force microscope, and ultrasonic transducers for medical and sonar applications have been invented and produced.²⁶⁾

1.2.3 Microwave electronics

Piezoelectric thin film transducers are the key components of the surface acoustic wave (SAW) devices. The wave transmission frequency (f_0) is calculated as:

$$f_0 = V_s/2t \quad (1-4)$$

where V_s is speed of sound, and t is the thickness of thin film. By the control of the micron-level thickness, the piezoelectric thin film transducers can work at 2-12 GHz.²⁷⁾

1.3 Piezoelectric oxides

It is well known that the piezoelectric materials can be divided into perovskite, tungsten-bronze, bismuth layer, etc. Among of them, perovskite structure oxides are pivotal piezoelectric materials. The name of the “perovskite structure” is derived from the structure of Calcium titanate (CaTiO_3). The general chemical formula of perovskite structure is ABO_3 , where A and B are vastly different sized cations. This typical perovskite unit is called an oxy-octahedron. This oxy octahedron shows a centrosymmetric structure above T_C and does not display piezoelectricity. When the temperature is below T_C , B atom is shifted from its central position, resulting in a shift of the positive and negative charges. The spontaneous polarization (P_s) occurs and piezoelectricity appears. For perovskite structure, it exists more than 6 orientations of P_s . The randomly arranged perovskite structure with multiple P_s orientations in ceramics lead to its superior piezoelectricity to tungsten-bronze, bismuth layer, and other structures.

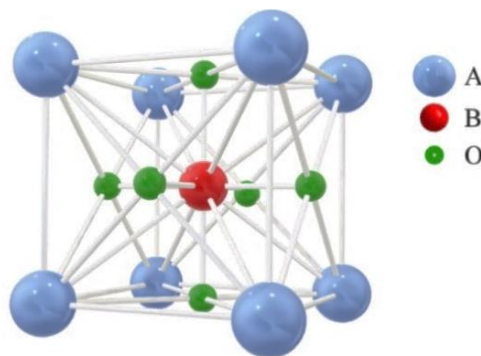


Fig. 1.3 Perovskite crystal structure.

Since barium titanate (BaTiO_3), the earliest ferroelectric with perovskite structure, was discovered, the exploration of new perovskite structural ferroelectrics has yet to cease. Substitutions of the A and B ions can generate a variety of perovskite ferroelectrics and the substitutions must keep sizes according to the Goldschmidt tolerance factor t , defined as follows:

$$t = \frac{r_A + r_O}{\sqrt{2}(r_B + r_O)} \quad (1-3)$$

where r_A , r_B , and r_O are the radii of the A, B cations and oxygen ion, respectively. The values of t are generally at a range of 0.88 to 1.09 for a stable perovskite structure.²⁰⁾ Possible substitutions of A and B ions were summarized by Roy.²¹⁾ For piezoelectrics, BaTiO_3 , $(\text{Bi,Na})\text{TiO}_3$, BiFeO_3 , and $\text{K}_{0.5}\text{Na}_{0.5}\text{NbO}_3$ are typical perovskite structure materials.

1.4 Lead-containing and Lead-free Piezoelectric Materials

1.4.1 Lead-containing piezoelectric materials

Perovskite structural piezoelectric materials, especially those consisting of lead based piezoelectric ceramics, have served as excellent and indispensable materials. For example, PZT, the earliest-studied lead-containing piezoelectric material, has been the most incisively explored and the most widely used for its desirable elastic, dielectric, piezoelectric, pyroelectric, ferroelectric, and optical properties.³⁰⁾ After the PZT, other lead-containing piezoelectric materials such as lead titanate, lead barium lithium niobite, and modified lead titanate were prepared and studied in succession.

Considering that environmental pollution is against the sustainable development of society, there is no question of the environment-friendly lead-free piezoelectric

ceramic development is one of the main development concerns of modern piezoelectric ceramics. However, in practical applications, the compositions of PZT-based materials are at their almost perpendicular morphotropic phase boundaries (MPB), as shown in Fig. 1.4 (a). To piezoelectric materials, MPB is referred to the phase transitions between the tetragonal and the rhombohedral phases based on the change of the composition. From the phase diagram of PZT, the composition with $x = 0.47$ shows the MPB, $x < 0.47$ shows the rhombohedral phase, and $x > 0.47$ shows tetragonal phase, respectively. With the temperature increasing, the tetragonal phase and the rhombohedral phase and transform to cubic phase, respectively. As shown in equation (1-1) in Chapter 1.1.1, the piezoelectric coefficient (d_{33}) is the multiplication of the dielectric constant (ϵ_r) and the electromechanical coupling constant (k_p). Due to the PZT with MPB composition displaying the largest ϵ_r and k_p , the piezoelectric coefficient of PZT is the highest at the MPB as shown in Fig. 1.4 (b). The MPB of PZT is almost vertical, indicating the temperature stability of piezoelectricity in a large temperature range. Thus, the PZT with the MPB composition is mainly applied in industry. In addition, compared with lead-free materials, PZT exhibits excellent piezoelectric properties, low cost of raw materials, and easy preparation. Consequently, PZT is widely used in practical application.

However, the commercial PZT-based materials contain above 60 wt% of lead oxide which is a serious hazard to the human brain and nervous system. Due to the toxicity of lead oxide in these materials to both humans and the environment, lead-containing materials are restricted to use according to the *Directive on the restriction of the use of certain hazardous substances in electrical and electronic equipment* (RoHS).³²⁾ Nevertheless, lead-containing materials are still used in practice, because the performance of lead-free materials is not yet capable of replacing lead-containing

materials completely. Consequently, the development of environmentally friendly lead-free piezoelectric materials that can replace the lead-containing materials is very important.

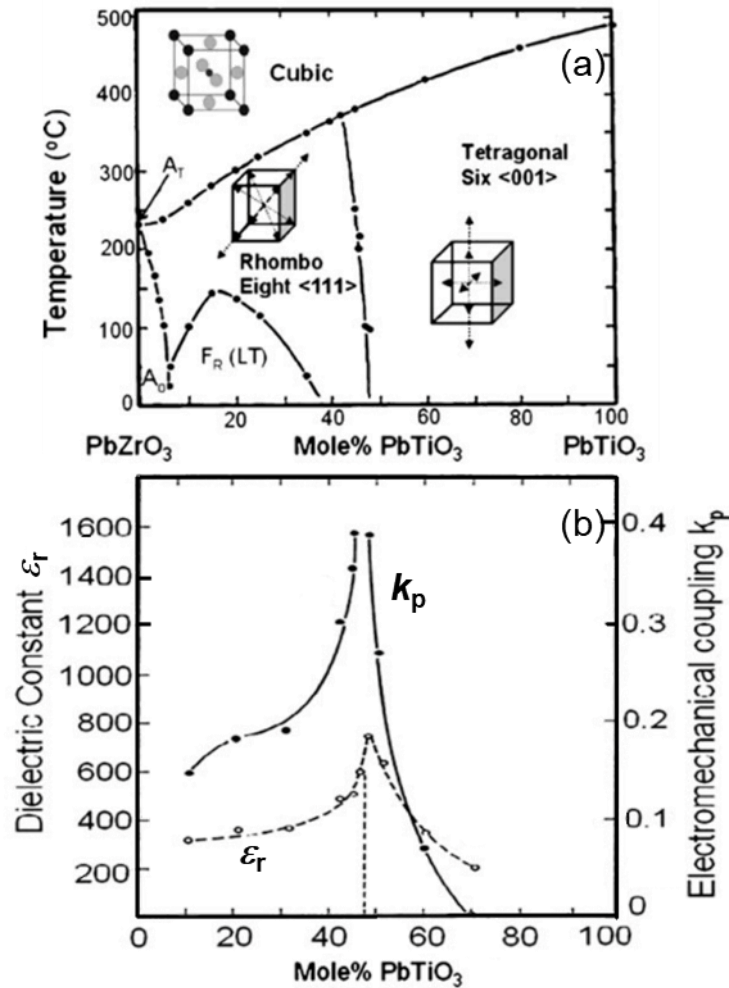


Fig. 1.4 (a) Phase diagram of Pb(Zr,Ti)O₃ and (b) dielectric constant and electromechanical coupling constant in the Pb(Zr,Ti)O₃ system.³¹⁾

1.4.2 Lead-free piezoelectric materials

According to the crystal structure, lead-free piezoelectric materials can be divided into perovskite, tungsten-bronze, bismuth layer. Due to the low properties, Tungsten-bronze and bismuth layer structure materials is rarely studied. According, studies are

focused on the perovskite structure piezoelectric materials, especially potassium sodium niobate [(K,Na)NbO₃, KNN]-based materials, sodium bismuth titanate [(Bi,Na)TiO₃, BNT]-based materials, and barium titanate (BaTiO₃, BT)-based materials. However, comparing with the PZT, lead-free piezoelectric ceramics with binary components show inclined MPBs in phase diagrams, as shown in Fig. 1.5 (a). Thus, lead-free piezoelectric ceramics do not show temperature stability of piezoelectricity, commonly.

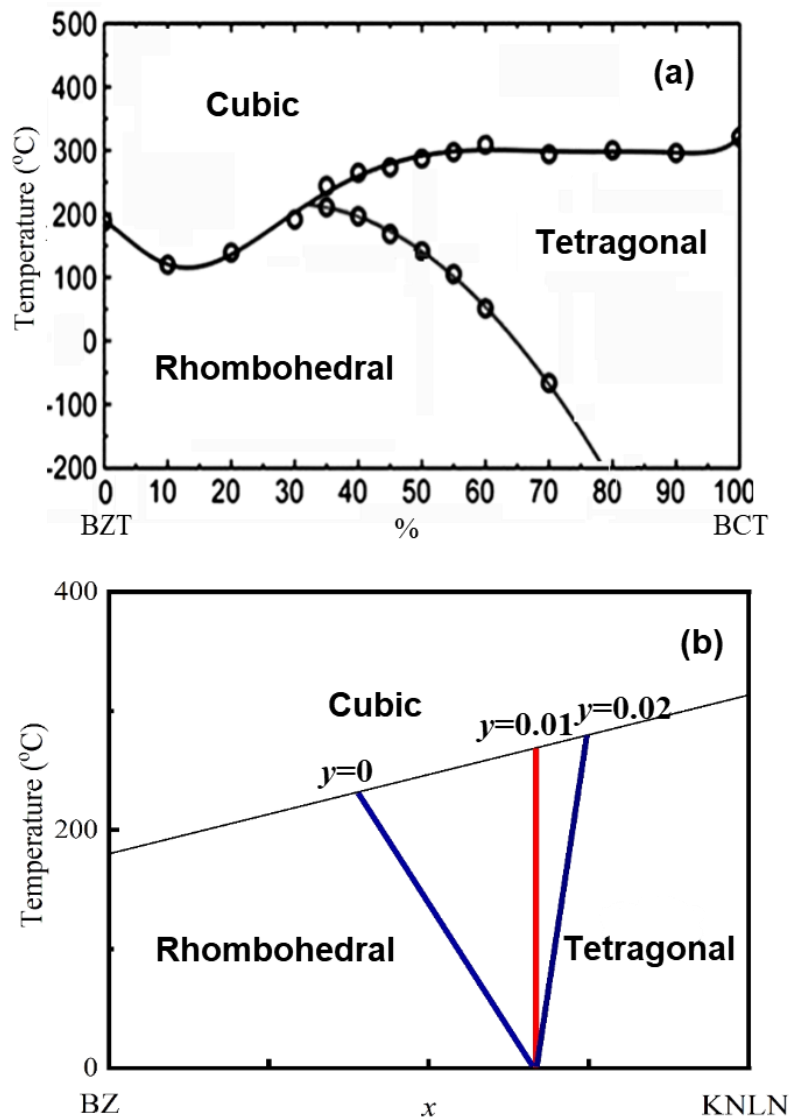


Fig. 1.5 Phase diagrams of (a) $(1-x)\text{Ba}(\text{Zr}_{0.2}\text{Ti}_{0.8})\text{O}_3-x(\text{Ba}_{0.7}\text{Ca}_{0.3})\text{TiO}_3$ (BZT-BCT)³³ and (b) $(1-x-y)\text{BaZrO}_3-x(\text{K}_{0.45}\text{Na}_{0.5}\text{Li}_{0.05})\text{NbO}_3-y(\text{Bi}_{0.5}\text{Na}_{0.5})\text{TiO}_3$ (BZ-KNLN-BNT)³⁴.

KNN refers to the solid solution of ferroelectric potassium niobate (KNbO_3) and anti-ferroelectric sodium niobate (NaNbO_3). In the phase diagram of the KNN solid solution (Fig. 1.6), KNbO_3 shows the phase transition of rhombohedral-orthorhombic-tetragonal-cubic with increasing temperature. NaNbO_3 shows the antiferroelectric phase at room temperature which undergoes a series of complex phase transitions with increasing temperature. Finally, NaNbO_3 becomes cubic above $630\text{ }^\circ\text{C}$. All KNN show an orthorhombic phase at room temperature. Among them, $\text{K}_{0.5}\text{Na}_{0.5}\text{NbO}_3$ shows the highest piezoelectric properties. The $\text{K}_{0.5}\text{Na}_{0.5}\text{NbO}_3$ phase transition process is similar to that of KNbO_3 , and the phase transition temperatures of $\text{K}_{0.5}\text{Na}_{0.5}\text{NbO}_3$ are about $-160\text{ }^\circ\text{C}$, $200\text{ }^\circ\text{C}$ and $400\text{ }^\circ\text{C}$. In previous studies, by the introduction of BaZrO_3 rhombohedral phase $\text{K}_{0.5}\text{Na}_{0.5}\text{NbO}_3\text{-BaZrO}_3$ solid solution could be obtained, as shown in Fig. 1.5 (b).³⁴⁾ The MPB in $\text{K}_{0.5}\text{Na}_{0.5}\text{NbO}_3\text{-BaZrO}_3$ is sloped and the phase transition around the MPB composition is rhombohedral-tetragonal-cubic with temperature increasing. The temperature instability of the properties disallows them from application in a wide range of temperatures. However, in previous studies the inclined MPB of $\text{K}_{0.5}\text{Na}_{0.5}\text{NbO}_3\text{-BaZrO}_3$ was found to be changed to vertical with the addition of a third component, e.g., $(\text{Bi}_{0.5}\text{Na}_{0.5})\text{TiO}_3$ and $(\text{La}_{0.5}\text{Na}_{0.5})\text{TiO}_3$.^{34,35)} In addition, K and Na elements are easily volatilized at high temperature. This makes it difficult to sinter high-density ceramics using the conventional process. By partial replacement of A site (K^+ , Na^+) using Li^+ , the melting point of $\text{K}_{0.5}\text{Na}_{0.5}\text{NbO}_3$ solid solution could be decreased and made easy to sinter. In addition, the introduction of Li could also increase the T_C .

As stated above, the compositions of modified MPB in the lead-free piezoelectric KNN-system materials are always complicated, and the thin film preparation of this kind of lead-free piezoelectric materials is difficult. In this study, $\text{BaZrO}_3\text{-}$

$(K_{0.45}Na_{0.5}Li_{0.05})NbO_3-(Bi_{0.5}Na_{0.5})TiO_3/(La_{0.5}Na_{0.5})TiO_3$ (BZ-KNLN-BNT/LNT) thin films are attempted to be prepared. The vertical MPB compositions of these KNN-based lead-free piezoelectric material are applied.

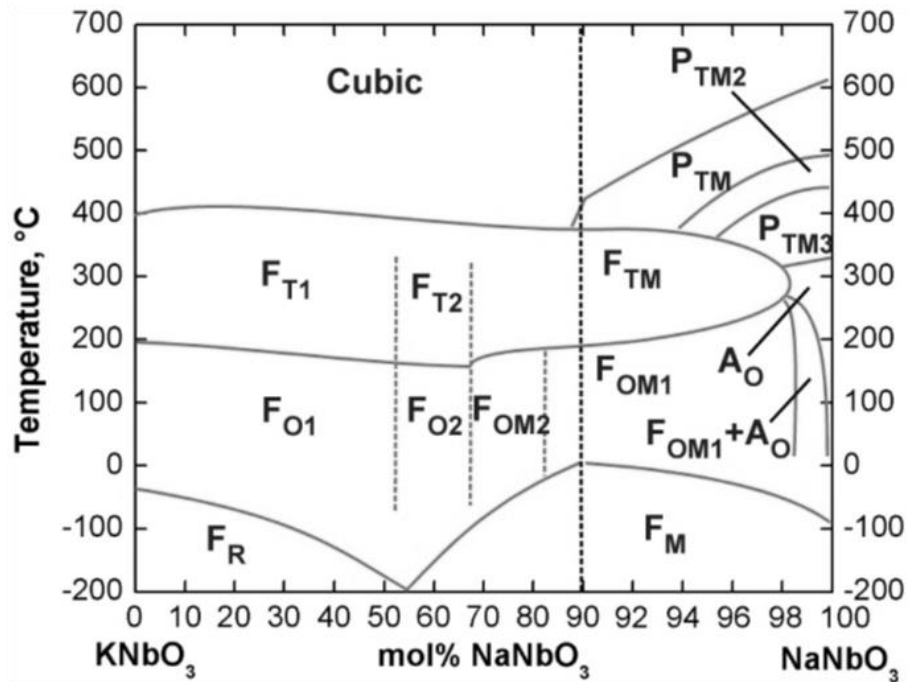


Fig. 1.6 Phase diagram of the KNN solid solution (F_R -ferroelectric rhombohedral with high potassium, F_M -ferroelectric monoclinic, F_{O1} -ferroelectric orthorhombic, F_{O2} -ferroelectric orthorhombic, F_{OM1} -ferroelectric orthorhombic field enforced in pure $NaNbO_3$, F_{OM2} -ferroelectric orthorhombic, F_{T1} -ferroelectric tetragonal with high potassium, F_{T2} -ferroelectric tetragonal, F_{TM} -ferroelectric tetragonal obtained with additives, A_O -antiferroelectric orthorhombic, P_C -paraelectric cubic, P_{OM} -paraelectric orthorhombic, P_{TM} -paraelectric tetragonal, P_{TM2} -paraelectric pseudo tetragonal, P_{TM3} -paraelectric pseudo tetragonal).³⁶⁾

BNT, as an expected replacement of lead-contained materials, shows the non-centrosymmetric rhombohedral symmetry structure and a high T_C of 320 °C. However, the difficulty of polarization caused by the large E_c of 73 kV/cm at room temperature (RT) and poor piezoelectric properties limits its practical application. The tetragonal phase BT is added in the BNT system to improve its properties. The MPB of $(1-x)(Bi,Na)TiO_3-xBaTiO_3$ (BNT- x BT) ceramics is in the range of $0.06 \leq x \leq 0.07$, as

shown in Fig. 1.7. These ceramics have low depolarization temperatures (T_d , 110-120 °C) and cannot be applied in a wide temperature range. BNT- x BT with MPB compositions exhibit complex phases such as coexisting rhombohedral and tetragonal phases.³⁸⁾ In addition, T_d 's of BNT- x BT ($x < 0.05$ & $x > 0.11$) are above 160 °C and they exhibit rhombohedral and tetragonal structures, respectively. 0.83(Bi,Na)TiO₃-0.17BaTiO₃ (BNT-17BT) exhibits the highest T_d of 209 °C.³⁹⁾ The application temperature improvement of the BNT- x BT thick films is another crucial subject in this study.

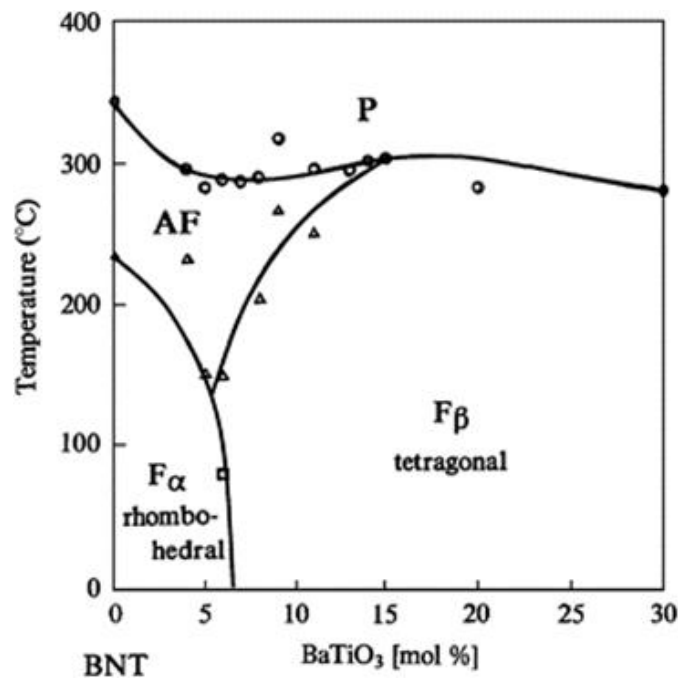


Fig. 1.7 Phase diagram of BNT- x BT. (F_{α} , ferroelectric rhombohedral phase; F_{β} , ferroelectric tetragonal phase; AF, antiferroelectric phase; P, paraelectric phase.)⁴⁰⁾

1.5 Films and Deposition Techniques

Thin film and thick film usually refer to nanometer and micrometer-level thickness films, respectively. However, the differences between thin film and thick film are not

only their thicknesses but their deposition processes as well. The progress of the exploration of thin film deposition techniques creates the possibility to manufacture new electronic equipment and mechanical parts with higher performances. High-integrated electronic films have been widely explored and applied. Piezoelectric films with high piezoelectric properties are practically applied in SAW substrates, ultrasonic micro-actuators, and infrared detectors. As stated above, in practical application, lead-contained piezoelectric films are still mainstream. Lead-free materials cannot completely substitute the lead-contained materials yet. Thus, research of lead-free films is necessary.

For thin films, the progress of the exploration of thin film deposition techniques provides the possibility to manufacture new electronic equipment or mechanical parts with higher performances. The deposition techniques are divided into three classifications: physical vapor deposition (PVD),^{41,42)} chemical vapor deposition (CVD),⁴³⁾ and solution-based chemistry (SBC).⁴⁴⁻⁴⁶⁾ Most of PVD and CVD methods require a vacuum condition. The growth rate of these deposition methods is usually slow and the cost is large to achieve excellent epitaxial growth.⁴⁷⁾ Generally, chemical methods offer lower cost and easier device requirements than other methods. In this study, Radiofrequency (RF) sputtering was used to prepare bottom electrodes, and the sol-gel deposition method was applied to prepare the precursor solution, respectively.

Sol-gel is a representative SBC thin film deposition technique which was discovered and used in 1846 by J. J. Ebelmenand to form silicate glass by hydrolyzing and inducing polycondensation of silicic acid.⁴⁸⁾ All sol-gel processes are started with the acquisition of precursors, whose compounds are small in molecular size. The first chemical reaction process is proceeded in a liquid solution at approximately room temperature. Precursors are converted into dispersed colloids, which could be either a

sol or a polymer solution. In the next process, the previously dispersed colloids were transformed into interconnected colloids which is called as “gel”. As the gel is dried, it comes up to the third process. After heat treatment in different conditions, various products could be obtained, such as glass, fiber, and ceramics.⁴⁹⁾ The advantages of sol-gel technique could be summarized as lower processing temperature, high homogeneity and purity of resulting materials, and possibility of various forming processes. Generally, sol-gel process contains two steps: hydrolysis reaction to form M-OH and condensation reaction to form metal oxide bonds, as shown in Fig. 1.8.

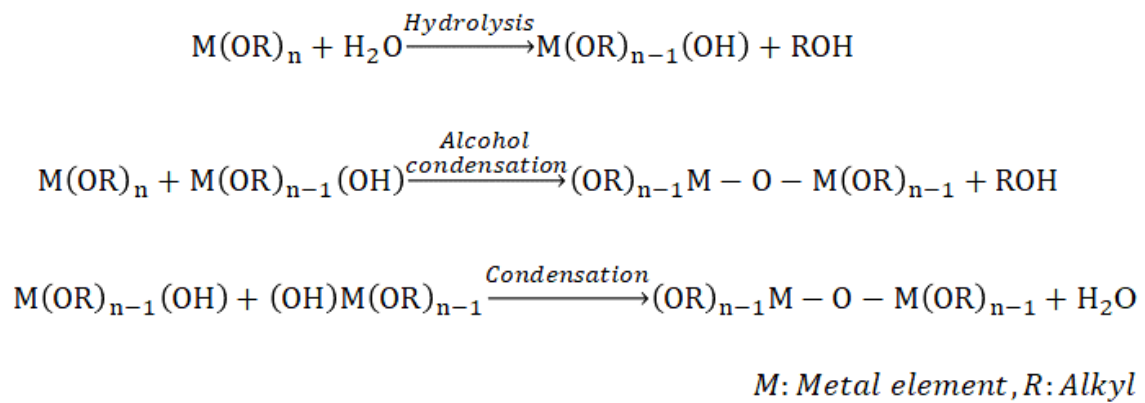


Fig. 1.8 General scheme of the sol-gel process mechanisms.

In a general sol-gel process, metallic alkoxides are used as the raw materials. Metallic alkoxides show high chemical activity and instability in water, resulting in its flammability in air. The Pechini method, also known as the polymeric precursor method, is a modified sol-gel method which could avoid using metallic alkoxides. The raw materials used in Pechini method are citric acid (CA, C₆H₈O₇) and carbonate mineral or metal hydroxide instead of alkoxide, thus there is no danger in raw material storage. The main reactions of this method contained: (1) chelation between metal cations from carbonate mineral or metal hydroxide and CA; (2) polyesterification of excess

hydroxycarboxylic acid with glycol,⁵⁰⁾ as shown in Fig. 1.9. In the preparation of thin films, the key point is a stable and transparent solution without precipitation in every step above. Thus, even though the Pechini technique is applied for multicomponent films theoretically, multicomponent films using this technique have not been extensively studied in practical.

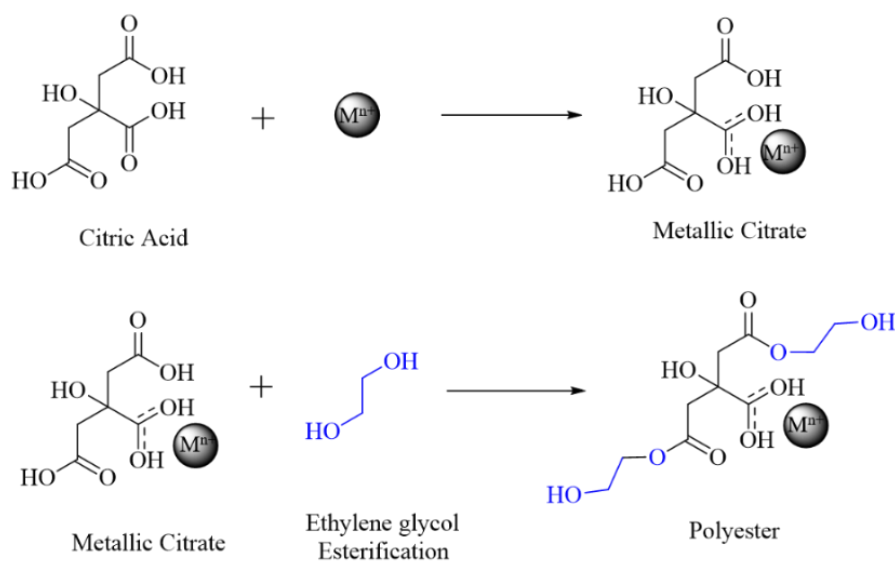


Fig. 1.9 Scheme of the Pechini method reactions.

Although the thin film deposition technology is ahead of the development of thin films, the research of piezoelectric thin film is still confined to simple composition thin films, especially for lead-free piezoelectric. Even the sol-gel deposition technology support for the complex composition thin film, due to the complexity of its processes and the severity of its chemical reactions, it has little effect on facilitating relevant research on multi-component lead-free piezoelectric thin film.

For thick film preparation, screen printing, spin coating, and tape casting are widely used. Regardless of any kind of thick film deposition technique, a stable ink plays an important role in it. Generally, the ink components contain solvent, surfactant,

dispersant, binder, and plasticizer. As a popular coating technique, screen printing possesses the technical specifications as below:

Thickness capability: 10-30 μm per layer, up to ~ 200 μm thick;

Ink viscosity range: 1-10 $\text{Pa}\cdot\text{s}$ (shear-thinning behavior acceptable);

Powder loading: 10-40 vol%.

Due to these beneficial properties, screen printing process was used in the thick film preparation of this study.

1.6 Thesis Objectives and Organization

1.6.1 Thesis objectives

KNN-based and BNT-based lead-free piezoelectric materials are the most promising candidates for PZT materials. This thesis focuses on the preparation of KNN-based thin films with MPB compositions and the using temperature improvement of BNT-based materials.

For KNN-based lead-free piezoelectric ceramics, there is no property temperature stability because of its inclined MPB. To improve the property temperature stability, the compositions of modified MPB in the lead-free piezoelectric KNN-system materials are always complicated. In previous studies, the so-called vertical MPB of BZ-KNLN-BNT/LNT was found in ceramics. However, these KNN-based lead-free piezoelectric thin films with the vertical MPB compositions, which are expected to be applied in high integration devices, have been studied less. The first purpose is to study lead-free BZ-KNLN-BNT/LNT thin film preparation using the Pechini method. Due to the precise control of composition ratios, the Pechini method is expected to prepare complicated

compositional films. However, in the field of piezoelectric materials, the Pechini method has not been used for composition systems larger than three elements. Preparing multi-component films proves to be a formidable challenge. Accordingly, in this study the Pechini method is expected to prepare multi-compositional films by the precise control of composition ratios.

On the other hand, lead-free piezoelectric BNT are respected to be another substitute of PZT-based materials due to the large P_r of $38 \mu\text{C}/\text{cm}^2$ and relatively high T_C of 320°C . However, BNT is difficult to polarize because its large E_c of $73 \text{ kV}/\text{cm}$ at room temperature. To improve this, BT has been introduced to BNT and the E_c was decreased to $30 \text{ kV}/\text{cm}$. Meanwhile, the addition of BT results in the decrease of T_d . Although BNT-BT lead-free piezoelectric ultrasonic vibrators have been already commercialized, their low T_d limit that they cannot be applied at high temperatures. The second objective of this thesis focuses on the improvement of the application temperature of BNT-BT thick film. Among BNT- x BT solid solutions, BNT-17BT shows the highest T_d and the phase transition is tetragonal to cubic with temperature increasing. The emphasis is on effects of prestress arising from the different coefficient of thermal expansion between BNT-17BT thick films and substrates.

Currently, lead-free piezoelectric materials are still unable to match lead-containing materials, as exemplified by piezoelectric properties and manufacture cost. Researches on lead-free materials are aimed to improve the piezoelectric properties to a usable level, and then to a substitutive level of lead-containing materials, finally and hopefully to an exceeded level of lead-containing materials. It is the vision of all researchers working on lead-free piezoelectric materials.

1.6.2 Thesis organization

This thesis consists 5 chapters. Chapter I introduces the research background and objectives. Chapter II describes the preparation and characterization methods of films. Chapter III shows the exploration of BZ-KNLN-BNT/LNT thin film preparation. Chapter IV discusses the prestress effects on lead-free BNT-17BT thick films. Chapter V states the conclusions of this research.

References

- 1) S. J. Zhang and F. Li, J. Appl. Phys. **111** [3](2012)031301.
- 2) J. Curie and P. Curie, Bulletin de Minéralogie (1880)90.
- 3) G. Lippmann, Annales de chimie et de physique **24** [145](1881) [in French].
- 4) J. C. Curie, Pierre Comptes Rendus **93** (1881)4. [in French].
- 5) G. H. Haertling, J. Am. Ceram. Soc. **82** [4](1999)797.
- 6) W. G. Cady, *Piezoelectricity; an introduction to the theory and applications of electromechanical phenomena in crystals* (McGraw-Hill Book Company, Inc., New York; London, 1946).
- 7) L. APC International, *Piezoelectric Ceramics: Principles and Applications* (APC International, 2011).
- 8) J.G. Webster, *The Measurement, Instrumentation and Sensors Hand Book* (1999).
- 9) L. F Chen, C. K Ong, C. P. Neo, V. V. Varadan, and V. K. Varadan, *Microwave Electronics: Measurement and Materials Characterization* (2004).
- 10) D. Feezell and S. Nakamura, Semiconductor Lasers (2013)221-271.
- 11) D. Berlincourt, O. Mattiat, and Y. Kikuchi, *Ultrasonic transducer materials* (Plenum Pub Corp, 1971).
- 12) Y. Xu, *Ferroelectric materials and their applications* (Elsevier, 2013).
- 13) M. Davis, *Phase transitions, anisotropy and domain engineering: the piezoelectric properties of relaxor-ferroelectric single crystals*. Verlag nicht ermittelbar (2006).

- 14) K.G. Webber, *Effect of domain wall motion and phase transformations on nonlinear hysteretic constitutive behavior in ferroelectric materials*, Georgia Institute of Technology (2008).
- 15) S. Zhang, F. Li, P. S. E., and S. T. R., J. Appl. Phys. **111** [3](2012) 031301.
- 16) A. Gruverman and A. Kholkin, Rep. Prog. Phys. **69** [8](2006)2443-2474.
- 17) M. Panjan, *Ferroelectrics and ferroelectric domains* (2003)
- 18) S. Mahajan, *Encyclopedia of Materials: Science and Technology* (2001).
- 19) M.J. Polking, A.P. Alivisatos, and R. Ramesh, MRS Commun. **5** [1](2015)27-44.
- 20) M. Acosta, N. Novak, V. Rojas, S. Patel, R. Vaish, J. Koruza, G. A. Rossetti, Jr., and J. Rodel, Appl. Phys. Rev. **4** (2017)041305.
- 21) A. Dubey. Piezoelectric Material (Future source of electricity). (2013).
- 22) D. Chapman, J. Appl. Phys. **40** [6](1969)2381-2385.
- 23) M. Francombe, Thin Solid Films **13** [2](1972)413-433.
- 24) B. Sharma, S. Vogel, and P. Prentky: Ferroelectrics **5** [1](1973)69-75.
- 25) M. Dawber, K.M. Rabe, and J. F. Scott, Rev. Mod. Phys. **77** [4](2005) 1083-1130.
- 26) C. F. Zhang, *Study on Preparation, Microstructure and Properties of High Curie Temperature Perovskite Piezoelectric Thin Films*. Tsinghua University (2011).
- 27) K. Lakin, and J. Wang, Appl. Phys. Lett. **38** [3](1981) 125-127.
- 28) W. Travis, E. N. K. Glover, H. Bronstein, D. O. Scanlon, and R. G. Palgrave, Chem Sci. **7** [7](2016)4548.
- 29) R. Roy, J. Am. Ceram. Soc. **37** [12](1954)581.
- 30) H. G. Wei, H. Wang, Y. J. Xia, D. P. Cui, Y. P. Shi, M. Y. Dong, C. T. Liu, T. Ding, J. X. Zhang, Y. Ma, N. Wang, Z. C. Wang, Y. Sun, R. B. Wei, and Z. H. Guo, J. Mater. Chem. C. **6** [46](2018)12446.

- 31) T. R. Shrout and S. J. Zhang, *J. Electroceramics* **19** [1](2007)113.
- 32) RosH. Available from: <https://www.assentcompliance.com/wpcontent/uploads/Guide-RoHS-Exemption-List-PC-GD-180717.pdf>.
- 33) W. F. Liu and X. B. Ren, *Phys. Rev. Lett.* **103** (2009)257602.
- 34) T. Karaki, T. Katayama, K. Yoshida, S. Maruyama, and M. Adachi, *J. J. Appl. Phys.* **52** [9S1](2013)09KD11.
- 35) R. Baba, T. Karaki, and T. Fujii, *J Adv Dielectr.* **06** [02](2016).
- 36) Kosec M., Malič B. Benčan A., and Rojac T., *Piezoelectric and Acoustic Materials for Transducer Applications*. (Springer, Boston, MA, 2008).
- 37) M. Hinterstein, L. Schmitt, M. Hoelzel, W. Jo, J. Rödel, H. J. Kleebe, and M. Hoffman, *Appl. Phys. Lett.* **106** [22](2015)222904.
- 38) C. Ma, X. Tan, E. Dul'kin, and M. Roth, *J. Appl. Phys.* **108** [10](2010)104105.
- 39) J. Lv, T. Karaki, and M. Adachi, *J. J. Appl. Phys.* **49** (2010) 09MD06.
- 40) T. Takenaka, K. Maruyama, and K. Sakata, *J. J. Appl. Phys.* **30** (1991)2236.
- 41) K. Tonisch, V. Cimalla, C. Foerster, H. Romanus, O. Ambacher, and D. Dontsov: *Sens. Actuators, A.* **132** [2](2006)658.
- 42) Y. Zhao, H. Wang, C. Wu, Z. F. Shi, F. B. Gao, W. C. Li, G. G. Wu, B. L. Zhang, and G. T. Du, *Vacuum* **103** (2014)14.
- 43) C. E. Morosanu, *Thin films by chemical vapour deposition* (Elsevier, 2016).
- 44) X. Xu, C. Xia, S. Huang, and D. Peng, *Ceram. Int.* **31** [8](2005)1061.
- 45) S. M. Rozati and S. Akesteh, *Mater. Charact.* **58** [4](2007)319.
- 46) I. Sta, M. Jlassi, M. Hajji, and H. Ezzaouia, *Thin Solid Films* **555** (2014)131.

- 47) M. S. El-Eskandarany, *Mechanical Alloying*. (2015).
- 48) A. C. Pierre, *Kirk-Othmer Encyclopedia of Chemical Technology* (John Wiley & Sons, Inc., 2007).
- 49) A. C. Pierre, *Introduction to Sol-Gel Processing* (Springer US, 2013).
- 50) L. Klein, M. Aparicio, and A. Jitianu, *Handbook of sol-gel science and technology*. (Springer International Publishing, Switzerland 2016).

CHAPTER II

PREPARATION AND CHARACTERIZATION OF FILMS

2.1 Introduction

For ferroelectric films, inchoate research can be traced back to the late 1960s and early 1970s.¹⁻³⁾ With the development and integration of Si devices, thin-film technologies attracted interest in the use of ferroelectric films to make non-volatile memories. CMOS⁴⁾ and MEMSs⁵⁾ were invented subsequently. Until now, microsystems, memories, and high-frequency electrical components are still the three main applications of ferroelectric thin films.

Thick films are films with a thickness range of 10-100 μm . Thick film technology was started in the 1950s and was one of the earliest microelectronic-enabling technologies.⁶⁾ Nowadays thick film technology is widely applied to manufacture electronic devices such as surface-mount devices, hybrid integrated circuits, heating elements, and sensors, especially for a mass of applications in the automotive industry. For piezoelectric thick films, the earliest introduction was in 1987 by Baudry.⁷⁾ During the studies of piezoelectric thick films, PZT materials⁸⁻¹⁰⁾ were always the mainstream. Piezoelectric thick films have been used in numerous applications, such as micropumps, accelerometers, ultrasonic motors, prosthetic hands-slip sensors, resonators, elastic wave sensors, multi-modal sensors, microfluidic separators, pyroelectric thick film sensors, and thick-film actuators.¹¹⁾

2.2 Preparation and Characterization of Thin Films

2.2.1 Preparation of substrates

Sliced Si substrates with a size of 1×2 cm were ultrasonically cleaned in deionized water, acetone, Semiko clean #23, and methyl alcohol for 10 min orderly. The single-crystal silicon substrates with diamond cubic structures were used as original substrates. In order to prepare well-oriented bottom electrodes, a SiO₂ layer that could prevent the interdiffusion of elemental Si¹⁹⁾ was prepared by an oxidation furnace. This oxidation furnace is designed to be in the gas flow regulation range of 0 to 5 atm and in the temperature range of 600 to 1000 °C. In this experiment, a 500 nm-thick SiO₂ layer could be formed on the surface of (100) Si for 1.5 h at 900 °C.

2.2.2 Preparation of bottom/top electrodes

To measure the electrical properties of the thin films, bottom/top electrodes with high conductivities were prepared using RF/DC (Radio Frequency/Direct Current) sputtering devices, respectively. Sputtering belongs to PVD, which is an atomic deposition process. In this process, the target materials can be solid or liquid. The atomic vapor of the target materials is evaporated and transported to the substrate as a vapor through either a vacuum, low-pressure gas, or plasma environment and then condensed on the substrate. DC sputtering is applied to metallic electric conductor target materials coatings such as Pt and Au instead of dielectric target materials coatings. RF sputtering is widely used in dielectric thin film preparation. The epitaxial growth of thin films is influenced by the orientation of the bottom electrode. Metallic and semi-conductive bottom electrodes with high electrical conductivity and orientation are

widely used for the epitaxial thin films. In this study, high oriented (100)-Pt/TiO₂ and (001)-LaNiO₃ (LNO) electrodes were prepared by the RF-sputtering method. In RF sputtering processes, the electrical potential of the current in the vacuum environment is alternated by radio frequencies to clean up the charge accumulation on the target materials in order to make the sputtering continue. The radio frequency of 13.56 MHz is an international standard.

2.2.3 Synthesis of the precursor solution

The Pechini process was selected for lead-free piezoelectric thin films. The Pechini method is a peculiar sol-gel method named after its inventor, M. P. Pechini.^{12,13)} The Pechini process is showed in Fig. 2.1. The raw materials used in the Pechini method are CA and carbonate minerals or metal hydroxide instead of alkoxide, which is used in common sol-gel process. Thus, there is no hydrolysis equilibria reaction in the process. The main reactions of this method contained the raw materials in the second reaction process are metallic citrates and ethylene glycol (EG). Next, the precursor solution undergoes the sol change and wet gel change with the heat treatment. In the end, ceramics or thin films would be produced with different heat treatment routes. For thin film preparation, the key point is the synthesis of stable and transparent metal-CA solution, sol, and wet gel. The Pechini process has been widely applied in preparation of solar cell with complex oxides.^{14,15)} However, complex oxide piezoelectric thin film has not been synthesized and studied yet. For the BZ-KNLN-BNT/LNT thin films, the raw materials of Nb, Zr, and Ti were difficult to react in the Pechini process. Their intermediate products that can react with CA solutions were explored. For the Nb source, the preparation of Nb₂O₅ · H₂O will be discussed. The powder Nb₂O₅ · H₂O was filtered by vacuum filtration and washed with an ultrasonic vibrator in deionized water. For Zr

and Ti sources, their hydrolysates from titanium butoxide $\{\text{Ti}[\text{O}(\text{CH}_2)_3\text{CH}_3]_4\}$ and zirconium butoxide $\{\text{Zr}[\text{O}(\text{CH}_2)_3\text{CH}_3]_4\}$ were used. With the exception of the three components above, other sources were prepared by normal Pechini processes. In addition, due to the complicated compositions, the reactants in the synthesis interact each other, and the preparation conditions in each step will be discussed in chapter III

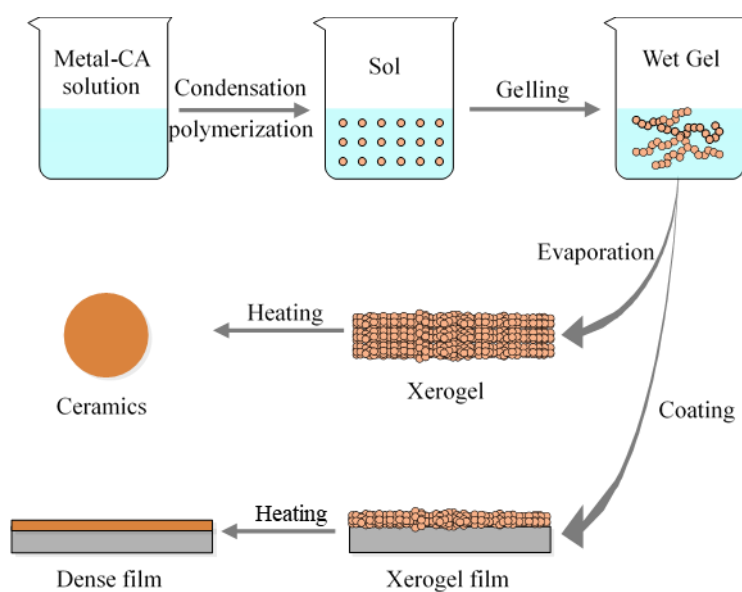


Fig. 2.1 Schematic diagram of the Pechini process.

2.2.4 Spin-coating deposition

The gel solution was dropped and spin-coated onto the substrates. Simultaneously, in the second spin-coating step, a halogen point heater (HPH-30A/f30, HEAT-TECH Co., Ltd.) was applied to dry the coating layer in air at 120 °C, as shown in Fig. 2.2. The thin film surface temperature was measured by a radiation thermometer (AD-5616, A&D Co., Ltd). Usually, the inorganic components of thin films are evaporated in drying oven. By using the halogen point heater, the thin film preparation process is simplified.

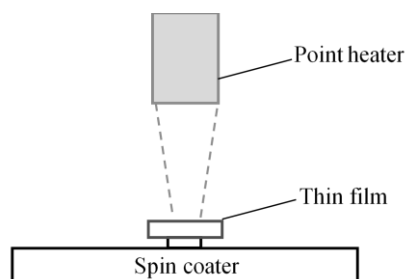


Fig. 2.2 Schematic of spin-coater (MS-B100, MIKASA Co., Ltd) with the point heater.

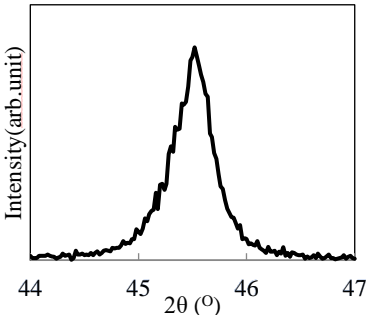
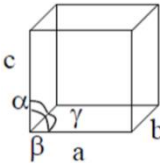
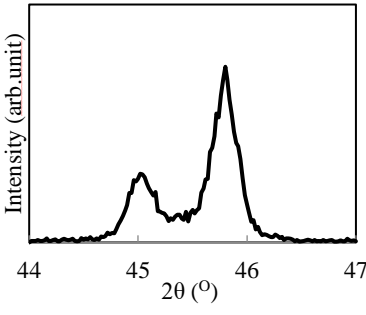
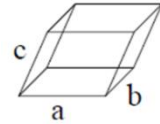
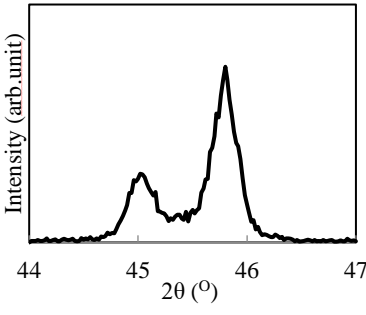
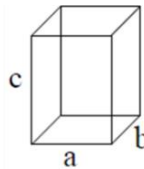
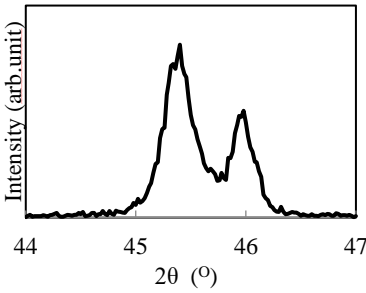
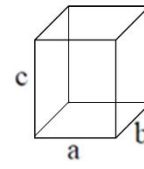
2.2.5 TG/DTA

In this experiment, TG/DTA (thermogravimetric & differential thermal analysis) was measured with the EXSTAR6000 series (SII Nano-Tech Inc.). From the TG/DTA curve, the heat treatment reaction processes of the precursor solutions could be analyzed and then the heat treatment conditions of thin film specimens could be decided.

2.2.6 X-ray diffraction analysis

The phase analysis of powders from heated precursor solutions is based on the patterns measured by X-ray diffraction (XRD) diffractometer (RINT2200) with Cu K_{α} radiation operated at 40 kV and 40 mA. The crystal structure data is from the release 2004 of the powder diffraction file (PDF) by using the JADE 6.0 software (Materials Data, Inc.). As shown in table 1-1, the crystal structure is determined by the (200) peak around $2\theta = 45^{\circ}$, which is a structure characteristic peak of the perovskite structure. A single peak represents either the cubic or rhombohedral phase. Twin peaks with a stronger right peak indicate the tetragonal phase. Twin peaks with a stronger left peak indicate the orthorhombic phase.

Table 1.2 Relationship of (200) peak pattern and crystal phase.

| (200) Peak pattern | Crystal phase |
|---|---|
|  |  <p data-bbox="995 349 1054 376">Cubic</p> <p data-bbox="938 398 1230 432">$a = b = c, \alpha = \beta = \gamma = 90^\circ$</p> |
|  |  <p data-bbox="986 517 1129 544">Rhombohedral</p> <p data-bbox="954 577 1273 611">$a = b = c, \alpha = \beta = \gamma \neq 90^\circ$</p> |
|  |  <p data-bbox="995 808 1098 835">Tetragonal</p> <p data-bbox="932 857 1262 891">$a = b \neq c, \alpha = \beta = \gamma = 90^\circ$</p> |
|  |  <p data-bbox="991 1182 1129 1209">Orthorhombic</p> <p data-bbox="932 1243 1241 1276">$a \neq b \neq c, \alpha = \beta = \gamma = 90^\circ$</p> |

2.2.7 Scanning electron microscopy

Morphology photos were taken with a scanning electron microscopy (SEM) (S-300N) and the crystalline state and thickness were identified. Additionally, this system was also used for Energy dispersive X-ray analysis (EDXA).

2.3 Preparation and Characterization of Thick Films

The screen-printing method was used in the fabrication of the thick film and the bottom/upper electrodes. As shown in Fig. 2.3, the particles were arranged in order by printing the paste through a multi mesh screen. To prepare thick films, several layers would be printed on the substrate repeatedly.

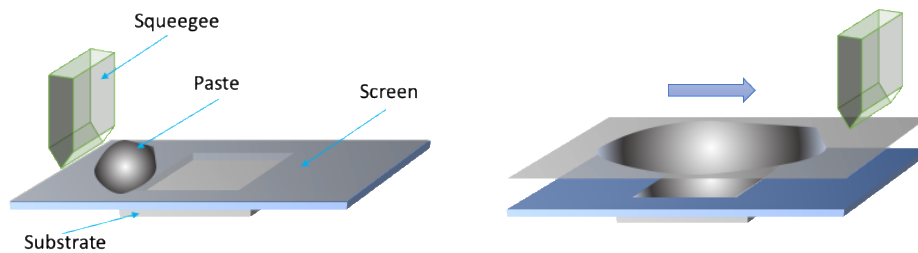


Fig. 2.3 The process of screen-printing.

Thermomechanical analysis (TMA; SIIEXSTAR6000) was used to measure the thermal expansion coefficient of bulk ceramics with increasing temperature. Room-temperature and high-temperature XRD (Rigaku Smart Lab.) were used to characterize the crystalline phase and residual stress of the thick films. Residual stress was measured with two-dimensional X-ray diffraction (XRD²). Fig. 2.4 (a) shows the geometric definition of diffraction cones in the laboratory coordinates system, $X_L Y_L Z_L$. The stress measurement is based on the fundamental relationship between the stress tensor and the diffraction cone distortion. Fig. 2.4 (b) shows a diffraction cone cross-section on a 2D detector plane. The 2θ is a functional relationship with respect to γ , $2\theta = 2\theta(\gamma)$.

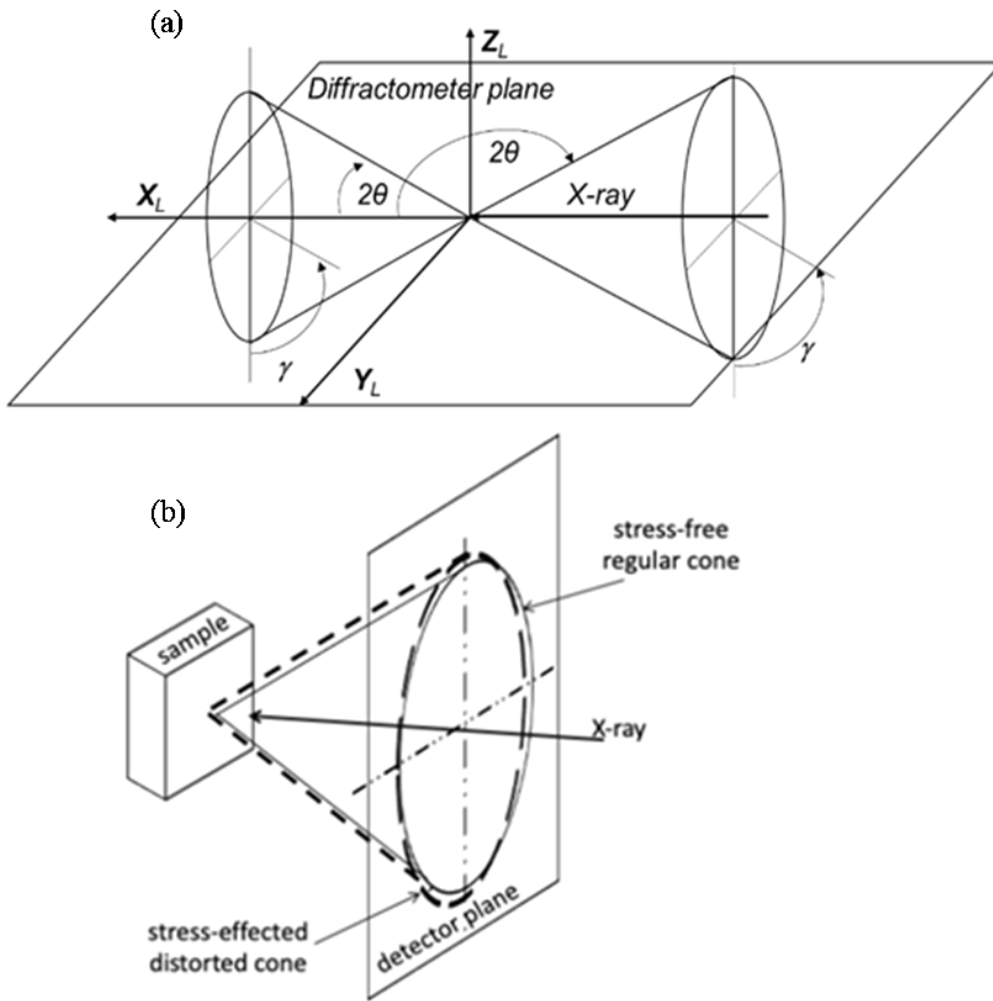


Fig. 2.4 The geometric definition of diffraction rings in laboratory axes (a) and Diffraction cone distortion due to stress (b).¹⁶⁾

The fundamental equation for strain measurement using 2D detector is given by He and Smith in 1998:¹⁶⁾

$$f_{11}\varepsilon_{11} + f_{12}\varepsilon_{12} + f_{22}\varepsilon_{22} + f_{13}\varepsilon_{13} + f_{23}\varepsilon_{23} + f_{33}\varepsilon_{33} = \ln\left(\frac{\sin\theta_0}{\sin\theta}\right) \quad (2-1)$$

$$f_{11} = h_1^2$$

$$f_{12} = 2h_1h_2$$

$$f_{13} = 2h_1h_3$$

$$f_{22} = h_2^2$$

$$f_{23} = 2h_2h_3$$

$$f_{33} = h_3^2$$

$$(2-2)$$

$$\begin{aligned}
h_1 &= a \cos \phi - b \cos \psi \sin \phi + c \sin \psi \sin \phi \\
h_2 &= a \sin \phi + b \cos \psi \cos \phi - c \sin \psi \cos \phi \\
h_3 &= b \sin \psi + c \cos \psi
\end{aligned} \tag{2-3}$$

$$\begin{aligned}
a &= \sin \theta \cos \omega + \sin \gamma \cos \theta \sin \omega \\
b &= -\cos \gamma \cos \theta \\
c &= \sin \theta \sin \omega - \sin \gamma \cos \theta \cos \omega
\end{aligned} \tag{2-4}$$

where ε_{ij} is the strain, f_{ij} is the strain coefficient determined by the specimen orientation and the direction of the diffraction vector at each data point on the diffraction ring, h_i is the component of the unit vector \mathbf{H}_{hkl} of the diffraction vector expressed in specimen coordinates, and $\ln\left(\frac{\sin \theta_0}{\sin \theta}\right)$ expresses the distortion of the diffraction cone at a specific $(\gamma, 2\theta)$ position. To isotropic materials,

$$\begin{aligned}
S_1 &= -\frac{\nu}{E} \\
\frac{S_2}{2} &= \frac{1+\nu}{E}
\end{aligned} \tag{2-5}$$

where S is the macroscopic elastic constant, E is Young's modulus, and ν is Poisson's ratio. Then the equation (2-1) changed to

$$P_{11}\sigma_{11} + P_{12}\sigma_{12} + P_{22}\sigma_{22} + P_{13}\sigma_{13} + P_{23}\sigma_{23} + P_{33}\sigma_{33} = \ln\left(\frac{\sin \theta_0}{\sin \theta}\right) \tag{2-6}$$

where

$$\begin{aligned}
P_{ij} &= \frac{1}{E} [(1 + \nu)f_{ij} - \nu] = S_2 \frac{f_{ij}}{2} + S_1 & i = j \\
P_{ij} &= \frac{1}{E} (1 + \nu)f_{ij} = S_2 \frac{f_{ij}}{2} & i \neq j
\end{aligned} \tag{2-7}$$

By fitting the integral to each diffraction ring, $(\gamma, 2\theta)$ data points could be obtained. The stress tensor could be fitted to the data points by least-squares method. Equation (2-1) can be written as:

$$S_1(\sigma_{11} + \sigma_{22} + \sigma_{33}) + \frac{S_2}{2}(\sigma_{11}h_1^2 + \sigma_{22}h_2^2 + \sigma_{33}h_3^2 + 2\sigma_{12}h_1h_2 + 2\sigma_{13}h_1h_3 + 2\sigma_{23}h_2h_3) = \ln\left(\frac{\sin\theta_0}{\sin\theta}\right) \quad (2-8)$$

An impedance analyzer was used to measure the temperature dependence of the capacitance and the dielectric loss factor ($\tan\delta$) of the specimens. An atomic force microscope (MFP-3D Infinity) was used to investigate the domain structures of the thick films. The temperature dependence of the piezoelectric coefficients was measured by a quasi-static piezo d_{33} meter (ZJ-6B). A ferroelectric test system (Toyo FCE-2) was applied to measure the P - E hysteresis loops at 100 Hz.

References

- 1) D. Chapman, J. Appl. Phys. **40** [6](1969)2381.
- 2) M. Francombe, Thin Solid Films **13** [2](1972)413.
- 3) B. Sharma, S. Vogel, and P. Prentky, Ferroelectrics **5** [1](1973)69.
- 4) S. S. Eaton, Dig. Tech. Pap. IEEE Int. Solid-State Circuit Conf. **31** (1988)130.
- 5) P. Rai-Choudhury, *MEMS and MOEMS Technology and Applications* (2000).
- 6) N. White, *Springer Handbook of Electronic and Photonic Materials* (2017).
- 7) H. Baudry, Microelectron. Int. **4** [3](1987)71.
- 8) H.D. Chen, K.R. Udayakumar, C.J. Gaskey, L.E. Cross, J.J. Bernstein and L.C. Niles, J. Am. Ceram. Soc. **79** [8](1996)2189.
- 9) E. S. Thiele and N. Setter, J. Am. Ceram. Soc. **83** [6](2004)1407.
- 10) T. Papakostas, N. Harris, S. Beeby, and N. White, Eurosensors XII (1998)461.
- 11) N. M. White, S. P. Beeby, and N. J. Grabham, *Electroceramic-Based MEMS: Fabrication Technology and Applications* (2005).
- 12) M. P. Pechini, US Patent US3330697A (1967).
- 13) M. P. Pechini, CA Patent CA 759914 (1967).
- 14) M. Kunduraci and G. G. Amatucci, J. Electrochem. Soc. **153** [7](2006)A1345.
- 15) H. S. Kim, S. P. Yoon, J. W. Yun, S. A. Song, S.C. Jang, S. W. Nam and Y.G. Shul, Int. J. Hydrog. Energy. **37** [21](2012)16130.
- 16) B. B. He: Powder Diffr. **18** [2](2012)71.

CHAPTER III

MULTICOMPONENT LEAD-FREE THIN FILMS

3.1 Introduction

KNN-based lead-free piezoelectric materials¹⁻⁵⁾ have been scientifically attractive and widely reported due to their large d_{33} and high T_C . However, the MPB of these lead-free piezoelectric materials are inclined. Among these KNN systems, the so-called vertical MPB of BZ-KNLN has been discovered by using rhombohedral BNT as the third component.⁶⁾ The piezoceramics with the composition near MPB exhibited the temperature stability of the piezoelectric properties in a wide temperature range. However, due to the evaporation of Bi_2O_3 in the sintering process, La, which shows a same +3 oxidation state and an atomic radius of 187 pm, was considered a substitution of Bi according to the Goldschmidt tolerance factor t . The existence of vertical MPB in BZ-KNLN-LNT ceramics substituting La for Bi were confirmed.⁷⁾ However, the thin films with this composition were not attractive enough by other researchers. Although these multicomponent ceramics with vertical MPB compositions exhibit the excellent temperature stability of piezoelectric properties, the complexity of composition restricts the development of the thin films. PVD⁸⁻¹⁰⁾ and CVD^{11,12)} cannot be used to prepare multicomponent oxide films because the application of gas during the deposition will negatively affect the condensation of vapor onto the substrates. In this part, a modified Pechini process to prepare the multicomponent precursor solution method is proposed

for first time, and the multicomponent thin films are prepared successfully and characterized. In addition, some complex components were successfully synthesized within the precursor solution.

3.2 Experiment

3.2.1 Selection of raw materials

The first step of Pechini method is the chelation between metal cations from metal salt and CA. The ionization state distribution diagram of CA is shown in Fig. 3-1. With the pH value increasing, the primary ionization, secondary ionization, and tertiary ionization of CA occurs sequentially. The max quantity of the primary ionization product AH_2^- is at a pH value of 4. As shown in Fig. 1.8, the reaction in the first step of Pechini process is the primary ionization product AH_2^- and metal carbonates or metal hydroxides. Consequently, the excess of CA is a necessity for the CA solution.

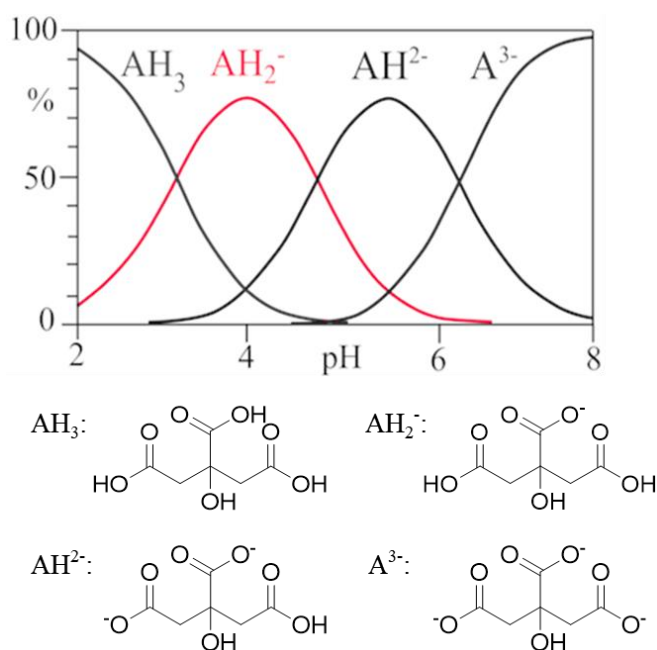


Fig. 3.1 Ionization state distribution diagram of CA (A: $C_6H_5O_7$).¹³⁾

Carbonate mineral or metal hydroxide would be the best selection due to their acid-based neutralization with CA. For the compositions of BZ-KNLN-BNT/LNT, sodium carbonate (Na_2CO_3), potassium carbonate (K_2CO_3), Lithium carbonate (Li_2CO_3), and lanthanum carbonate [$\text{La}_2(\text{CO}_3)_3$] are water-soluble carbonate minerals and can be used directly. However, barium carbonate (BaCO_3) is not dissolved in water but it is soluble in the CA solution. And bismuth (III) nitrate [$\text{Bi}(\text{NO}_3)_3 \cdot 5\text{H}_2\text{O}$] could also be solubilized in the CA solution and used as one of the raw materials.

For the niobium (Nb) source, there is not a commercial raw material that reacts with CA, but $\text{Nb}_2\text{O}_5 \cdot n\text{H}_2\text{O}$ [$\text{Nb}(\text{OH})_5$] is a usable powder material that can be prepared from niobium pentoxide (Nb_2O_5) as follows:^{14,15)}

The powder of Nb_2O_5 was added into HF in a hot water bath of 80 °C. After the solution became transparent, $\text{NH}_3 \cdot \text{H}_2\text{O}$ was dropped into the solution until the pH value to 8. The liquid mixture containing white precipitate was kept in a drying oven for 12 h. The powder was filtered by vacuum filtration and washed with an ultrasonic vibrator in deionized water. The cycle of filtering and washing was repeated 3-4 times until a pH value of 7 was achieved. $\text{Nb}_2\text{O}_5 \cdot n\text{H}_2\text{O}$ powder was obtained after drying for 10 h. In the previous studies, $(\text{NH}_4)_2\text{C}_2\text{O}_4$ was added after adding $\text{NH}_3 \cdot \text{H}_2\text{O}$, as shown in Fig 3.2 (a).^{14,15)} The NH_4^+ from $(\text{NH}_4)_2\text{C}_2\text{O}_4$ played the role in promoting the generation of $\text{Nb}_2\text{O}_5 \cdot n\text{H}_2\text{O}$. In this study, the pH values were controlled from 8-12 by adjusting the dosage of $\text{NH}_3 \cdot \text{H}_2\text{O}$ and meanwhile the dosage of $(\text{NH}_4)_2\text{C}_2\text{O}_4$ was reduced, as shown in Fig 3.2 (b). Finally, at the pH value of 10, $\text{Nb}_2\text{O}_5 \cdot n\text{H}_2\text{O}$ was also prepared successfully without using $(\text{NH}_4)_2\text{C}_2\text{O}_4$, as shown in Fig 3.2 (c). Compared the XRD pattern of the product and the PDF card of $\text{Nb}_2\text{O}_5 \cdot n\text{H}_2\text{O}$ in Fig. 3-3 (a, b), it was confirmed that the product without using $(\text{NH}_4)_2\text{C}_2\text{O}_4$ was also $\text{Nb}_2\text{O}_5 \cdot n\text{H}_2\text{O}$. Due to

the existence of $(\text{NH}_4)_2\text{C}_2\text{O}_4$ is not in the following cleaning process, the washing of the product is easy and the cost was reduced.

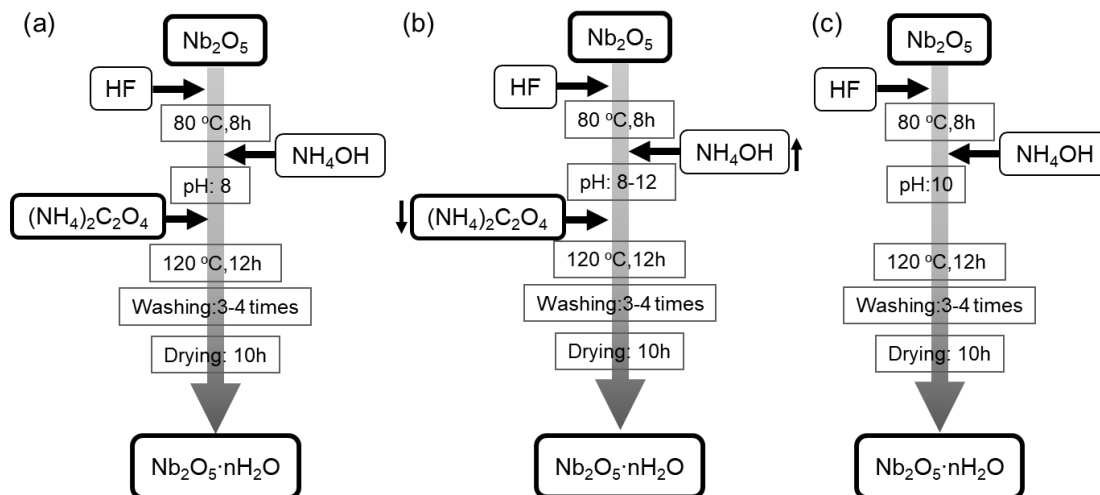


Fig. 3.2 Synthesis route of $\text{Nb}_2\text{O}_5 \cdot n\text{H}_2\text{O}$ [$\text{Nb}(\text{OH})_5$].

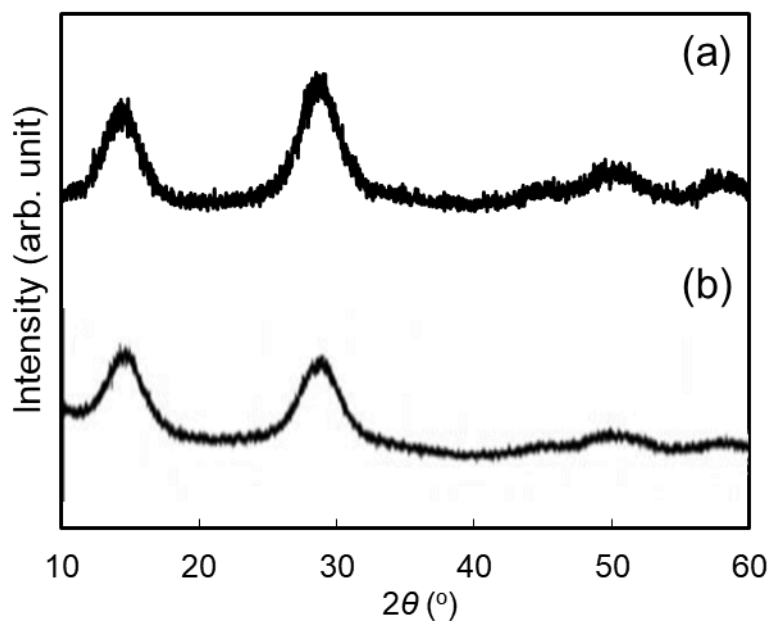
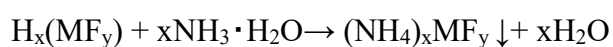


Fig. 3.3 (a) XRD pattern of the product without using $(\text{NH}_4)_2\text{C}_2\text{O}_4$ and (b) PDF card of $\text{Nb}_2\text{O}_5 \cdot n\text{H}_2\text{O}$.

The carbonates and hydroxides of the titanium and zirconium were unstable in their natural state. In first step of this study, their hydrates were expected to be prepared in the same manner as Nb because they are near to Nb in the periodic table. However, the XRD patterns of prepared powders (Fig. 3-4) showed that the productions were $(\text{NH}_4)_2\text{TiF}_6$ (PDF#30-0067) and $(\text{NH}_4)_3\text{ZrF}_7$ (PDF#07-0024). The reaction process is written as:



M: Ti, Zr;

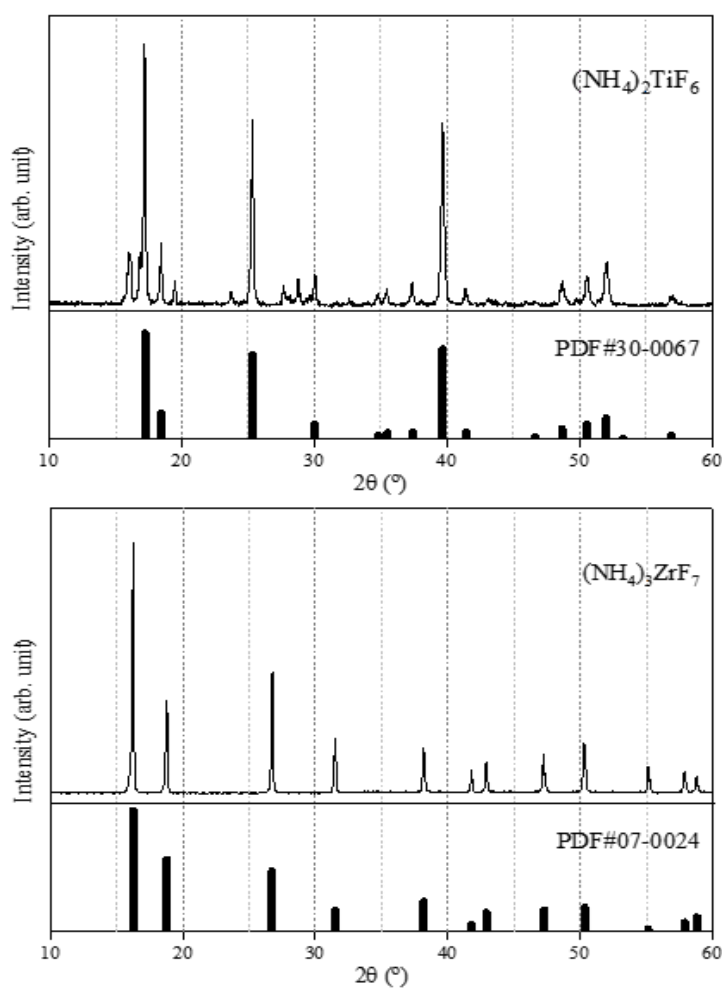


Fig. 3.4 XRD patterns of prepared powders.

Lastly, titanium butoxide $\{\text{Ti}[\text{O}(\text{CH}_2)_3\text{CH}_3]_4\}$ and zirconium butoxide $\{\text{Zr}[\text{O}(\text{CH}_2)_3\text{CH}_3]_4\}$ were attempted to react with the CA solution in the Pechini process. The sediments initially appeared and then disappeared in CA solution at 80 °C due to the sediments of hydroxides reacting with CA at high temperature. Finally, the titanium butoxide and zirconium butoxide were chosen as raw materials of the Ti and Zr sources, respectively.

The information on the chemical formula, purity, molecular weight, and manufacturer of the raw materials are listed in Table 3-1.

Table 3.1 Information on raw materials.

| Chemical formula | Purity (%) | Molecular weight | Manufacturer |
|--|------------|------------------|--------------|
| K_2CO_3 | 99.5 | 138.21 | Wako |
| Na_2CO_3 | 99.8 | 105.99 | Wako |
| Li_2CO_3 | 99.99 | 73.8874 | Kojundo |
| $\text{La}_2(\text{CO}_3)_3$ | 90 | 457.84 | Wako |
| BaCO_3 | 99.95 | 197.34 | Kojundo |
| $\text{Bi}(\text{NO}_3)_3 \cdot 5\text{H}_2\text{O}$ | 99.5 | 485.07 | Wako |
| Nb_2O_5 | 99.9 | 265.809 | Kojundo |
| HF | 46 | 20.01 | Wako |
| $\text{NH}_3 \cdot \text{H}_2\text{O}$ | 17.03 | 28 | Wako |
| $\text{Ti}[\text{O}(\text{CH}_2)_3\text{CH}_3]_4$ | 95 | 340.33 | Wako |
| $\text{Zr}[\text{O}(\text{CH}_2)_3\text{CH}_3]_4$ | 85 | 383.68 | Wako |
| $\text{C}_6\text{H}_8\text{O}_7$ | 98.0 | 192.12 | Wako |
| $(\text{CH}_2\text{OH})_2$ | 99.5 | 65.07 | Wako |
| $(\text{NH}_4)_2\text{C}_2\text{O}_4$ | 99.5 | 142.11 | Wako |

* Wako: Wako Pure Chemical Industries, Ltd.

Kojundo: Kojundo Chemical Laboratory Co.Ltd.

3.2.2 Exploration of the precursor solution synthesis

In the early stages of the experiment, carbonates and CA were directly added into deionized water similar to the processes of other simple component thin films, and the prepared Ti/Zr salts $\{(\text{NH}_4)_2\text{TiF}_6 \& (\text{NH}_4)_3\text{ZrF}_7\}$ were used to prepare the all component

precursor solutions. The conditions are listed in Table 3-2. However, due to the multi-element components, the precipitation occurred regardless of changing ratios of CA and EG, as shown in Fig. 3-5.

To determine the reason for the appearance of precipitation, condition No. 5 was selected and metal source solutions were prepared, respectively. The photos show the reacted solutions, and solutions which used the prepared Ti/Zr salts produced precipitation. On the contrary, other metal solutions were transparent without precipitation.

Table 3.2 Preparing conditions and statuses of precursors.

| No. | CA/EG | Time (h) | Temp. (°C) | Color | Precipitation |
|-----|-------|----------|------------|--------------|---------------|
| 1 | 1:1 | 12 | 80 | white | Yes |
| 2 | 1:2 | 12 | 80 | white yellow | Yes |
| 3 | 1:3 | 12 | 80 | yellow | Yes |
| 4 | 1:4 | 20 | 80 | brown | Yes |
| 5 | 1:5 | 20 | 80 | dark brown | Yes |
| 6 | 1:6 | 20 | 80 | white yellow | Yes |

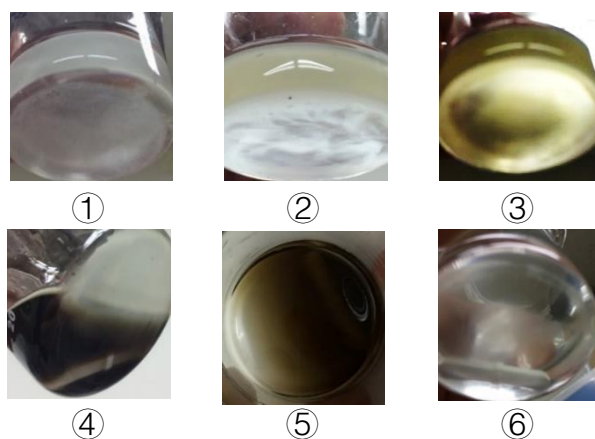


Fig. 3.5 Photographs of prepared precursor solutions.

Table 3.3 Preparing conditions and statuses of metal solutions.

| Metallic salts | BaCO ₃ | Li ₂ CO ₃ | K ₂ CO ₃ &Na ₂ CO ₃ | Nb ₂ O ₅ ·nH ₂ O | (NH ₄) ₂ TiF ₆ | (NH ₄) ₂ ZrF ₆ | Bi(NO ₃) ₃ ·5H ₂ O |
|--------------------------|---|---|---|---|--|---|---|
| M ^{x+} : CA: EG | | | | 1:3:15 | | | 1:30:150 |
| Time (h) | | | | 20 | | | 20 |
| Temp. (°C) | | | | 80 | | | 80 |
| pH | | | | 8 | | | 8 |
| State after heating |  |  |  |  |  |  |  |

Afterwards, titanium/zirconium butoxides were used as raw materials as stated in Chapter 3.2.1. By controlling the temperature, pH, and the ratios of metal ion and CA, transparent individual metal-CA solution sources were obtained. Consequently, the multicomponent precursor solutions were prepared successfully by mixing the different metal-CA solution sources. Compared to simple component thin film, this step was an improvement of the Pechini process for multi-component chemical compounds.

The synthesis route and conditions of stable precursor solutions are shown in Fig. 3-6 and Table 3-4. Nb₂O₅·nH₂O was dissolved in the CA solution by mixing for 12 h. Then a small amount of Nb source solution was heated at 900 °C for 2 h in a platinum crucible. The molarity of Nb was calculated as follows:

$$b = \frac{N \times (m_3 - m_1)}{M \times (m_2 - m_1)} \quad (3-1)$$

where b is the molarity, N is Nb atomic number in Nb₂O₅, M is the molar the weight of Nb₂O₅, m_1 is the weight of platinum crucible, m_2 is the weight of the Nb source solution (including the platinum crucible), and m_3 is the weight of prepared Nb₂O₅ (including the platinum crucible).

Na₂CO₃, K₂CO₃ and Li₂CO₃ were directly dissolved in the CA solution, respectively. BaCO₃ was dissolved in the CA solution and then the pH was quickly adjusted to 8 by adding NH₃·H₂O. La₂(CO₃)₃ was added into the CA solution and then

adjusted the pH value of 8 by dropping $\text{NH}_3 \cdot \text{H}_2\text{O}$. La source was obtained after mixing for 12 h. $\text{Bi}(\text{NO}_3)_3 \cdot 5\text{H}_2\text{O}$ was dissolved in the alkali CA solution. By heating the mixtures of $\text{Ti}[\text{O}(\text{CH}_2)_3\text{CH}_3]_4/\text{Zr}[\text{O}(\text{CH}_2)_3\text{CH}_3]_4$ and CA solutions at 80°C until the solutions became transparent, the Ti and Zr sources were obtained, respectively. The molarities of each metal source could be calculated as the same as equation (3-1). The metal sources were then mixed at the demanded composition ratios. Finally, ethylene glycol (EG) was added to the mixture above at different CA/EG ratios of 1/3, 1/4, and 1/5, and the pH value was subsequently adjusted to 10 by adding $\text{NH}_3 \cdot \text{H}_2\text{O}$. However, after the chelation process at 120°C for 24 h, sediments appeared in the solutions at CA/EG ratios of 1/3 and 1/5. Thus, the CA/EG ratio of 1/4 was chosen to prepare the stable precursor.

The elements used in this study include almost all elements used in lead-free piezoelectric materials, so the precursor solutions of other piezoelectric materials could be prepared easily by using the prepared metal sources.

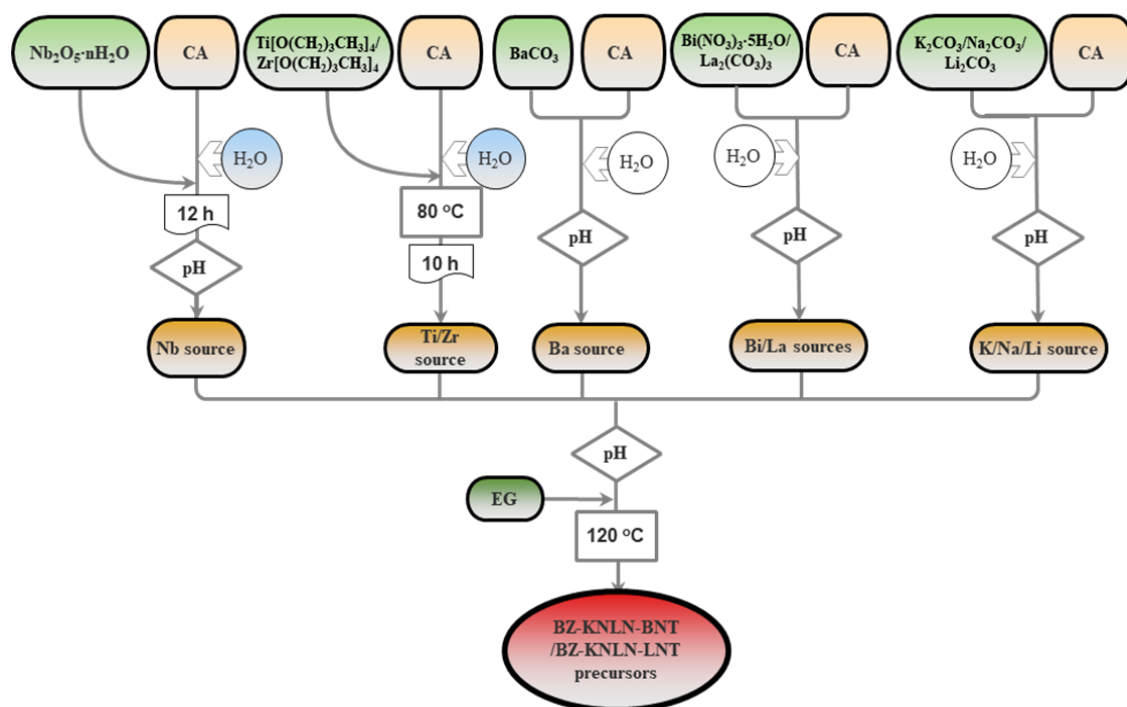


Fig. 3.6 Synthesis route of BZ-KNLN-BNT/LNT precursors.

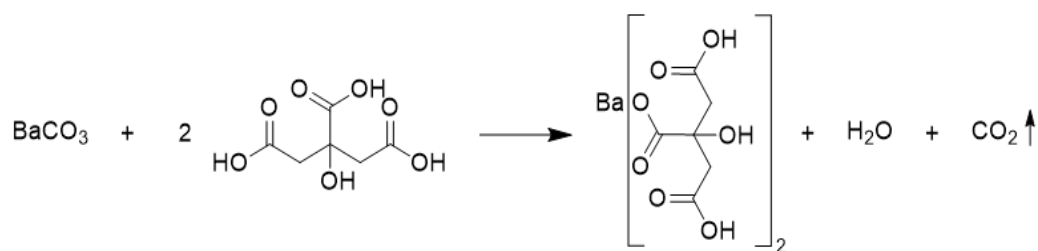
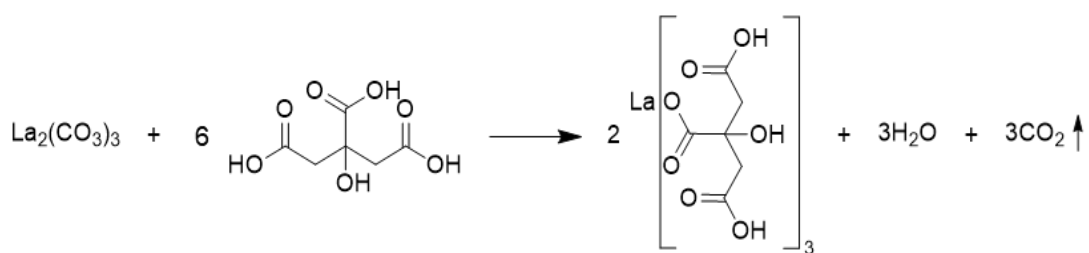
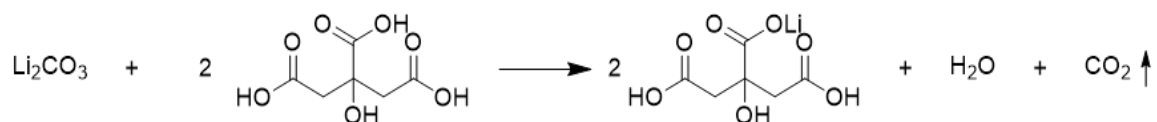
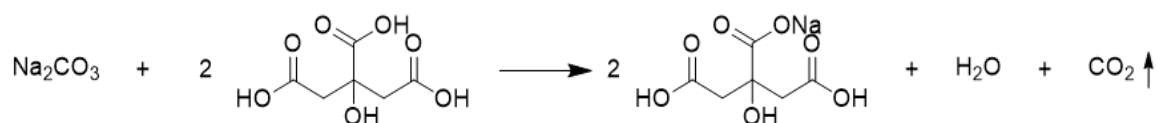
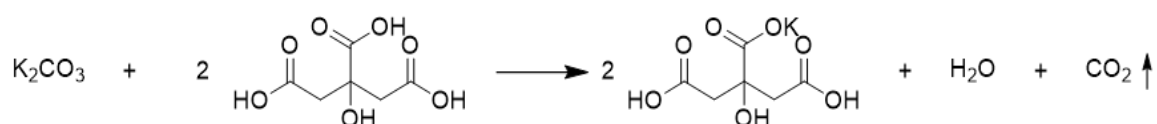
Table 3.4 Preparing conditions of metal-CA solutions.

| Metal-CA | Metal:CA (mol) | pH | Temp. (°C) |
|------------|----------------|----|------------|
| Nb-CA | 1:3 | 8 | - |
| Ba-CA | 1:3 | 8 | - |
| K&Na&Li-CA | 1:3 | - | - |
| Bi-CA | 1:30 | 8 | - |
| La-CA | 1:30 | 8 | - |
| Ti-CA | 1:30 | - | 80 |
| Zr-CA | 1:30 | - | 80 |

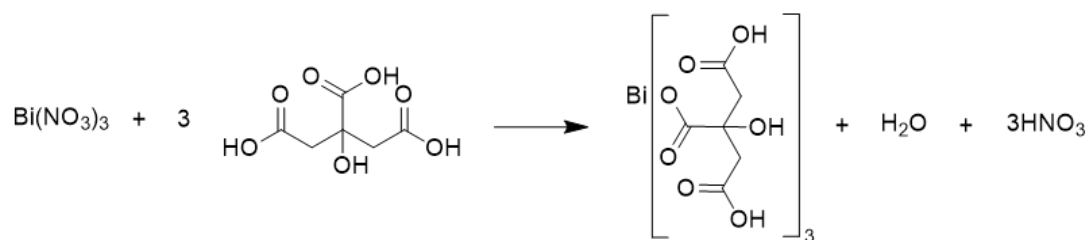
*“-”: no controlling.

Here, the reaction mechanism of precursor solution synthesis will be described in the following equations.

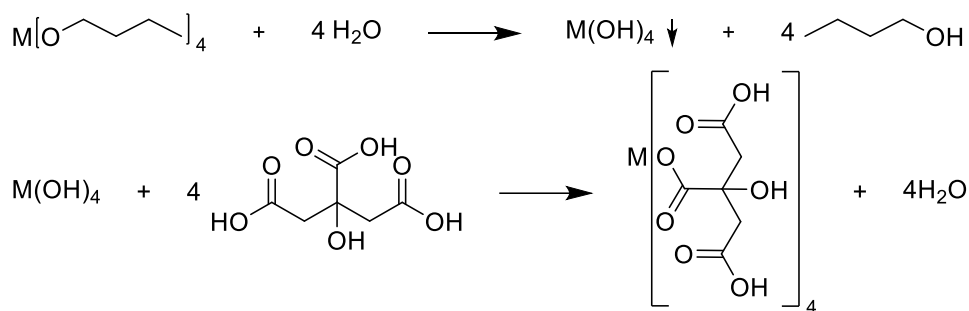
The reactions between carbonates and CA are:¹⁶⁾



The $\text{Bi}(\text{NO}_3)_3$ dissolved in CA aqueous solution:¹⁷⁾

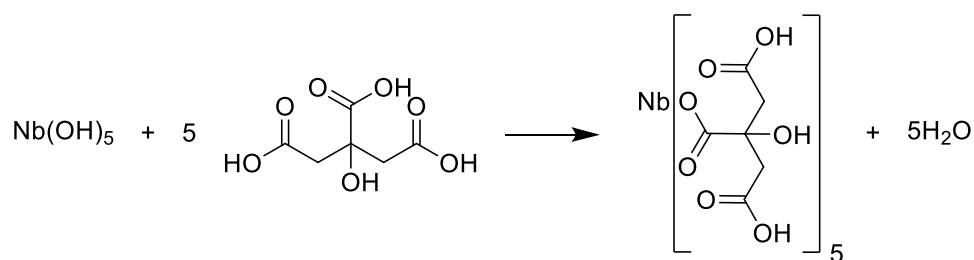
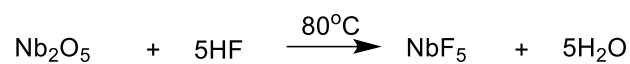


The process of Ti and Zr source preparation:

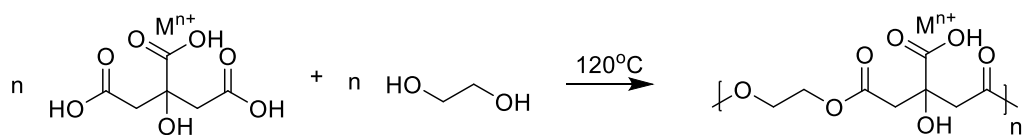


M: Ti;Zr

The preparation of $\text{Nb}_2\text{O}_5 \cdot n\text{H}_2\text{O}$ [$\text{Nb}(\text{OH})_5$]:



The polycondensation between metal-CA and EG:



M^{n+} : metallic cations.

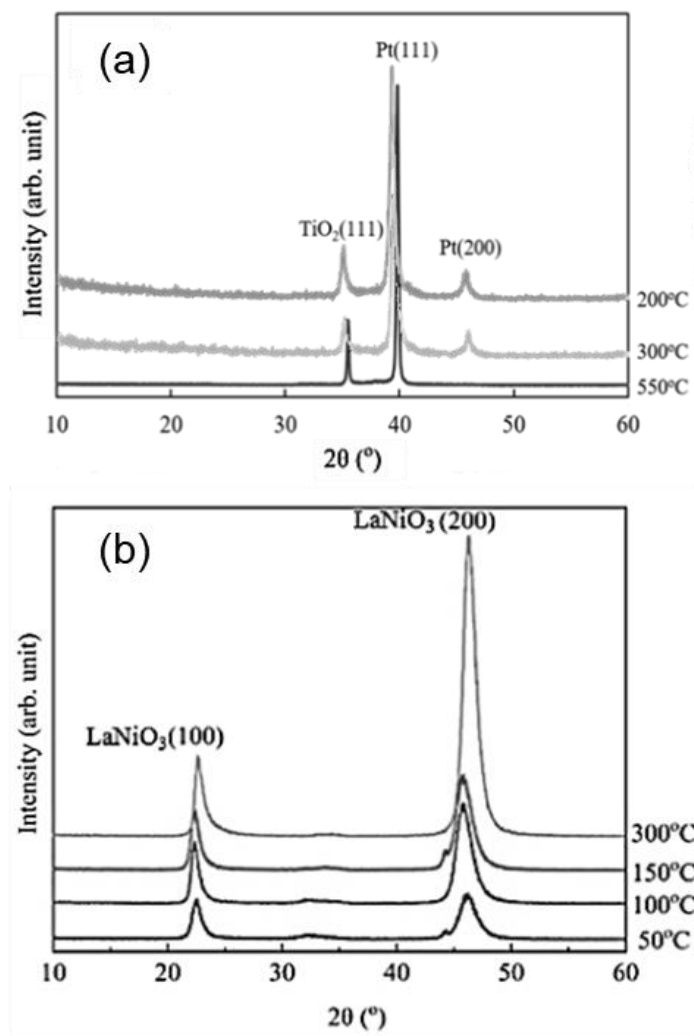


Fig. 3.7 XRD patterns of (a) Pt/TiO₂/SiO₂/Si and (b) LaNiO₃/SiO₂/Si substrates.

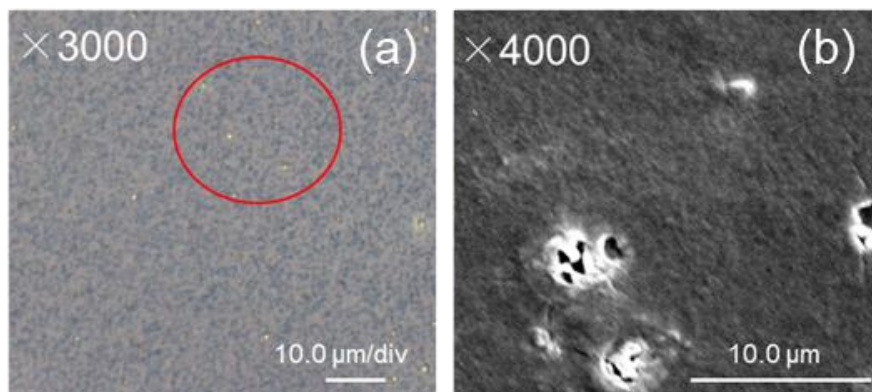


Fig. 3.8 Surface images of Pt/TiO₂/SiO₂/Si by electron optical microscope (a) and films on Pt/TiO₂/SiO₂/Si by SEM (b).

Table 3.5 Sputtering conditions of bottom electrode layers.

| Target | Ti | Pt | LaNiO ₃ |
|---------------------|---------------------------|--|---------------------------|
| Substrate | SiO ₂ /Si | TiO ₂ /SiO ₂ /Si | SiO ₂ /Si |
| Temperature (°C) | 200/300/550 | 200/300/550 | 50/150/150/300 |
| Gas pressure (Torr) | 2-9×10 ⁻³ | 2-9×10 ⁻³ | 2-9×10 ⁻³ |
| Gas flow (sccm) | Ar:18; O ₂ :12 | Ar:18 | Ar:18; O ₂ :12 |
| Power (W) | 150 | 150 | 150 |
| Time (min) | 3 | 5 | 60 |

3.2.4 Exploration of the spin-coating condition

The spin speed and spin coating times affect the film thickness directly. In this study, a two-step spin-coating method was used with the conditions in Table 3.6. By comparing specimens No. 2 and No. 3, increasing the time of step I had little effect on the film quality. Flaws in specimens No. 1 - 4 appeared after pyrolysis at 400 °C. This was due to the effective film-formation components being relatively limited due to the existence of massive organic components. This is also the reason the high inner-stress producing during the pyrolyzation. For the specimen No. 5, the thickness was enough to sustain the inner stress, so no flaws appeared and approximate 700 nm in thickness of thin film were obtained in the following process.

Table 3.6 Spin-coating conditions.

| No. | Step I | | Step II | | Times | State after pyrolysis |
|-----|----------|-------------|----------|-------------|-------|-----------------------|
| | Time (s) | Speed (rpm) | Time (s) | Speed (rpm) | | |
| 1 | 5 | 500 | 30 | 3500 | 5 | Flaw |
| 2 | 5 | 500 | 30 | 3000 | 3 | Flaw |
| 3 | 10 | 500 | 30 | 3000 | 3 | Flaw |
| 4 | 5 | 500 | 30 | 2000 | 3 | Flaw |
| 5 | 5 | 500 | 30 | 1700 | 3 | No-flaw |

3.2.5 Thermal treatment process

In this study, the thermal treatment process included the evaporation of inorganic components, the pyrolyzation of organic components, and the crystallization of thin film. The evaporation of inorganic components was proceeded in the step II of spin-coating at 120 °C. Additionally, the pyrolyzation condition of organic components was determined as 400 °C for 30 min and the heating rate was 1 °C/min. For the crystallization process, two main factors were considered: temperature and heating rate. The effect of temperature on the phase transition will be discussed in Chapter 3.3. Heating rate mainly affects the film-formation quality. A Rapid thermal annealing (RTA) system and a muffle furnace were used for thin film crystallization. RTA is a heating system which can heat specimens over 1000 °C in a matter of seconds. The specimens crystallized by RTA displayed rough and powdery surfaces. This indicated that a rapid rise in temperature was not conducive to film-formation quality of massive organic components. Ultimately, a muffle furnace was used to create a crystallization process with a slow heating rate, as shown in Fig. 3.9. Thus, the quality of film-formation was improved.

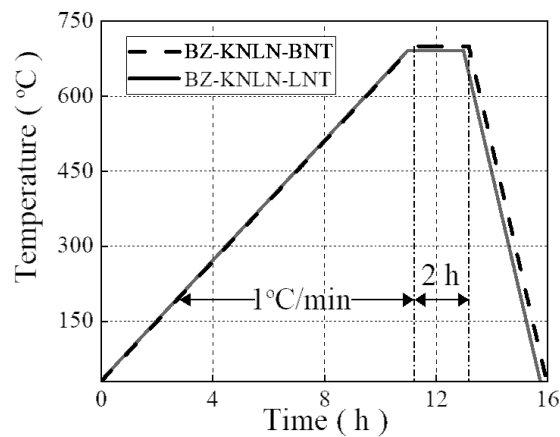


Fig. 3.9 Curve of heating rate in the crystallization process.

3.3 Results and Discussion

3.3.1 BZ-KNLN-BNT

The precursor solution of $0.055\text{BaZrO}_3\text{-}0.935(\text{K}_{0.45}\text{Na}_{0.5}\text{Li}_{0.05})\text{NbO}_3\text{-}0.01(\text{Bi}_{0.5}\text{Na}_{0.5})\text{TiO}_3$ was synthesized. The TG/DTA curve is shown in Fig. 3.10. The DTA curve displayed an endothermic peak before 200 °C and an exothermic peak appeared at 550 °C. The endothermic peak refers to the evaporation process of inorganic and organic compositions and the polycondensation between EG and metal-CA. The exothermic peak shows the synthesis reaction. From the TG curve, the weight loss was drastic before 200 °C and steady above 650 °C. This means the final synthesis reaction is achieved at 650 °C. According to the experience in TG/DTA data, the actual heat treatment temperature could be confirmed to about 700 °C.

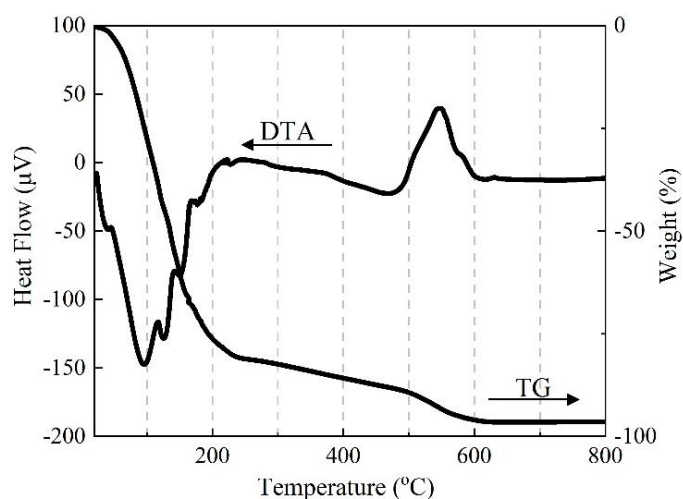


Fig. 3.10 TG/DTA spectrum of BZ-KNLN-BNT precursor.

To confirm the heat treatment temperature, the precursor solutions were heated at 650 °C and 700 °C for 2 h, respectively. The XRD patterns of the powders are shown in Fig. 3.11. Pyrochlore structure peaks appeared at 20° and 28° at 650 °C due to the

incomplete reaction at this low temperature. However, in the case of 700 °C, the powder from the precursor solution showed a perovskite structure. Consequently, the heat treatment temperature was determined to be 700 °C. This corresponds to the results from the TG/DTA curves.

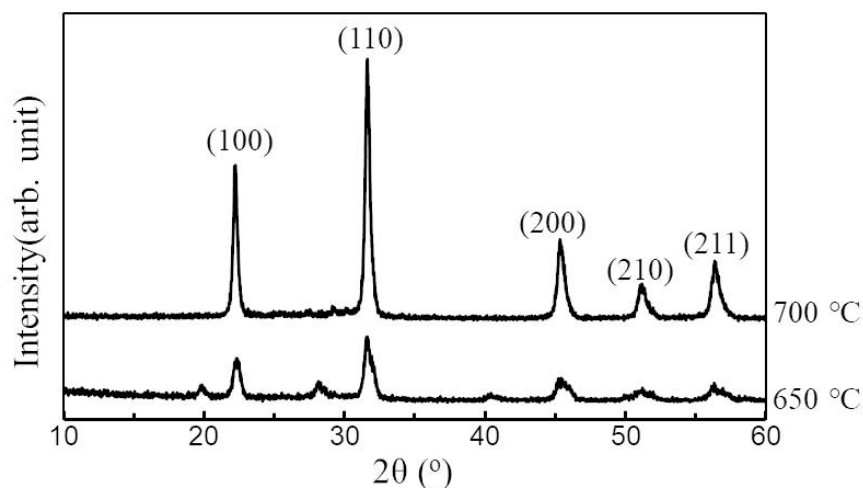


Fig. 3.11 XRD patterns of powder from heating the precursor solutions.

The qualitative EDXA of the powder was measured with the SEM system. Li cannot be detected in this EDXA due to its low energy of characteristic radiation. Other element peaks appeared in Fig. 3.12. Although the accuracy of the quantitative EDXA is affected by the multi-component compositions, the count peaks indicated the existence of the elements of the composition. According to the reliability qualitative EDXA, it is confirmed that the modified Pechini method is effective in regard to the preparation of the stable multicomponent precursor solution.

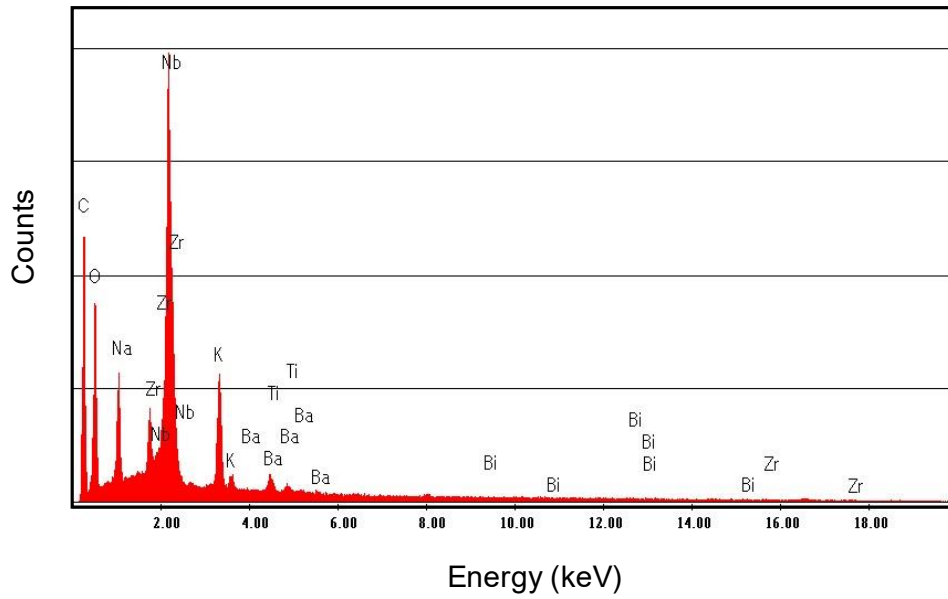


Fig. 3.12 EDXA spectrum of BZ-KNLN-BNT powder.

Next, the films were grown on LNO/SiO₂/Si substrates with the prepared precursor solution. The films were heated at 700 °C for 2 h. Fig. 3.13 shows the XRD patterns of thin films and substrates. The (100) and (200) peaks of the thin films were observed at $2\theta = 22.88^\circ$ and 45.46° , and the (100) and (200) peaks of LNO were observed at $2\theta = 23.22^\circ$ and 47.36° , respectively. Comparing with the XRD pattern of powder in Fig 3.11, the strongest (110) peak of the thin film did not appear but a strong (100) peak appeared on the (100) oriented LNO/SiO₂/Si substrate. This indicated that the BZ-KNLN-BNT films on LNO/SiO₂/Si substrates showed a preferential (100) orientation on the (100) oriented LNO/SiO₂/Si.

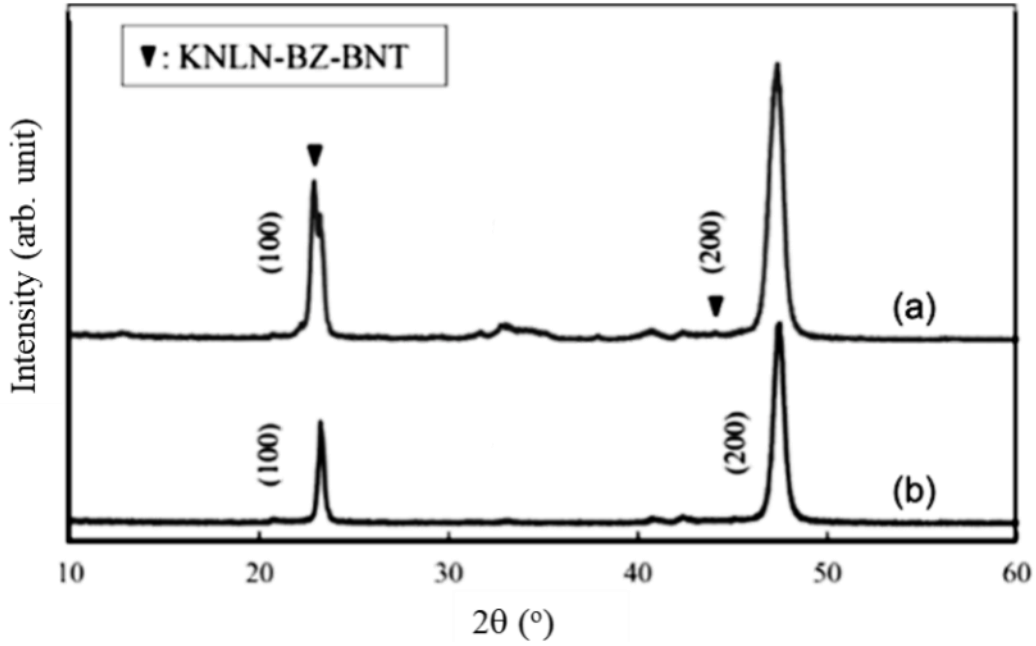


Fig. 3.13 XRD patterns of (a) KNLN-BZ-BNT films on LNO/SiO₂/Si substrate crystallized at 700 °C and (b) LNO/SiO₂/Si substrate.

Surface and cross-sectional SEM images of the thin films are shown in Fig. 3.14. Fig. 3.14 (a, b) shows that the surface of thin film grown on Pt/TiO₂/SiO₂/Si substrate was rough. Thus, the substrate LNO/SiO₂/Si was used to replace the Pt/TiO₂/SiO₂/Si substrate. The picture shows that the grain size of the thin films grown on LNO/SiO₂/Si was about 200 nm and the thicknesses of the thin film and LNO layer were about 700 nm and 280 nm, respectively, as shown in Fig. 3.14 (c, d).

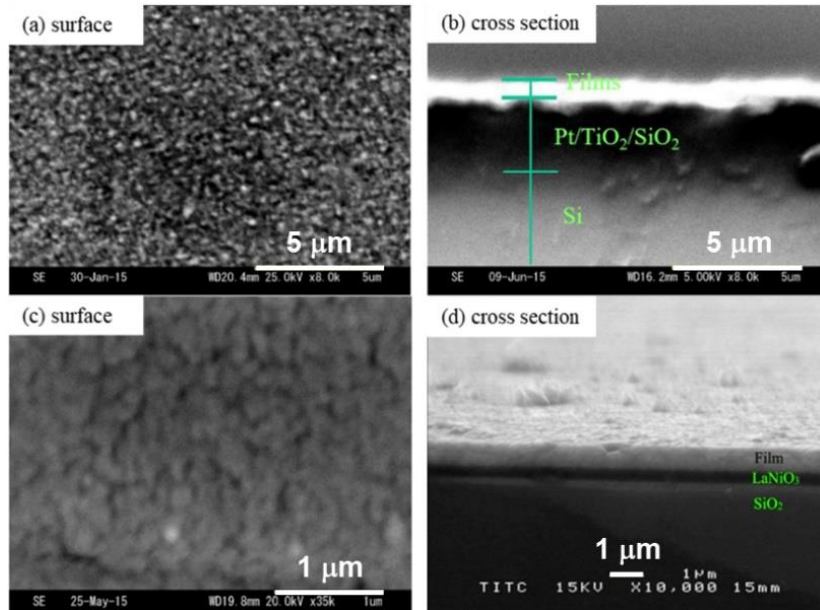


Fig. 3.14 SEM images of thin films on LNO/SiO₂/Si: (a, b) and Pt/TiO₂/SiO₂/Si: (c, d).

The temperature dependence of the dielectric constant at 100 kHz is shown in Fig. 3.15. The figure shows that the T_C of the films was 292 °C, and this value was near to that of the bulk ceramics (270 °C) in previous research. The values for the dielectric constant were lower than that of the bulk ceramics ($\epsilon_r = 1600$ at RT) due to the restraint from the rigid substrates. The dielectric loss, however, was unable to be measured. This may be the result of the defects and inadequate thickness of the films.

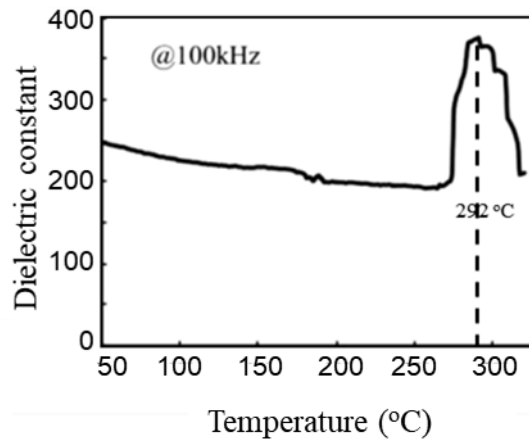


Fig. 3.15 Temperature dependence of dielectric constant of KNLN-BZ-BNT films.

3.3.2 BZ-KNLN-LNT

In this part of the experiment, the components of the precursor solution were prepared based on the chemical formula of $(1-x-y)\text{BaZrO}_3-x(\text{K}_{0.45}\text{Na}_{0.5}\text{Li}_{0.05})\text{NbO}_3-y(\text{La}_{0.5}\text{Na}_{0.5})\text{TiO}_3$ (BZ-KNLN-LNT) ($y = 0.0075$). In this composition, La was used to instead of Bi, due to the evaporation of Bi_2O_3 in BZ-KNLN-BNT at high temperature. This composition of bulk ceramics proved of the existence of the vertical MPB at $x = 0.9025$. To investigate the existence of the vertical MPB using the Pechini method, the precursor solutions with the compositions at $x = 0.9$, 0.9025 , and 0.905 were synthesized.

The chemical reaction process was also characterized by TG/DTA, as shown in Fig. 3.16. The drastic polycondensation between EG and metal-CA occurred before 220°C . With the temperature increasing, the gel process finished at 650°C , allowing the synthesis reaction to be achieved above 650°C . Due to little discrepancy in the compositions, only the TG/DTA of $x = 0.9025$ was measured as a representative.

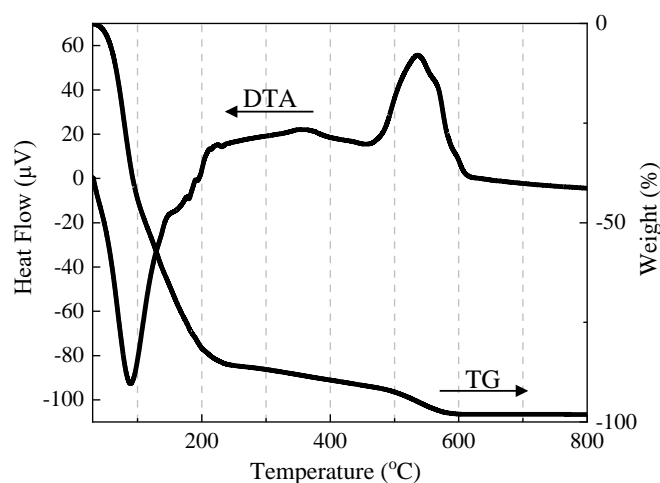


Fig. 3.16 TG/DTA spectrum of the precursor solution $(1-x-y)\text{BZ}-x\text{KNL}-y\text{LNT}$ ($x = 0.9025$, $y = 0.0075$).

The precursor solutions were heated at 700 °C for 2 h. Fig. 3.17 shows the XRD patterns of the powders. The (100), (110), and (200) peaks were at $2\theta = 22.16^\circ$, 31.56° , and 45.36° , respectively. All obtained powders showed the perovskite structures as the same as ceramics by solid-phase synthesis⁷⁾. The high-temperature XRD patterns of the powders in the range of room temperature to 300 °C are shown in Fig. 3.18. With the temperature rising, in the case of $x = 0.905$, the shape of the characteristic peaks showed a mixed twin peak with a stronger right peak at low temperature and then changed to a single peak above 200 °C. This meant that the phase transition of $x = 0.905$ was from tetragonal to cubic. In the case of $x = 0.9$, the characteristic peaks showed single peaks with temperature increasing. Because the composition of $x=0.9$ was very similar to $x = 0.905$, the phase structures of $x = 0.9$ could be surmised to be rhombohedral at 50 °C and cubic at 300 °C. In the case of $x = 0.9025$, the characteristic peaks showed mixed peaks at low temperature, and the characteristic peaks changed to single peaks above 200 °C. This indicated that the phase transition of $x = 0.9025$ was mixed rhombohedral-tetragonal to cubic. The change of the characteristic peaks of $x = 0.905$ and $x = 0.9025$ above 200 °C illustrated that the T_C 's could be about 200 °C. Consequently, by comparing the phase transition of these three specimens, it could be confirmed that the precursor solution with $x = 0.9025$ prepared by the Pechini process was at the vertical MPB composition. These corroborated with results of $(1-x-y)\text{BZ}-x\text{KNL}-y\text{LNT}$ ceramics in previous studies.

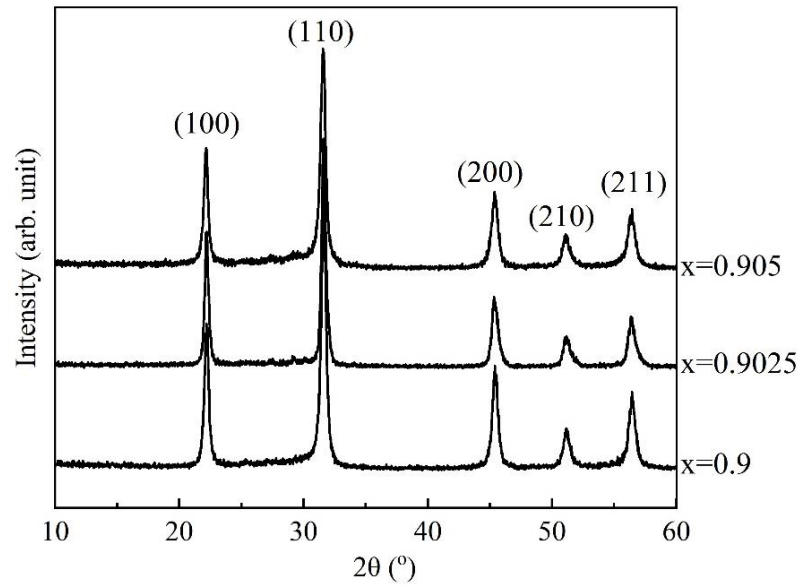


Fig. 3.17 XRD patterns of $(1-x-y)\text{BZ}-x\text{KNLN}-y\text{LNT}$ ($x = 0.9, 0.9025, 0.905, y = 0.0075$) powders from heating the precursor solutions.

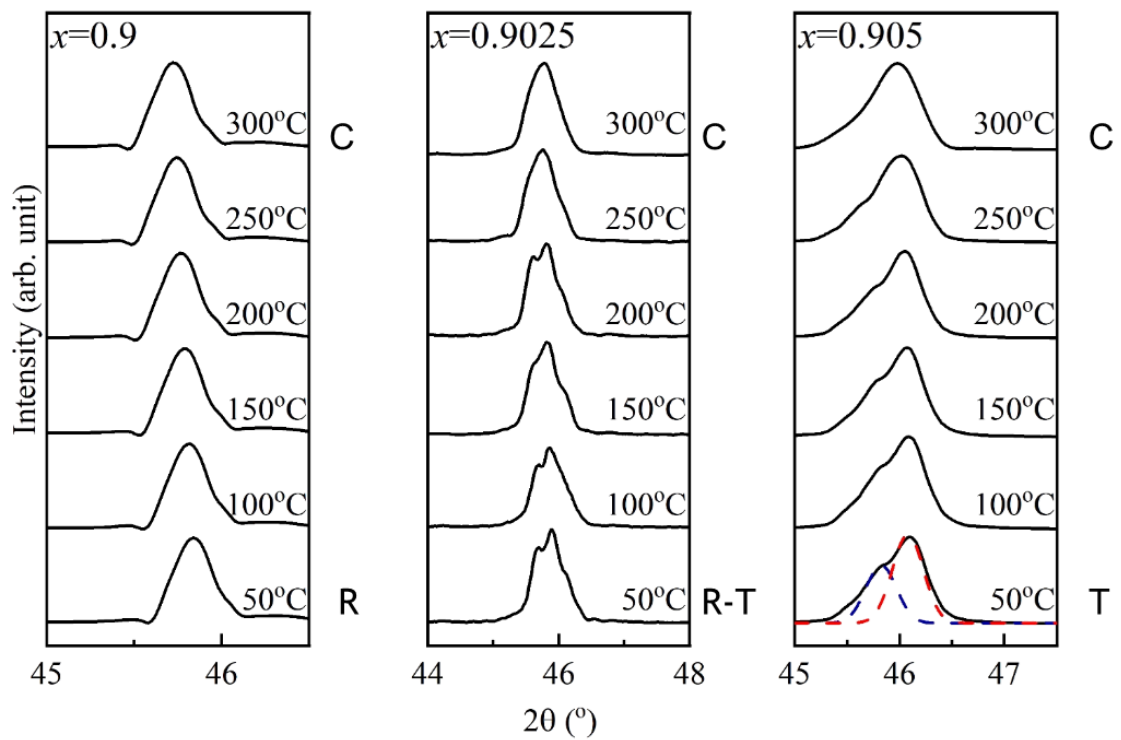


Fig. 3.18 High-temperature XRD patterns of $(1-x-y)\text{BZ}-x\text{KNLN}-y\text{LNT}$ ($x = 0.9, 0.9025, 0.905, y = 0.0075$) powders (R, rhombohedral phase; T, tetragonal phase; R-T: mixed rhombohedral-tetragonal phase; C, cubic phase).

The bulk ceramics were prepared with the obtained powder from the heated precursor solutions. The temperature dependence of the dielectric constant and $\tan\delta$ curves of bulk ceramics were shown in Fig.3.19. From the dielectric constant curve, the T_C 's of $x = 0.9025$ and $x = 0.905$ were about 202 °C and 205 °C, respectively. This result was similar to that of the previous studies. Based on the T_C 's and the high-temperature XRD patterns (Fig. 3.18), the phase diagram of $(1-x-y)\text{BZ}-x\text{KNLN}-y\text{LNT}$ ($x = 0.9025, 0.905, y = 0.0075$) could be obtained, as shown in Fig. 3.20. The composition of $x = 0.9025$ was at vertical MPB. With the temperature increasing, $x > 0.9025$ showed the tetragonal transition, and $x < 0.9025$ should be the rhombohedral-cubic phase transition, respectively.

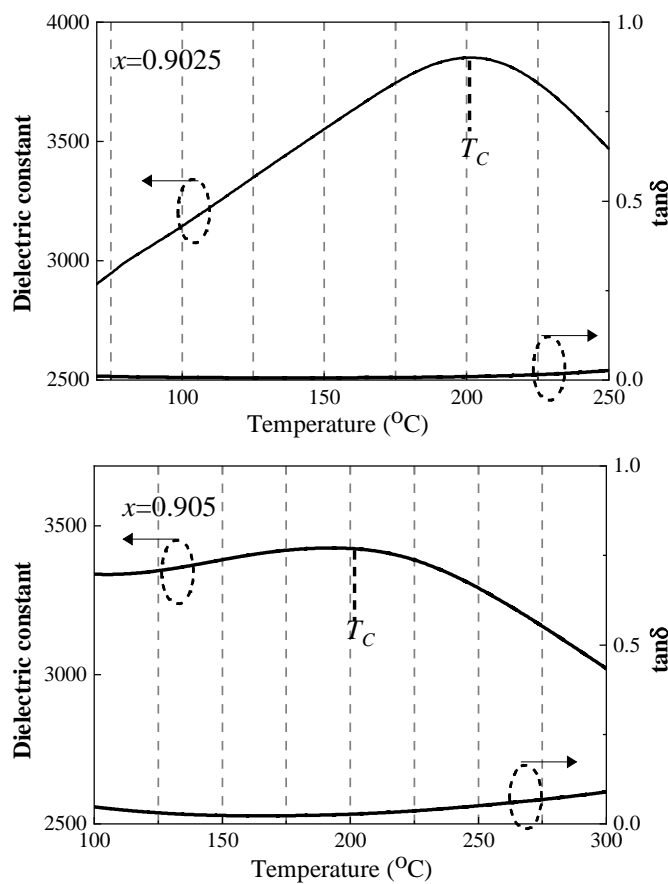


Fig. 3.19 Temperature dependence of the dielectric constant and $\tan\delta$ of $(1-x-y)\text{BZ}-x\text{KNLN}-y\text{LNT}$ ($x = 0.9025, 0.905, y = 0.0075$) bulk ceramics at 100 kHz.

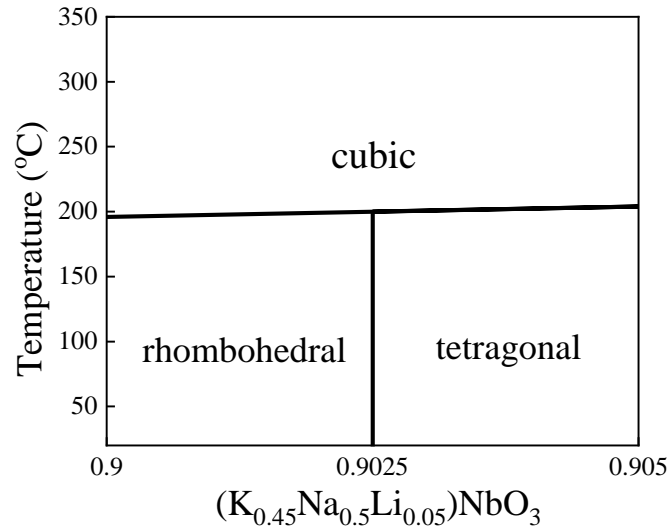


Fig. 3.20 Phase diagram of $(1-x-y)BZ-xKNLN-yLNT$ ($x = 0.9, 0.9025, 0.905, y = 0.0075$) powders from the precursor solution.

Next, the thin films were grown on (100)-oriented, Nb-doped $SrTiO_3$ (STO) substrates using the spin-coating technique. The precursor solutions after heat-treatment at 120 °C for 2 h were grown on (100)-oriented Nb-doped STO substrates using the spin-coating technique. The surface SEM (Fig. 3.21) shows that tight thin films were obtained on STO substrates.

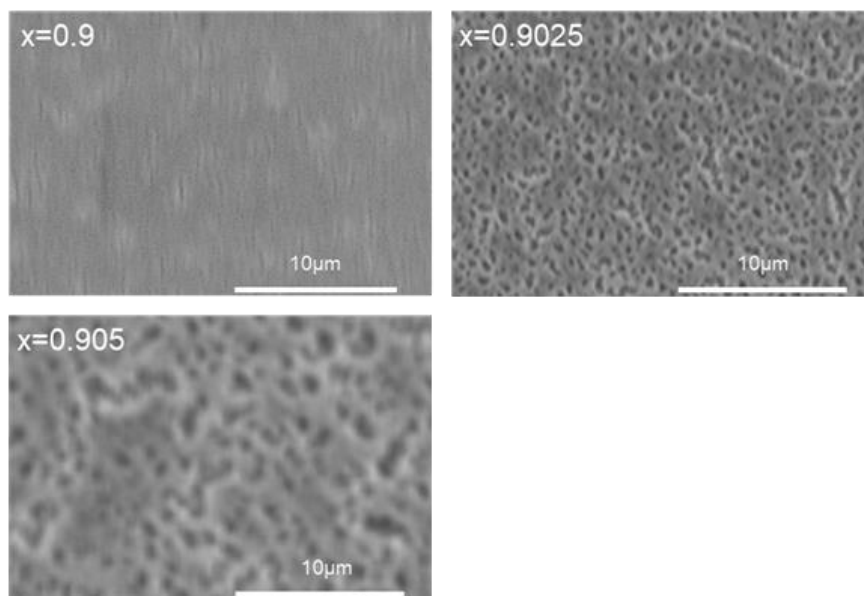


Fig. 3.21 SEM of $(1-x-y)BZ-xKNL-yLNT/STO$ ($x = 0.9, 0.9025, 0.905, y = 0.0075$).

The XRD patterns of BZ-KNLN-LNT/STO are shown in Fig. 3.22. The (100) and (200) peaks of the thin films were at $2\theta = 22.16^\circ$ and 45.42° , whereas the (110) peaks of all thin films at $2\theta = 31.56^\circ$ did not appear. This indicated that all specimens show the (100) oriented epitaxial growth. The specimen of $x = 0.9025$ shows a superior (100) orientation on the STO substrates, as the (100) peak was higher than that of the STO.

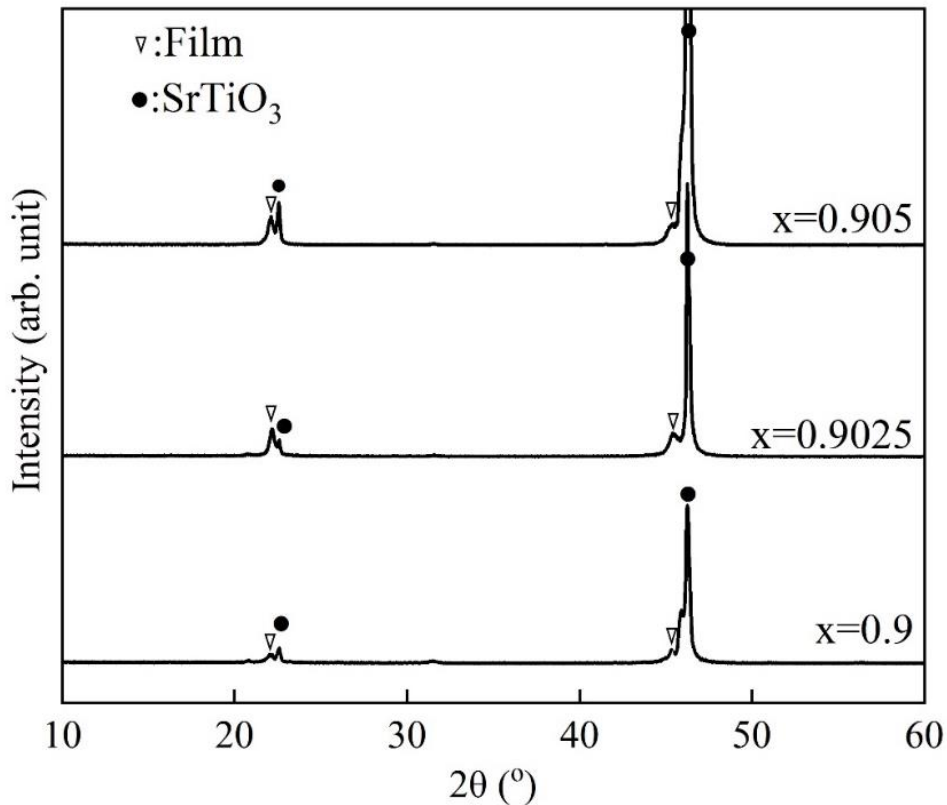


Fig. 3.22 XRD patterns of $(1-x-y)\text{BZ}-x\text{KNLN}-y\text{LNT}$ ($x = 0.9, 0.9025, 0.905, y = 0.0075$) films grown on (100)-oriented SrTiO_3 substrates (690°C).

The frequency-dependent dielectric properties of films were measured using an impedance/ gain-phase analyzer (4194 A), as shown in Fig. 3.23. In the frequency range of $10\text{ k} < 100\text{ k}$, the dielectric constants of $x = 0.9, 0.9025,$ and 0.905 were 760-1100, 950-1360, 580-680, respectively. Although $x = 0.9$ showed unstable dielectric constants with frequency changing, $x = 0.9025$ showed higher dielectric constants than $x = 0.9$ and 0.905 . The dielectric losses of $x = 0.9$ and 0.9025 appeared the values exceed 0.1, and $x = 0.905$ showed dielectric loss values less than 0.1. However, in the frequency

range of $100\text{k} < 1\text{M}$, all film specimens showed stable dielectric properties with changing frequency. The dielectric losses of $x = 0.9$ and 0.905 were in the value range of less than 0.05 with frequency changing and the specimen of $x = 0.9025$ showed large dielectric losses of more than 0.1 at a low-frequency ranges. However, with the increasing of frequency, the specimens of $x = 0.9$, 0.9025 , and 0.905 exhibited the dielectric constants of 800 - 850 , 600 - 650 , and 950 - 1000 , respectively. The specimen of $x = 0.9025$ showed higher dielectric constant values than $x = 0.9$ and 0.905 . The result confirmed that the dielectric constants at the almost vertical MPB composition displayed the maximum values, as mentioned in the introduction.

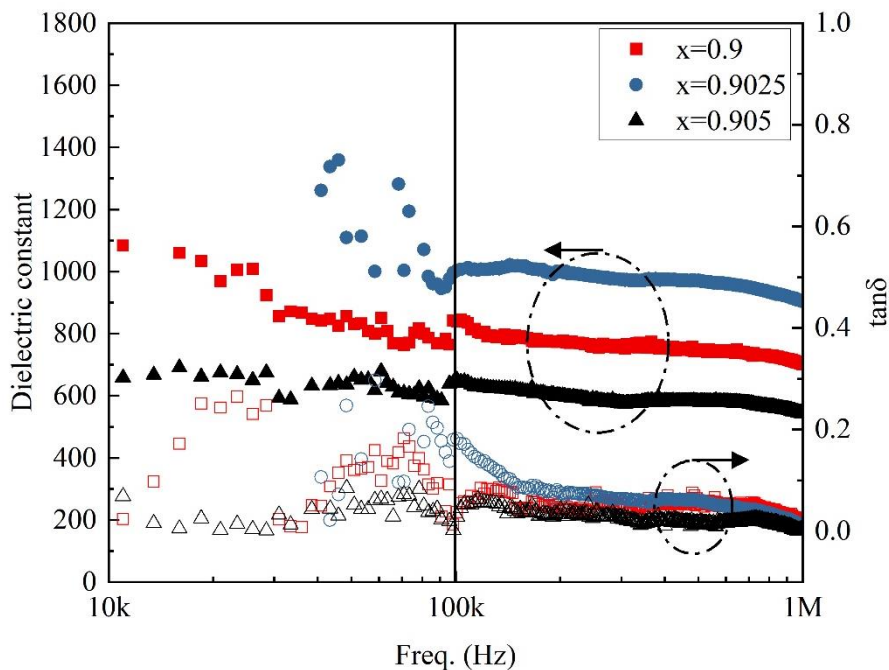


Fig. 3.23 Frequency-dependent dielectric properties of $(1-x-y)\text{BZ}-x\text{KNL}-y\text{LNT}/\text{STO}$ ($x = 0.9, 0.9025, 0.905, y = 0.0075$).

The ferroelectric properties of films were characterized by P - E hysteresis loops, as shown in Fig. 3.24. The E_c values of specimens ($x = 0.9, 0.9025, 0.905$) were about 2 kV/cm , 2 kV/cm , and 3 kV/cm , respectively, and the P_r values were $0.67\ \mu\text{C/cm}^2$, $1.94\ \mu\text{C/cm}^2$, and $0.52\ \mu\text{C/cm}^2$, respectively. The lower ferroelectric properties may be

attributed to restraint from the hard substrate. Among the three specimens, the specimen at $x = 0.9025$ still showed higher P_r than that of others. This meant that the specimen at $x = 0.9025$ showed a harder domain switch than other specimens. The superior ferroelectric properties of the specimen at $x = 0.9025$ also demonstrated that the composition of thin films was in vertical MPB.

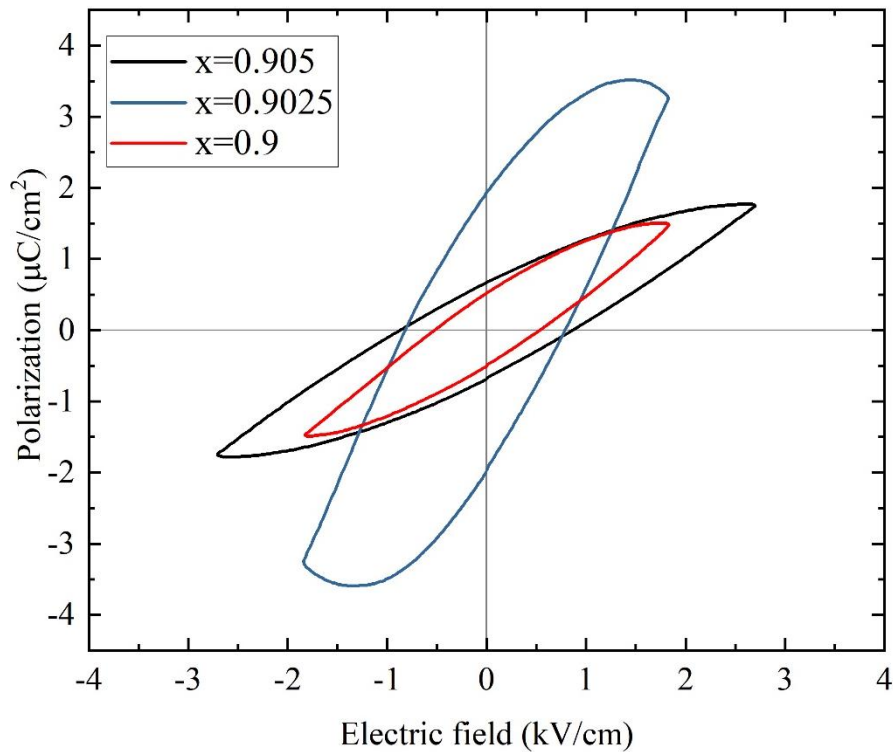


Fig. 3.24 P - E loops of unpoled $(1-x-y)\text{BZ}-x\text{KNLN}-y\text{LNT}$ ($x = 0.9, 0.9025, 0.905, y = 0.0075$) thin films on $(100)\text{-SrTiO}_3$ at 100Hz.

3.4 Summary

A modified deposition method for complex multi-component lead-free thin films was proposed for the first time. The transparent and stable source solutions of Nb, Ti, and Zr were prepared successfully. BZ-KNLN-BNT/LNT thin films were prepared successfully by this method as well. The BZ-KNLN-BNT thin films heated at 700 °C exhibited a perovskite of (100) orientation on (001)-LNO/SiO₂/Si substrates and a T_C

of 292 °C. To BZ-KNLN-LNT, the powders with $x = 0.9, 0.9025$ and 0.905 were obtained by heating the precursor solution and the ceramics were prepared. The T_C 's of the ceramics with $x = 0.9025$ and 0.905 were 202 °C and 205 °C, respectively. By investigating the high temperature XRD patterns and the temperature dependence of the dielectric constant, the vertical MPB composition with $x = 0.9025$ of BZ-KNLN-LNT precursor solution synthesized by Pechini process was verified. BZ-KNLN-LNT thin films were grown on (100)-oriented Nb-doped SrTiO₃ substrates and showed superior (100) orientation along with the substrates. Precise control of multicomponent composition was achieved through the use of the improved Pechini method. The results indicated that the preparation of thin films would not be limited by multi-component materials and the high performance of lead-free piezoelectric films is possible to be achieved. This work brings lead-free materials one step closer to seeing wide use in industry.

References

- 1) Y. Guo, K. I. Kakimoto, and H. Ohsato, *Mater. Lett.* **59** [2-3](2004)241-244.
- 2) R. Zuo, J. Roedel, R. Chen, and L. Li, *J. Am. Ceram. Soc.* **89** [6](2006)2010-2015.
- 3) J. F. Li, K. Wang, B. P. Zhang, and L. M. Zhang: *J. Am. Ceram. Soc.* **89** [2](2006)706-709.
- 4) M. Matsubara, et al., *J. Am. Ceram. Soc.* **88** [5](2005)1190-1196.
- 5) K. Xu, J. Li, X. Lv, J. Wu, X. Zhang, D. Xiao, and J. Zhu: *Adv. Mater. (Weinheim, Ger.)*. **28** [38](2016)8519-8523.
- 6) T. Karaki, T. Katayama, K. Yoshida, S. Maruyama, and M. Adachi, *J. J. Appl. Phys.* **52** [9S1](2013)09KD11.
- 7) R. Baba, T. Karaki, and T. Fujii, *J. Adv. Dielectr.* **6** [02](2016)1650008.
- 8) K. Tonisch, V. Cimalla, C. Foerster, H. Romanus, O. Ambacher, and D. Dontsov: *Sens. Actuators, A*. **132** [2](2006)658.
- 9) J. E. Mahan, *Physical vapor deposition of thin films*. pp. 336. ISBN 0-471-33001-9. (2000).
- 10) Y. Zhao, H. Wang, C. Wu, Z. F. Shi, F. B. Gao, W. C. Li, G. G. Wu, B. L. Zhang, and G. T. Du, *Vacuum* **103** (2014)14-16.
- 11) C. E. Morosanu, *Thin films by chemical vapour deposition* (Elsevier, 2016).
- 12) Y. Zhang, L. Gomez, F. N. Ishikawa, A. Madaria, K. Ryu, C. Wang, A. Badmaev, and C. Zhou, *J. Phys. Chem. Lett.* **1** [20](2010)3101-3107.
- 13) A. E. Martell and R. J. Motekaitis, *Determination and Uses of Stability Constants, 2nd Edition* (1992).

- 14) H. Yang, Y. Lin, F. Wang, and H. Luo: Mater. Manuf. Processes. **23** [5](2008)489-493.
- 15) J. P. Yasno, L. Tirado-Mejia, R. H. G. A. Kiminami, G. J. Sonia, and C. F. V. Raigoza, Bol. Soc. Esp. Ceram. Vidrio. **52** [5](2013)231-236.
- 16) H. Lee, M. Hong, S. Bae, H. Lee, E. Park, and K. Kim, J. Mater. Chem. **13** [10](2003)2626-2632.
- 17) B. Wang, L. Zhu, L. Liu, and S. H. Zhu, CN Patent, CN103864605A (2014).
- 18) X. J. Meng, J. L. Sun, J. Yu, H. J. Ye, S. L. Guo, and J. H. Chu, Appl. Surf. Sci. **171** [1-2](2001)68-70.

CHAPTER IV

LEAD-FREE PIEZOELECTRIC THICK FILMS AFFECTED BY PRESTRESS FROM SUBSTRATES

4.1 Introduction

Within the last twenty years, the thick film field of piezoelectric materials has been undergoing a revolution. Thick films containing PZT have been widely applied in numerous fields due to their wide range of desirable properties, such as superior piezoelectric coefficients. However, the application has been limited throughout the years due to lead oxide pollution. Consequently, the high properties lead-free piezoelectric materials are urgently explored.

Perovskite-based materials are considered to be a suitable candidate replacement for PZT-based materials such as BaTiO₃-based materials,¹⁻³⁾ (Bi,Na)TiO₃-based materials,⁴⁻⁶⁾ and (K,Na)NbO₃-based materials.⁷⁻¹⁰⁾ Lead-free piezoelectric materials based on (1-x)(Bi_{0.5}Na_{0.5})TiO₃-xBaTiO₃ (BNT-xBT) solid solution, which possess good properties are promising alternatives for PZT.¹¹⁾ However, the T_d 's of the BNT-xBT are low, e.g., the MPB composition ($0.06 \leq x \leq 0.07$) with T_d 's of 110-120 °C. In addition, T_d 's of BNT-xBT with $x > 0.11$ are above 160 °C. In this study, 0.83(Bi_{0.5}Na_{0.5})TiO₃-0.17BaTiO₃ (BNT-17BT) was selected due to its relative higher T_d of 209 °C. With the increase in temperature, BNT-17BT exhibits a phase transition from ferroelectric

(tetragonal) to antiferroelectric (cubic) at T_d . The antiferroelectric phase transforms into a paraelectric one at the maximum temperature value (T_m). Correspondingly, the crystal structure changes from tetragonal at room temperature to pseudo-cubic above T_d . The anisotropic tetragonal structure is easy to produce because of the compressive stress influence. In this study, the compressive prestress arising from the substrates was considered to be used. Based on the different thermal expansion coefficients between BNT-17BT thick film and substrates, the compressive prestress produced during the cooling process could be considered as a favorable condition for the increase of the c -axis preferential tetragonal degree and T_C of BNT-17BT with the temperature increasing, as shown in Fig. 4.1. Thus, the application temperature of BNT-17BT would be assumed to improve.

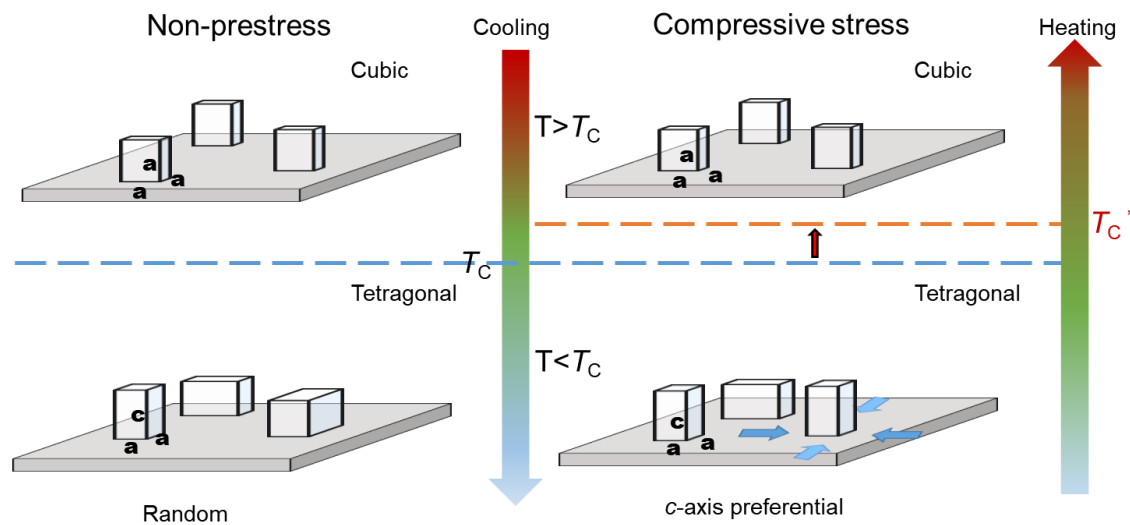


Fig. 4.1 Schematic of phase transition influenced by external stress.

4.2 Experiment

Firstly, raw materials from reagent-grade powders of sodium carbonate (Na_2CO_3) (Furuuchi Chemical, 99.999%), barium carbonate (BaCO_3) (Kojundo Chemical Laboratory, 99.95%), titanium dioxide (TiO_2) (Furuuchi Chemical, 99.99%), and bismuth oxide (Bi_2O_3) (Kojundo Chemical Laboratory, 99.99%) were used to prepare a certain amount power of BNT-17BT by a solid-phase synthesis method. A small amount of CuO powder was added to the ground powder as a sintering aid. Calcination was at 900 °C for 4 h. The calcined bulk was crushed and ground using ball milling for 1 h in absolute ethanol. Secondly, the paste for screen-printing was prepared as follows. An organic vehicle was prepared by mixing ethyl cellulose and α -terpineol at a weight ratio of 1:9. BNT-17BT powder, the organic vehicle, α -terpineol, ethyl acetate, and non-ionic surfactant were mixed with the weight ratio of 9: 1.5: 1.5: 1: 0.2.

Next, the aluminum oxide (Al_2O_3) and magnesium oxide (MgO) substrates with different thermal expansion coefficients were used. Then, screen printing was used to prepare Pt bottom electrodes and fired at a temperature of 1380 °C for 1 h in air. Lastly, the paste of BNT-17BT was printed on the Pt/substrate by using a 325-mesh screen mask, and then the BNT-17BT thick films were sintered at 900 °C for 4 h. After three identical cycles of printing to sintering, the BNT-17BT thick films were prepared successfully and the thickness of the films was approximately 30 μm . Afterwards, a 3×3 mm^2 Au electrode was printed on the thick films and fired at 850 °C for 20 min in air.

4.3 Results and Discussion

The thermal expansion curves of BNT-17BT, MgO, and Al₂O₃ ceramics were measured in the range of RT to 1000 °C, as shown in Fig. 4.2. From Fig. 4.2, MgO bulk ceramics show a higher thermal expansion curve than BNT-17BT and Al₂O₃ ceramics. In the temperature range of RT to 700 °C, the thermal expansion of Al₂O₃ is a bit larger than that of the BNT-17BT. That just means BNT-17BT/MgO could generate compressive stress during the time of refrigeration after sintering, and tensile compressive stress could possibly appear during the refrigeration of BNT-17BT/Al₂O₃ after cooling to room temperature. The two-dimensional X-ray diffraction¹⁴⁾ was used to calculate the residual stress and the values of BNT-17BT/Al₂O₃ and BNT-17BT/MgO were -70 MPa and -320 MPa, respectively, as shown in Table 4.1, where (-) stress values indicate compressive stress. This indicated that the compressive stress can be formed by the difference in thermal expansions between film materials and substrate materials and is consistent with the thick films.

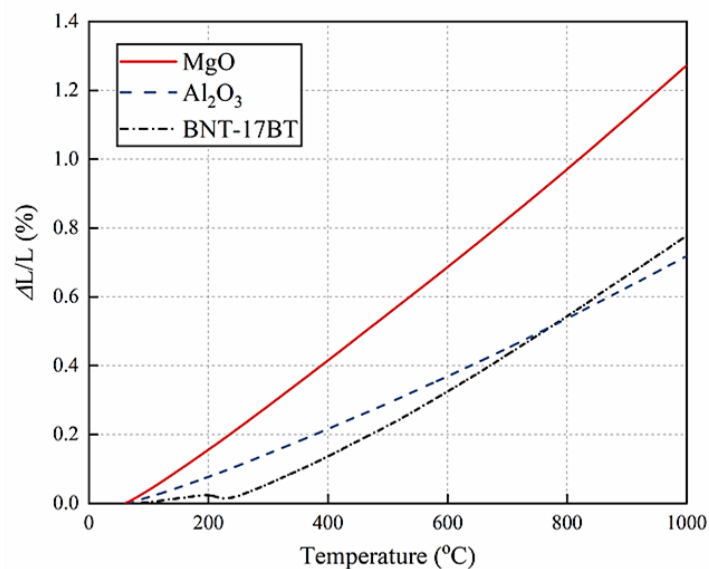


Fig. 4.2 Thermal expansion curves of MgO, Al₂O₃, and BNT-17BT ceramics in the temperature range of RT to 1000 °C.

Table 4-1 The volume fraction of the *c*-domain and residual stress of BNT-17BT bulk ceramics and thick films prepared on Al₂O₃ and MgO.

| Substrate | α_c | Residual stress (MPa) |
|---|------------------------------|------------------------------|
| BNT-17BT | 0.33 | - |
| BNT-17BT/Al ₂ O ₃ | 0.36 | -70 |
| BNT-17BT/MgO | 0.80 | -320 |

The scanning electron microscopy was used to observe the grain sizes of bulk ceramics BNT-17BT/Al₂O₃, and BNT-17BT/MgO. Additionally, the SEM images showed the sizes of the bulk ceramics were approximately 2-4 μm and the ceramic surface is compacted and distributed uniformly, as shown in Fig. 4.3 (a). However, the grain sizes of BNT-17BT/Al₂O₃ and BNT-17BT/MgO were 1-5 μm and 2-5 μm , respectively, as shown in Fig. 4.3 (b)/(c). But unlike the ceramic surface, small holes appeared on the thick films. This was due to the press-formation being used in the ceramic preparation process, whereas it was not used in thick-film preparation process. However, the holes of the BNT-17BT/MgO thick films were smaller in size and much smaller in quantity than those of the BNT-17BT/Al₂O₃ thick films. This result was caused by stress in the thick films due to the sintering process.

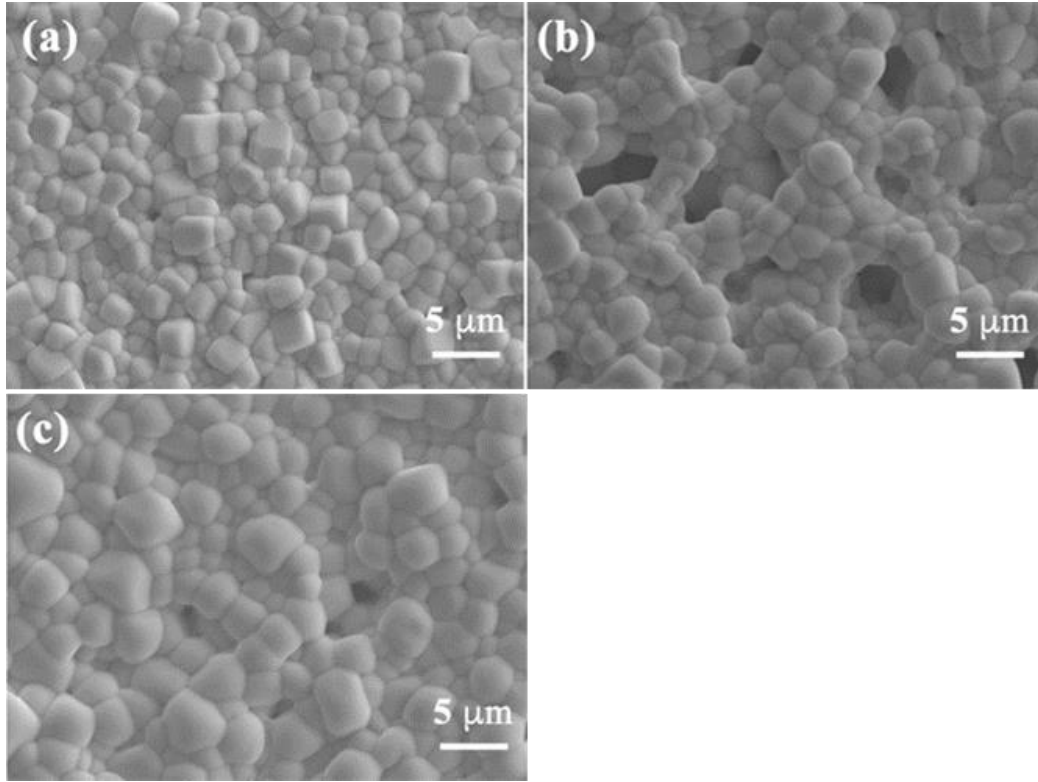


Fig. 4.3 SEM images of (a) bulk ceramics and thick films on (b) Al₂O₃ and (c) MgO.

The XRD patterns of the bulk ceramic powder, BNT-17BT/Al₂O₃, and BNT-17BT/MgO were shown in Fig. 4.4. Additionally, the XRD images appear to show that all specimens had a perovskite single phase. The volume fraction of the *c*-domain (α_c) was calculated with the XRD data as follows:

$$\alpha_c = V(002)/[V(002) + V(200)]$$

where V is peak area from integrating data. The calculated α_c values of BNT-17BT/MgO, BNT-17BT/Al₂O₃, and BNT-17BT bulk correspond to 0.80, 0.36, and 0.33, respectively. The result is shown in Table 4.1, and the relational graph between tetragonal degree and stress effect is shown in Fig. 4.5. Simultaneously, BNT-17BT/MgO and BNT-17BT/Al₂O₃ exhibited preferentially *c*-domains because of the influence of compressive stress, as shown in Fig. 4.1 and Fig 4.5.

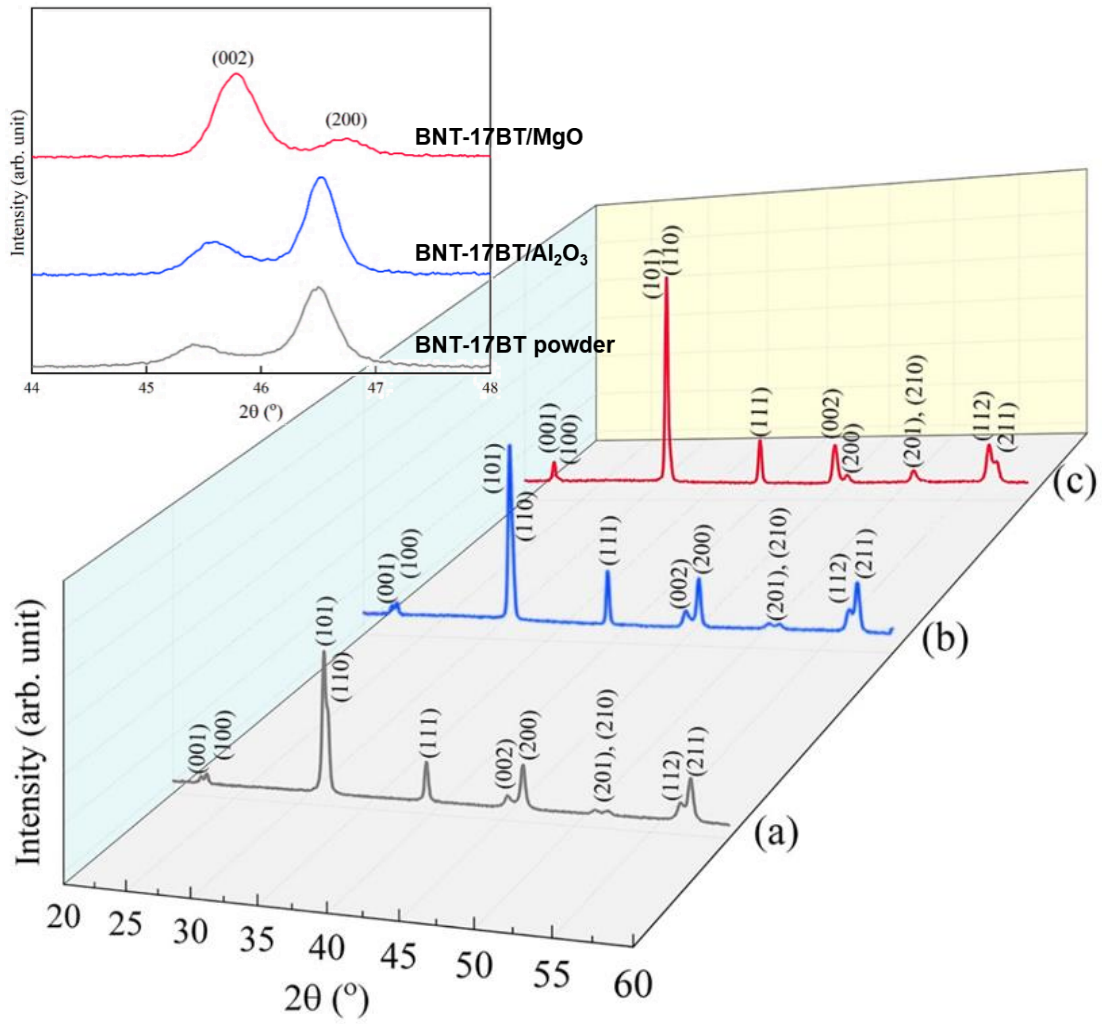


Fig. 4.4 XRD patterns of (a) BNT-17BT powder, (b) BNT-17BT/Al₂O₃, and (c) BNT-17BT/MgO.

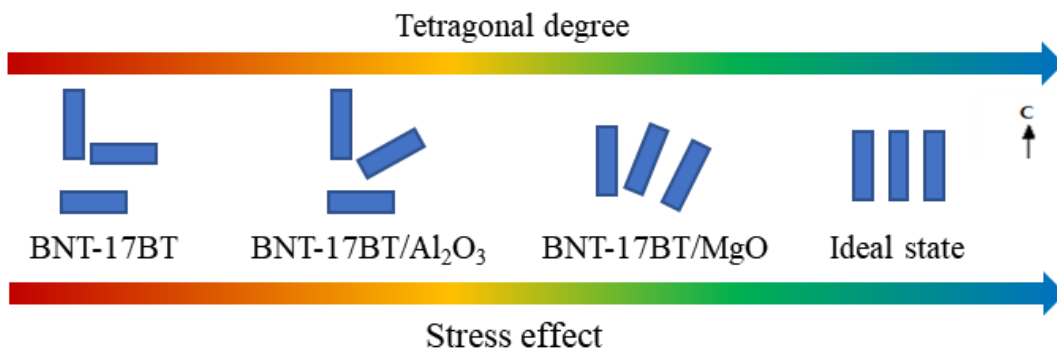


Fig. 4.5 Relational graph between tetragonal degree and stress effect.

The high-temperature XRD patterns ($44.5^\circ < 2\theta < 47.5^\circ$) were used to measure the BNT-17BT powder, BNT-17BT/ Al_2O_3 , and BNT-17BT/MgO, and the set temperature range was from 25 °C to 350 °C (Fig. 4.6). At room temperature, the intensity of the (200) peak at a high 2θ value for the BNT-17BT powder and BNT-17BT/ Al_2O_3 was strong. In contrast, the intensity of the (002) peak at a low 2θ value for BNT-17BT/MgO was strong. When the temperature exceeded 200 °C, the twin peaks of the BNT-17BT powder and BNT-17BT/ Al_2O_3 transformed into the single peaks. For BNT-17BT/MgO, the twin peaks changed to the single peak at temperature above 250 °C. The phase transition temperature can be confirmed when the two peaks changed into one peak. This result indicated that the crystal structure of the BNT-17BT thick films changed from tetragonal to cubic with increasing temperature, and the thick films prepared on MgO substrates exhibited a higher phase transition temperature. Thus, the thick films on MgO exhibited preferential *c*-domains during the phase change from tetragonal to cubic with increased temperature. This also indicated that the more random tetragonal *c*-direction of BNT-17BT was ordered by the compressive stress from MgO.

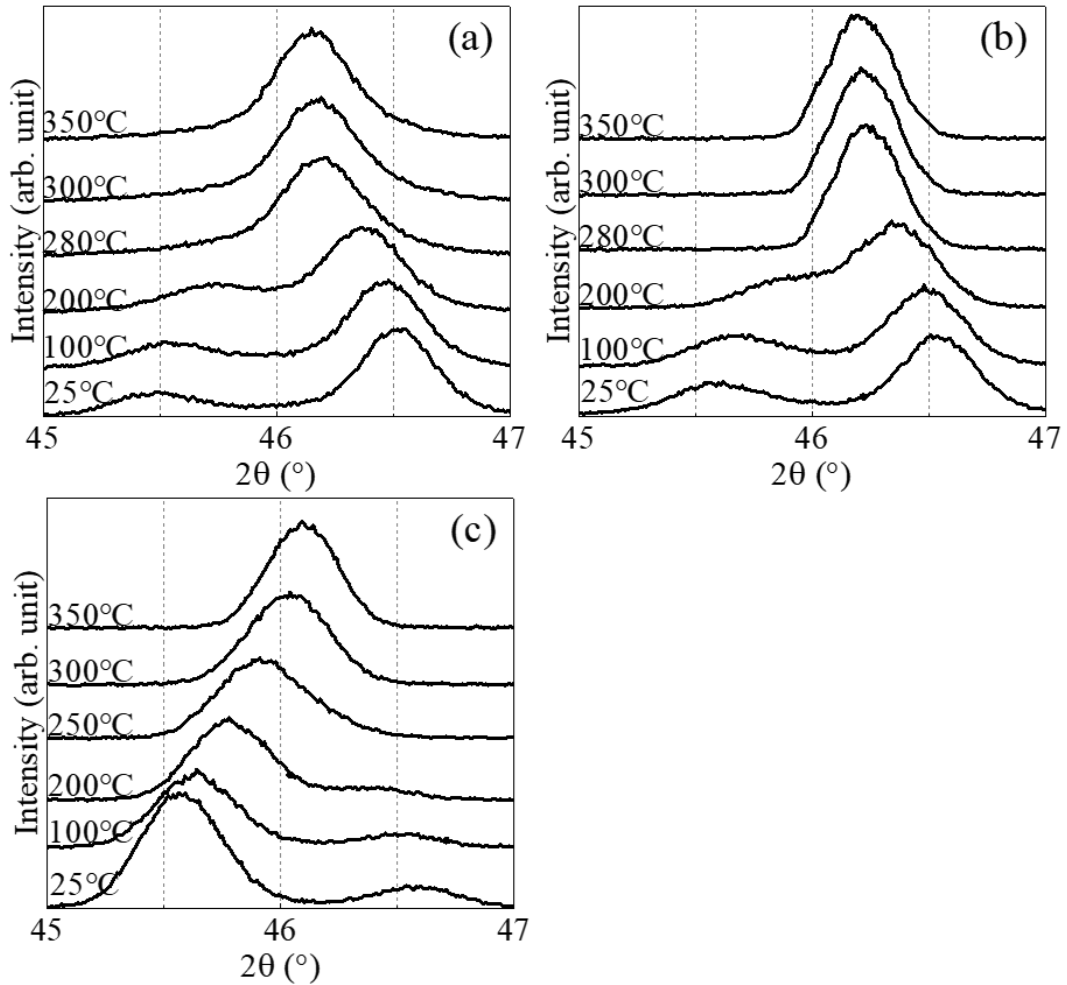


Fig. 4.6 High-temperature XRD intensity of (a) BNT-17BT powder and BNT-17BT thick films on (b) Al_2O_3 and (c) MgO .

Piezoresponse force microscopy (PFM) was used to observe the domain structure of BNT-17BT/ Al_2O_3 , and BNT-17BT/ MgO , as shown in Fig. 4.7. All BNT-17BT thick films exhibited similar polycrystalline morphology in topography images. In phase images, the bright yellow area represented the 180° domain area and the black area represented the 90° domain area. BNT-17BT/ MgO showed clear wave-like domain areas and BNT-17BT/ Al_2O_3 showed relatively ambiguity spindle-like domain areas. The larger distinct 180° domain area in BNT-17BT/ MgO compared to those in BNT-17BT/ Al_2O_3 confirmed that the preferential *c*-axis orientation in thick films can be obtained under the effect of the compressive stress.

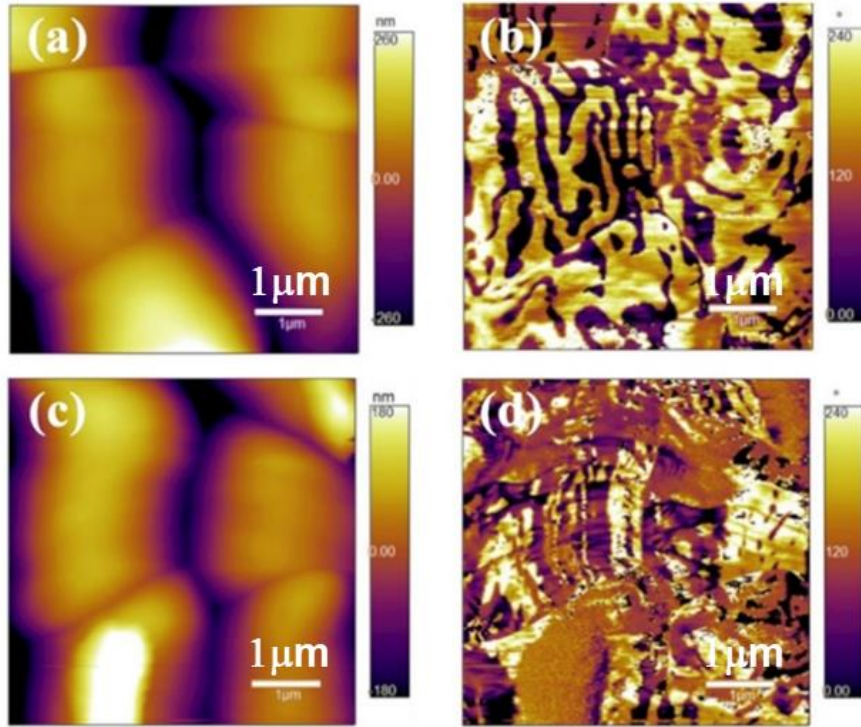
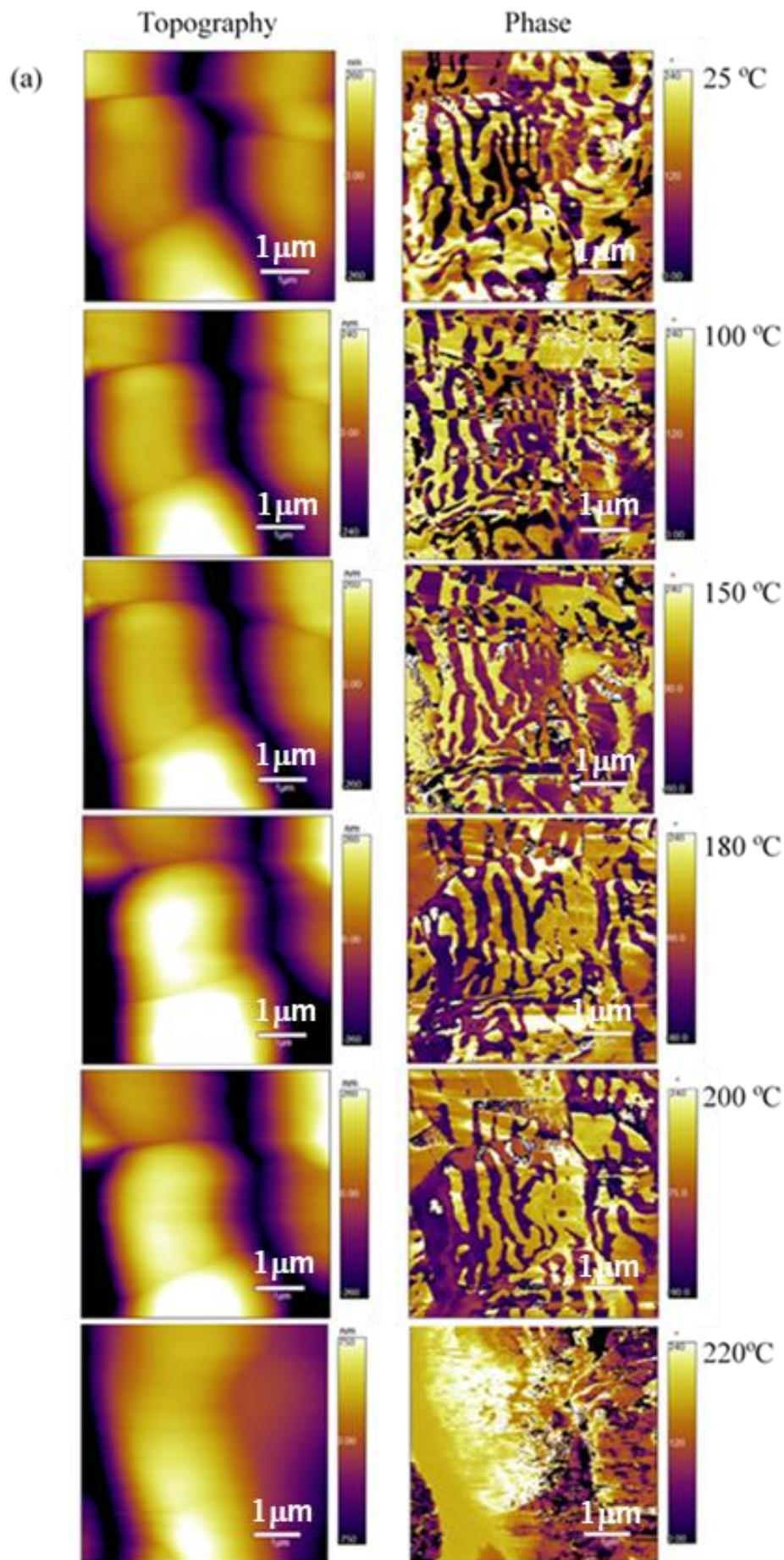


Fig. 4.7 PFM images of un-poled BNT-17BT thick films at 25 °C. (a, c) topography images of (a) BNT-17BT/MgO and (c) BNT-17BT/Al₂O₃, (b, d) phase images of (b) BNT-17BT/MgO and (d) BNT-17BT/Al₂O₃.

The high-temperature PFM images in the temperature range of 25 °C-230 °C are shown in Fig. 4.8. As shown in the topography images, crystalline sizes increased with temperature. As shown in the phase images, for BNT-17BT/MgO, when the temperature was from room temperature to 150 °C, the wave-like 90° domain gradually increased and until 200 °C connected into a large area. For BNT-17BT/Al₂O₃, the spindle-like 90° domain also increased with temperature increasing. This indicated that the domain inversions of BNT-17BT/MgO and BNT-17BT/Al₂O₃ occurred above 220 °C. Thus, the T_d 's of BNT-17BT/MgO and BNT-17BT/Al₂O₃ should exceed 220 °C.



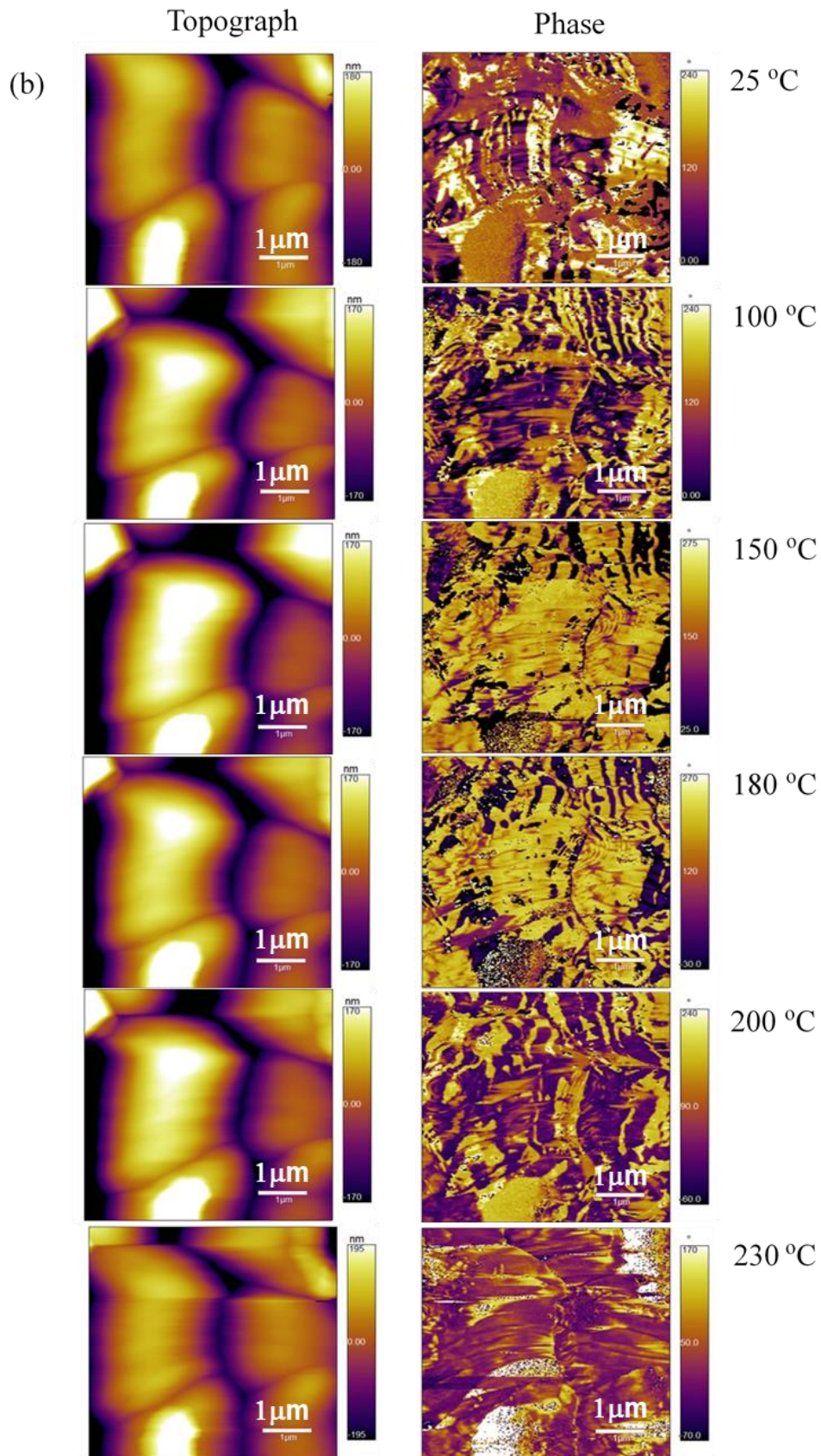


Fig. 4.8 High-temperature PFM images of BNT-17BT thick films on (a) MgO and (b) Al₂O₃.

The temperature dependence of the dielectric constant and $\tan\delta$ of bulk ceramics and BNT-17BT/MgO are shown in Fig. 4.9. The temperature at which the dielectric constant shows a hump indicates T_d .¹³⁾ Combined with the previous experimental data,^{7,11)} in the case of BNT-17BT bulk ceramics, an obvious hump appeared at about 210 °C and a T_m of 266 °C. It showed BNT-17BT bulk ceramics is a relaxor ferroelectric. However, BNT-17BT/MgO showed an ambiguity hump and a T_m of 340 °C. This indicated that BNT-17BT thick film on the MgO had the same temperature dependence of the dielectric constant curve shape as the ordinary ferroelectrics. The T_d of BNT-17BT/MgO should be at the T_m . This result illustrated that the compressive stress produced by the difference of thermal expansion coefficients could result in the T_d improvement of BNT-17BT.

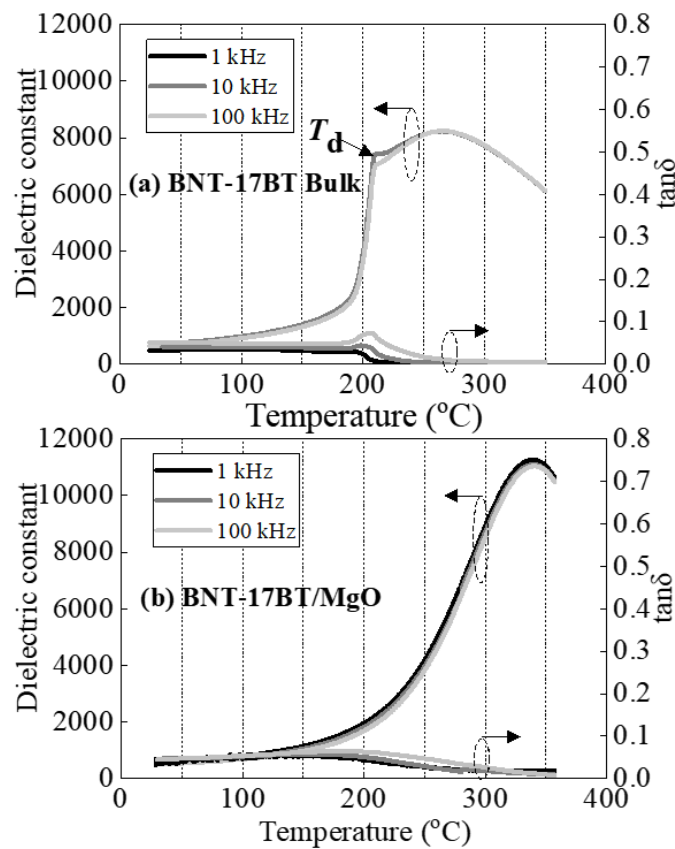


Fig. 4.9 Temperature dependence of the dielectric constant and $\tan\delta$ of (a) bulk ceramics and (b) BNT-17BT/MgO at 1 kHz, 10 kHz, and 100 kHz.

Fig.4.10 shows the temperature dependence of the piezoelectric coefficient d_{33} measured with a heating rate of 5 °C/min. The polarization conditions of bulk ceramics and thick films were 2 kV/mm at 150 °C for 5 min in silicone oil and 100 V at 120 °C for 5 min in air, respectively. The temperatures of the d_{33} maximum values of the bulk ceramics, BNT-17BT/ Al_2O_3 , and BNT-17BT/MgO were 220 °C, 310 °C, and 340 °C, respectively. The depolarization occurred above the peak temperature and this corroborated with the results in Fig 4.9. BNT-17BT/MgO showed a high T_d . This was because tetragonal phase transition occurred easily due to effect of the compressive stress from the MgO substrate in the cooling process. The d_{33} values of BNT-17BT/MgO and BNT-17BT/ Al_2O_3 were smaller than that of the bulk ceramics below the temperature of 220 °C. This was caused by the restraint effect of the rigid ceramic substrates to the thick films. However, the thick films still displayed piezoelectric properties until the temperature approaching 250 °C.

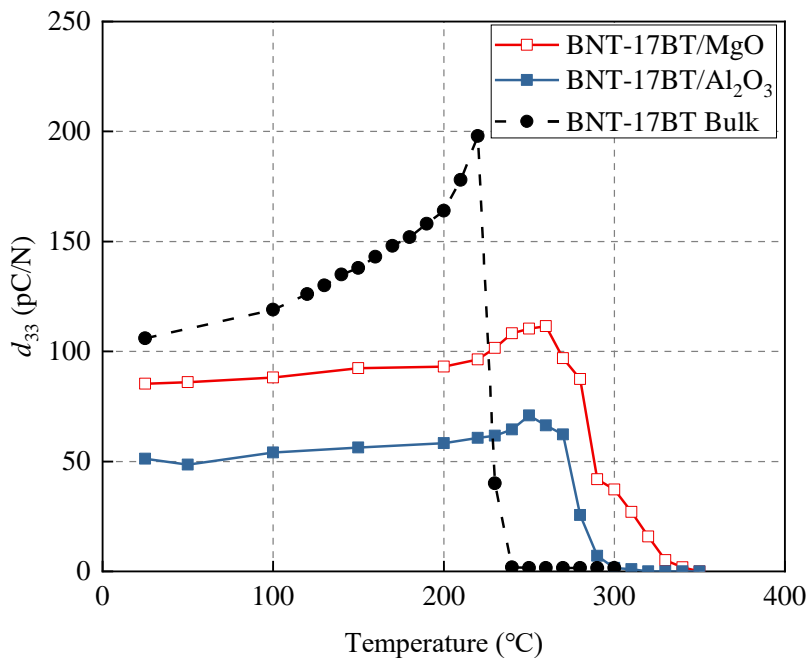


Fig. 4.10 Temperature dependence of the piezoelectric coefficient d_{33} of bulk ceramics and BNT-17BT/ Al_2O_3 , and BNT-17BT/MgO.

The P - E hysteresis curves of the bulk ceramics and the thick films prepared on the Al_2O_3 and MgO at high temperatures are shown in Fig. 4.11. The electric fields applied were 60 kV/cm on the thick films and 40 kV/cm on the bulk ceramics. The insulation breakdown and current leakage occurred in the bulk ceramics over 40 kV/cm. The P_r values of BNT-17BT/ MgO and BNT-17BT/ Al_2O_3 were $10 \mu\text{C}/\text{cm}^2$ and $4 \mu\text{C}/\text{cm}^2$, respectively. The high c -axis orientation of the thick films on the MgO substrate resulted in a high P_r value, exceeding that of the thick films on the Al_2O_3 substrate. The double hysteresis loops of the bulk ceramics indicated the existence of an antiferroelectric phase at 220 °C, whereas in the case of the thick films at 270 °C, an antiferroelectric phase was not observed. This indicated that the T_d of BNT-17BT on substrates was improved.

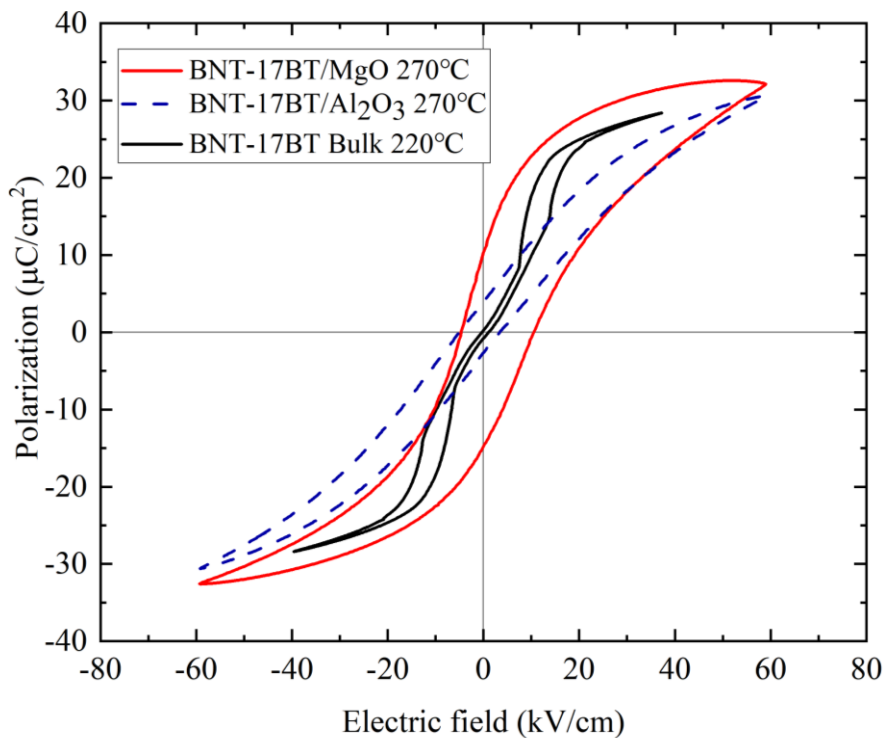


Fig. 4.11 P - E loops of the bulk ceramics at 220 °C and thick films prepared on Al_2O_3 and MgO ceramics at 270 °C.

The temperature dependence of P_r and E_c for the specimens is shown in Fig. 4.12. The P_r values of BNT-17BT/MgO and BNT-17BT/Al₂O₃ increased and then declined at approximately 220 °C and 200 °C, respectively. In the case of BNT-17BT/MgO, the corresponding temperature of maximum P_r value was higher because of its more preferential c -axis orientation than that of BNT-17BT/Al₂O₃. The P_r values of the BNT-17BT thick films were inferior to that of the BNT-17BT bulk ceramics due to the restraint effect of rigid substrates. However, when the temperature exceeded 220 °C, BNT-17BT/MgO still exhibited high piezoelectric properties. By contrast, the P_r value of soft PZT/YSZ was nearly 0, and the P_r value of hard PZT/YSZ could not be measured due to the leakage current. The E_c values of all specimens decreased as the temperature increased.

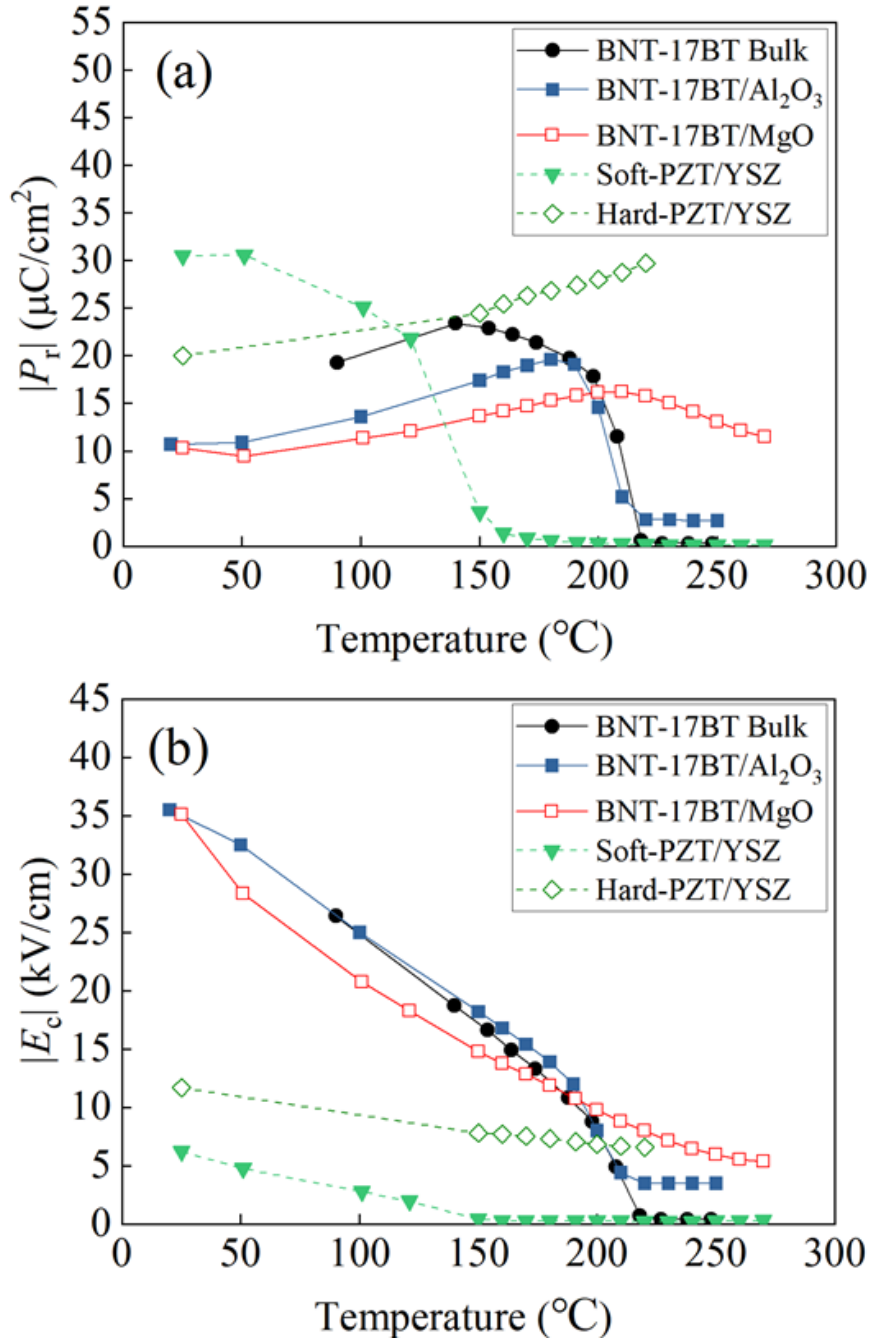


Fig. 4.12 Temperature dependences of (a) P_r and (b) E_c to BNT-17BT bulk ceramics, BNT-17BT thick films, soft PZT/YSZ (3 mol% Y_2O_3 -stabilized ZrO_2), and hard PZT/YSZ.

4.4 Summary

In summary, the T_d of BNT-17BT thick film was successfully improved by the prestress from the different thermal expansion coefficients between BNT-17BT thick film and substrates. The random tetragonal c -direction of BNT-17BT was ordered effectively by the compressive prestress from the different thermal expansion coefficients between the substrates and BNT-17BT during the cooling process.

All BNT-17BT thick films exhibited individual 180° domain areas. The α_c values of BNT-17BT/ Al_2O_3 and BNT-17BT/MgO were 0.36 and 0.80. BNT-17BT/MgO showed a high c -axis preferential tetragonal degree. The temperature dependence of dielectric coefficient, and the temperature dependence of the piezoelectric coefficient d_{33} indicated that T_d 's of BNT-17BT/MgO and BNT-17BT/ Al_2O_3 were 340°C and 310°C . The temperature dependence of the P_r and E_c indicated the high piezoelectric properties of the BNT-17BT thick films. Moreover, for temperatures exceeding 220°C , the piezoelectric properties of the BNT-17BT/MgO thick films were superior to those of PZT system materials.

These results for BNT-17BT thick films demonstrated that the application of the compressive prestress is an effective method to enhance the application temperature of lead-free materials. The detailed studies in this work provided the possibility to exceed the application temperature of lead-containing materials.

References

- 1) F. Gheorghiu, M. Simenas, C.E. Ciomaga, M. Airimioaei, V. Kalendra, J. Banys, M. Dobromir, S. Tascu, and L. Mitoseriu, *Ceram. Int.* **43** [13](2017)9998-10005.
- 2) Y. Sakai and M. Adachi, *J. J. Appl. Phys.* **54** [10S](2015)10NA02.
- 3) W. Wang, L. D. Wang, W. L. Li, D. Xu, Y. F. Hou, W. P. Cao, Y. Feng, and W. D. Fei: *Ceram. Int.* **40** [9](2014)14907-14912.
- 4) J. F. Li, K. Wang, F. Y. Zhu, L. Q. Cheng, and F. Z. Yao: *J. Am. Ceram. Soc.* **96** [12](2013)3677-3696.
- 5) T. Takenaka, K. I. Maruyama, and K. Sakata: *J. J. Appl. Phys.* **30** [Part 1, No. 9B](1991)2236-2239.
- 6) J. B. Lim, D. Suvorov, and J.-H. Jeon, *Ceram. Int.* **38** (2012)S355-S358.
- 7) L. Chen, Q. Lin, J. Hart, S. Li, and D. Wang, *Int. J. Appl. Ceram. Technol.* **13** [5](2016)896-903.
- 8) Y. Sakai, T. Futakuchi, T. Karaki, and M. Adachi, *J. J. Appl. Phys.* **53** [9S](2014)09PB07.
- 9) T. L. Men, H. C. Thong, J. T. Li, M. Li, J. Zhang, V. Zhong, J. Luo, X. Chu, K. Wang, and J.-F. Li, *Ceram. Int.* **43** [12](2017)9538-9542.
- 10) T. Shiraishi, N. Kaneko, M. Kurosawa, H. Uchida, Y. Suzuki, T. Kobayashi, and H. Funakubo, *J. J. Appl. Phys.* **54** [10S](2015)10ND06.
- 11) L. Liu, T. Karaki, T. Fujii, and Y. Sakai, *J. Adv. Dielectr.* **7** [2](2017)1750014.
- 12) Y. Sakai and T. Karaki, *J. J. Appl. Phys.* **56** [10S](2017)10PF01.

- 13) H. Muramatsu, H. Nagata, and T. Takenaka, J. J. Appl. Phys. **55**
[10S](2016)10TB07.

CHAPTER V

CONCLUSION AND PROSPECT

In this chapter, a concise work summary and some prospects will be presented. The aim of this dissertation is to prepare the lead-free piezoelectric KNN-based thin films with MPB compositions and improve the using temperature of BNT-based materials.

To KNN-based thin films, a modified Pechini process for multi-component lead-free $0.055\text{BaZrO}_3-0.935(\text{K}_{0.45}\text{Na}_{0.5}\text{Li}_{0.05})\text{NbO}_3-0.01(\text{Bi}_{0.5}\text{Na}_{0.5})\text{TiO}_3$ (BZ-KNLN-BNT) was developed for the first time. As for the components that were hard to be used in the Pechini process, $\text{Nb}_2\text{O}_5 \cdot n\text{H}_2\text{O}$ was prepared successfully by a simple method and a new preparation method of Ti and Zr sources was found. By the separate preparations of metal sources and the detailed investigating synthesis conditions, the optimal condition for a stable transparent precursor solution was obtained. (100)-oriented BZ-KNLN-BNT thin films were successfully prepared on the (100)-oriented LNO/SiO₂/Si substrates.

Next, $(1-x-y)\text{BaZrO}_3-x(\text{K}_{0.45}\text{Na}_{0.5}\text{Li}_{0.05})\text{NbO}_3-y(\text{La}_{0.5}\text{Na}_{0.5})\text{TiO}_3$ (BZ-KNLN-LNT) ($y = 0.0075$) with the vertical composition at $x = 0.9025$ was studied. The BZ-KNLN-LNT precursor solutions with the compositions around the vertical MPB ($x = 0.9, 0.9025, 0.905$) were successfully synthesized by the similar Pechini process of BZ-KNLN-BNT. By the phase transition analysis based on the high-temperature XRD patterns, it was verified that the prepared precursor solution with $x = 0.9025$ was at the vertical MPB. From the temperature dependence of the dielectric constant and $\tan\delta$

curves, the T_C 's of the bulk ceramics ($x = 0.9025, 0.905$) prepared with the powders from the Pechini process were about 202 and 205 °C, respectively. These results were corroborated with the ceramics prepared with the solid phase reaction method in previous studies. By using the precursor solutions synthesized by the modified Pechini process, the BZ-KNLN-LNT thin films were successfully grown on Nb-doped (100)-oriented SrTiO₃ substrates. Each of the BZ-KNLN-LNT thin films exhibited an excellent (100) orientation along with the substrates and high dielectric properties at a high frequency.

To BNT-based thick films, BNT-17BT thick films were prepared by the screen-printing method and the compressive prestress effects from substrates on the thick film properties were investigated. By using the difference of thermal expansion coefficients between BNT-17BT and substrates, BNT-17BT/Al₂O₃ showed light compressive residual stress with the value of -70 Mpa and BNT-17BT/MgO showed large compressive residual stress with the value of -320 Mpa. The volume fractions of the *c*-domain of BNT-17BT, BNT-17BT/Al₂O₃, and BNT-17BT/MgO were 0.33, 0.36, and 0.80, respectively. From the temperature dependence of the dielectric constant and $\tan\delta$ curves, the T_d 's of BNT-17BT bulk ceramics and BNT-17BT/MgO were about 210 °C and 340 °C. The temperature dependence of d_{33} showed a similar result: $T_{d \text{ BNT-17BT/MgO}} > T_{d \text{ BNT-17BT/Al}_2\text{O}_3} > T_{d \text{ BNT-17BT}}$. These results proved that the application of the compressive prestress from substrate improved the *c*-axis preferential tetragonal phase degree and increased the T_d of BNT-17BT. By comparing the temperature dependence of P_r , when the temperature was above 220 °C, BNT-17BT/MgO still exhibited high piezoelectric properties, but PZT thick films did not.

The KNN-based vertical MPB compositions applied in this work covered most elements in lead-free piezoelectric material studies. The successful preparation of these multi-component thin films provides the possibilities for the practical application of these vertical MPB composition thin films. Moreover, the modified Pechini method is also suitable for other lead-free composition thin films.

The application of prestress in this study was proved to be an effective method to enhance the application temperature of BNT-17BT ceramics. The detailed work in this study indicated that external stress could also order the random tetragonal *c*-direction in other ceramics to improve the piezoelectric properties and the application temperatures.

This work describes the possibility of the preparing multi-component lead-free precursor solutions for piezoelectric thin films and the possibility of the improving the application temperatures of lead-free thick films by the compressive prestress. These detailed studies not only bring the field of lead-free piezoelectric materials a step closer to finding a practical substitute for lead-containing materials, but also provide the possibilities of exceeding lead-containing materials in the future.

LIST OF PUBLICATIONS

1) L. Liu, T. Karaki, T. Fujii, and Y. Sakai

“Preparation of $0.055\text{BaZrO}_3\text{-}0.935(\text{K}_{0.45}\text{Na}_{0.5}\text{Li}_{0.05})\text{NbO}_3\text{-}0.01(\text{Bi}_{0.5}\text{Na}_{0.5})\text{TiO}_3$ piezoelectric thin films from precursor solution by Pechini method”

Journal of Advanced Dielectrics, Vol. 7, 1750014, (2017).

2) Y. Quan, W. Ren, G. Niu, L. Wang, J. Zhao, N. Zhang, M. Lin, Z. Ye, L. Liu, and T. Karaki

“Large Piezoelectric Strain with Superior Thermal Stability and Excellent Fatigue Resistance of Lead-Free Potassium Sodium Niobat-Based Grain Orientation-Controlled Ceramics”

ASC Applied Materials & Interfaces, Vol. 10, pp.10220-10226, (2018).

3) L. Liu, T. Karaki, T. Fujii, and Y. Sakai

“Effect of substrate material to the properties of screen-printed lead free $(\text{Bi}_{0.5}\text{Na}_{0.5})\text{TiO}_3$ -based thick films”

Japanese Journal of Applied Physics, Vol. 59, 025502, (2020).

LIST OF PRESENTATIONS

- 1) L. Liu T. Karaki, T. Fujii and Y. Sakai: “Preparation of conductive paste using base metal”, The 5th Japan-China Symposium on Ferroelectric Materials and Their Applications, Suzhou, China: Sep. 8-12, 2013.
- 2) L. Liu T. Karaki, T. Fujii and Y. Sakai: “Preparation of lead-free piezoelectric thin films from precursor solutions by Pechini method”, The 5th International Symposium on Organic and Inorganic Electronic Materials and Related Nanotechnologies, Fukui, Japan, Jun. 16-19, 2015.
- 3) L. Liu T. Karaki, T. Fujii and Y. Sakai: “Preparation of lead-free piezoelectric thin films from precursor solutions by Pechini method”, The 8th Japan-China Symposium on Ferroelectric Materials and Their Applications, Tsukuba, Japan, Sep. 29-Oct 2, 2016.
- 4) L. Liu T. Karaki, T. Fujii and Y. Sakai: “Preparation of lead-free piezoelectric thin films from precursor solutions by Pechini method”, The 33th Meeting on Ferroelectric Materials and Their Applications, Kyoto, Japan, May, 25-28, 2016.
- 5) L. Liu T. Karaki, T. Fujii and Y. Sakai: “Preparation of $0.09\text{BaZrO}_3\text{-}0.9025(\text{K}_{0.45}\text{Na}_{0.5}\text{Li}_{0.05})\text{NbO}_3\text{-}0.0075(\text{La}_{0.5}\text{Na}_{0.5})\text{TiO}_3$ piezoelectric thin films from precursor solution by Pechini method”, The 6th International Symposium on Organic and Inorganic Electronic Materials and Related Nanotechnologies, Fukui, Japan, Jun. 18-21, 2017.
- 6) L. Liu, T. Karaki, T. Fujii, and Y. Sakai: “Preparation of $\text{BaZrO}_3\text{-}(\text{K}_{0.45}\text{Na}_{0.5}\text{Li}_{0.05})\text{NbO}_3\text{-}(\text{La}_{0.5}\text{Na}_{0.5})\text{TiO}_3$ piezoelectric thin films from precursor solution by Pechini method”, 2018 IFAAP Joint Conference, Hiroshima, Japan, May 27-June 1, 2018.